Global Journal

OF SCIENCE FRONTIER RESEARCH: A

Online ISSN: 2249-4626
Print ISSN: 0975-5896
DOI: 10.17406/SFR

Physics & Space Science

Electron-Photon Momentum Relation in Hydrogen Atom

Mars Settlement: Nearly Impossible

EoS Parameter from Quantum Gravity

Two Waves of Electron in Hydrogen Atom

Discovering Thoughts, Inventing Future

VOLUME 26 / ISSUE 2 / VERSION 1.0

Global Journal of Science Frontier Research

Section A - Physics & Space Science

Volume 26 2026 **Issue A2**

Global Journal of Science Frontier Research

ISSN (Online): 2249-4626 • ISSN (Print): 0975-5896

Open Access Policy

Publisher

Global Journals Incorporated
301 Edgewater Place, Suite 100
Wakefield, MA 01880, United States

Copyright

Disclaimer

Compiled in the United States of America

Preface

The Global Journal of Science Frontier Research (GJSFR) is pleased to present this issue, bringing together a curated collection of high-quality research papers that explore the cutting-edge frontiers of natural and applied sciences.

This issue features research spanning topics including physics & space science, chemistry, biological science, agriculture & veterinary science, marine science, mathematics & decision science, biotechnology & genetics, environment & geology, and interdisciplinary scientific inquiry. Each paper has undergone a rigorous double-blind peer-review process to ensure scientific rigor and originality.

We would like to express our sincere gratitude to the authors for entrusting their research with us, to the reviewers for their thorough and constructive evaluations, and to our readers for their continued engagement with the scientific discourse.

We hope that the research presented herein inspires further discovery and contributes meaningfully to the advancement of scientific knowledge.

The Chief Editor
Global Journal of Science Frontier Research
Global Journals Organization

Table of Contents

GLOBAL JOURNAL
OF SCIENCE FRONTIER RESEARCH - A: PHYSICS & SPACE SCIENCE

Volume 26 | Issue 2 | 2026 · Article ID: GJSFR-258904 · Language: English

The Relationship between the Momentum of an Electron and the Momentum of a Photon Possessed by the Electron, Derived from an Energy-Momentum Relationship Applicable to an Electron inside a Hydrogen Atom

Article Record

K. Suto *

*Corresponding Author

RECEIVED	ACCEPTED	ONLINE PUBLISHED	PUBLISHED	PEER REVIEW
2026-06-26	2026-07-09	2026-07-21	2026-09-23	Double Blind

Abstract

Einstein's energy-momentum relationship, which holds in an isolated system in free space, cannot be applied to an electron in a hydrogen atom, where potential energy exists. Thus, the author has previously derived an energy-momentum relationship applicable to an electron in a hydrogen atom. It is possible, by using this relationship, to derive the relationships between the momentum of an electron, and the momentum of a photon possessed by the electron. There is a close relationship between these two physical quantities and the fine structure constant. Also, if the de Broglie relationship is applied to the energy-momentum relationship derived by the author, it is possible to derive the relationship between the wavelength of a moving electron, the wavelength of a photon possessed by the electron, and the Compton wavelength of the electron.

compton wavelength · einstein's energy-momentum relationship · energy-momentum relationship in a hydrogen atom · fine structure constant · momentum of a electron · momentum of a photon

AI USE STATEMENT
No generative AI was used for analysis or results.

FUNDING
No external funding was declared for this work.

CONFLICT OF INTEREST
The authors declare no conflict of interest.

DATA AVAILABILITY
Not applicable for this article.

ETHICS
No ethics committee approval was required for this article type.

CONSENT
Not applicable for this article.

TRIAL REG.
Not applicable.

Crossref DOI: 10.34257/GJSFRA258904

How to Cite: Suto (2026). The Relationship between the Momentum of an Electron and the Momentum of a Photon Possessed by the Electron, Derived from an Energy-Momentum Relationship Applicable to an Electron inside a Hydrogen Atom. Global Journal of Science Frontier Research, 26(2), 1-5. DOI: 10.34257/GJSFRA258904

AR Experience Web Page DOI

Print ISSN 0975-5896

Online ISSN 2249-4626

Under the strict compliance and defined process of

ARCHIVAL RECORD
GJSFR · Vol 26 · Issue 2 · 2026
Article ID GJSFR-258904 · DOI 10.34257/GJSFRA258904
Print ISSN 0975-5896 · Online ISSN 2249-4626

Global Journal of Science Frontier Research - Section A
GJSFR Volume 26 Issue 2

The Relationship between the Momentum of an Electron and the Momentum of a Photon Possessed by the Electron, Derived from an Energy-Momentum Relationship Applicable to an Electron inside a Hydrogen Atom

K. Suto*

Abstract

Einstein's energy-momentum relationship, which holds in an isolated system in free space, cannot be applied to an electron in a hydrogen atom, where potential energy exists. Thus, the author has previously derived an energy-momentum relationship applicable to an electron in a hydrogen atom. It is possible, by using this relationship, to derive the relationships between the momentum of an electron, and the momentum of a photon possessed by the electron. There is a close relationship between these two physical quantities and the fine structure constant. Also, if the de Broglie relationship is applied to the energy-momentum relationship derived by the author, it is possible to derive the relationship between the wavelength of a moving electron, the wavelength of a photon possessed by the electron, and the Compton wavelength of the electron.

Keywords: *compton wavelength, einstein's energy-momentum relationship, energy-momentum relationship in a hydrogen atom, fine structure constant, momentum of a electron, momentum of a photon*

* **Corresponding Author**
K. Suto

DOI
10.34257/GJSFRA258904

1. Introduction

N.Bohr was the first to derive the energy levels of a hydrogen atom [1]. Bohr considered the case where an electron moves in a circle at constant speed around the atomic nucleus (a proton).The following formula of motion of Newton holds when an electron moves at velocity v on a circular orbit with radius r.

$$\frac{m_e v^2}{r} = \frac{1}{4\pi\varepsilon_0}\frac{e^2}{r^2} \tag{1}$$

This formula indicates that the centrifugal force acting on an electron (left side) is equal to the Coulomb attraction exerted on an electron by the atomic nucleus (right side). Here, m_e is the rest mass of the electron.

Multiplying both sides of Formula (1) by 1/2 yields the following.

$$\frac{1}{2}m_e v^2 = \frac{1}{2}\frac{1}{4\pi\varepsilon_0}\frac{e^2}{r} \tag{2}$$

Incidentally, the potential energy of a hydrogen atom can be expressed with the following formula.

$$V(r) = -\frac{1}{4\pi\varepsilon_0}\frac{e^2}{r} \tag{3}$$

Therefore, Formula (1) can be written as follows.

$$\frac{1}{2}m_e v^2 = -\frac{1}{2}V(r) \tag{4}$$

Also, in classical quantum theory, the total mechanical energy of a hydrogen atom is defined as the sum of the kinetic energy K and potential energy $V(r)$ of the electron, and thus the energy can be described with the following formula.

$$E = \frac{m_e v^2}{2} - \frac{1}{4\pi\varepsilon_0}\frac{e^2}{r} \tag{5}$$

Hence, the energy of a hydrogen atom is given by the following formula.

$$E = -\frac{1}{2}V(r) + V(r) = \frac{1}{2}V(r) = -\frac{1}{2}m_e v^2 = -\frac{1}{2}\frac{1}{4\pi\varepsilon_0}\frac{e^2}{r} \tag{6}$$

When an electron with energy $m_e c^2$ is taken into an energy level of a hydrogen atom, the electron emits a photon of energy $h\nu$, but the electron simultaneously acquires the same amount of kinetic energy as $h\nu$. The source which supplies these energies can only be the rest mass energy of the electron.

The author has previously pointed out that the reduction in rest mass energy of the electron corresponds to the potential energy of the hydrogen atom [2, 3, 4].

Here, if the reduction in rest mass energy of the electron is represented as $-\Delta m_e c^2$, the potential energy can be defined as follows.

$$V(r) = -\Delta m_e c^2 \tag{7}$$

Next, the relativistic energy of an electron in a hydrogen atom is defined as follows.

$$m_n c^2 = m_e c^2 - \Delta m_e c^2 + K_{re,n} = m_e c^2 + \frac{1}{2}V(r_n) = m_e c^2 - K_{re,n} \tag{8}$$

Here, $m_n c^2$ is the relativistic energy of the electron, described with an absolute scale.

$m_n c^2$ is the sum of the residual part of the rest mass energy of the electron ($m_e c^2 + V(r_n)$) and the kinetic energy $K_{re,n}$.

Also, $E_{re,n}$ are the relativistic energy levels of a hydrogen atom. The "re" subscript of $E_{re,n}$ stands for "relativistic."

These energies can be illustrated as follows (see *Fig. 1*).

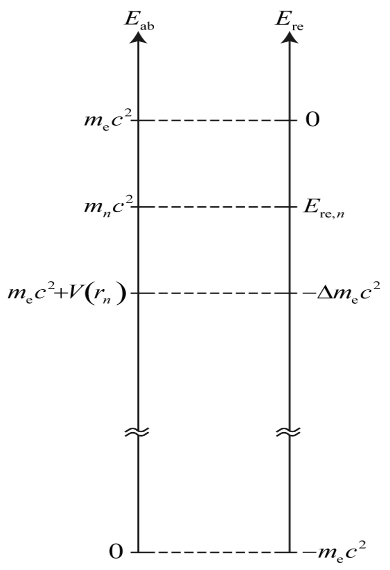

Figure 1. For $E_{re,n}$, the potential energy when the electron is at a position infinitely distant from the atomic nucleus (proton) is set to zero, just as for the energy levels $E_{BO,n}$ of a hydrogen atom derived nonrelativistically by Bohr. The relationship between $E_{BO,n}$ and $E_{re,n}$ is elucidated in Section 2, but $E_{BO,n}$ is an approximation for $E_{re,n}$. The "ab" subscript of E_{ab} stands for "absolute."

However, the energy of an electron placed at an infinitely distant position is not originally zero, it is $m_e c^2$ (however, the potential energy is zero in this case too). Energy in its original sense should be described with an absolute scale. In classical quantum theory, the potential energy of an electron at an infinite distance and the energy of the hydrogen atom are both regarded as zero. However, that idea is mistaken. There is a problem with classical quantum theory which describes the energy levels of a hydrogen atom in relative terms, ignoring the special theory of relativity (STR).

Also, $E_{re,n}$ has the following relationship with the energy $h\nu$ of the photon emitted to the outside from the electron.

$$E_{re,n} + h\nu = 0 \tag{9}$$

This completes preparations for deriving an energy-momentum relationship applicable to an electron in a hydrogen atom.

The author has already derived an energy-momentum relationship applicable to the electron in a hydrogen atom using five types of methods [5, 6, 7, 8, 9, 10]. One of those is reviewed in Section 2.

2. Energy-Momentum Relationship Applicable to an Electron in a Hydrogen Atom

According to the STR, the following relation holds between the energy and momentum of a body moving in free space [11].

$$(mc^2)^2 = (m_0 c^2)^2 + c^2 p^2 \tag{10}$$

Here, $m_0 c^2$ is the rest mass energy of the body. And mc^2 is the relativistic energy.

Incidentally, Einstein and Sommerfeld defined the relativistic kinetic energy as follows [12].

$$K_{re} = mc^2 - m_0 c^2 \tag{11}$$

The "re" subscript of K_{re} stands for "relativistic."

Taking Formula (11) into account, Formula (10) can be rewritten as follows.

$$\begin{aligned} c^2 p^2 &= (mc^2 - m_0 c^2)(mc^2 + m_0 c^2) \\ &= K_{re}(mc^2 + m_0 c^2) \end{aligned} \tag{12}$$

From this, the following formula for relativistic kinetic energy can be derived.

$$K_{re} = \frac{p_{re}^2}{m + m_0} \tag{13}$$

Here, the subscript "re" is attached to p, just as in K_{re}.

Incidentally, Einstein's energy-momentum relationship (10) holds when the energy absorbed by a body is all converted to kinetic energy of that body. However, an electron in an atom acquires kinetic energy through emission of energy. Therefore, Einstein's relationship (10) cannot be applied to an electron in an atom.

Here, the relativistic kinetic energy of an electron inside a hydrogen atom is defined as follows by referring to Formulas (11) and (13).

$$K_{re,n} = m_e c^2 - m_n c^2 \tag{14}$$

$$K_{re,n} = \frac{p_{e,n}^2}{m_e + m_n} \tag{15}$$

Here, $p_{e,n}$ is the relativistic momentum of the electron. (Due to the situation in this paper, $p_{re,n}$ is rewritten here as $p_{e,n}$.)

The term "relativistic" as used in this paper is not based on the STR. It means that the fact that the mass of the electron changes due to the electron's motion is taken into account. It must be noted that the mass of the electron decreases when the velocity of the electron inside the atom increases [13].

Linking the right sides of Formulas (14) and (15) with an equals sign and rearranging, the following relationship can be derived.

$$(m_n c^2)^2 + c^2 p_{e,n}^2 = (m_e c^2)^2 \tag{16}$$

where,

$$m_n c^2 = m_e c^2 + E_{re,n} = m_e c^2 - K_{re,n} = m_e c^2 + \frac{1}{2} V(r_n) \tag{17}$$

The following formula can be derived from Formula (16).

$$m_n c^2 = m_e c^2 \left(1 + \frac{v_n^2}{c^2}\right)^{-1/2} \tag{18}$$

To change Formula (18) into a formula of quantum theory, the discreteness of energy must be incorporated into Formula (18).

Previously, the author has shown that the following relationship holds for an electron in a hydrogen atom [14, 15].

$$\frac{v_n}{c} = \frac{\alpha}{n} \tag{19}$$

Here, α is the following fine-structure constant.

$$\alpha = \frac{e^2}{4\pi\varepsilon_0 \hbar c} = 7.2973525693 \times 10^{-3} \tag{20}$$

where α is a dimensionless constant introduced by A. Sommerfeld in 1916.

Using the relationship in Formula (19), Formula (18) can be written as follows.

$$m_n c^2 = m_e c^2 \left(\frac{n^2}{n^2 + \alpha^2} \right)^{1/2} \tag{21}$$

Taking Formula (21) into account, $E_{re,n}$ in Formula (17) can be written as follows.

$$E_{re,n} = m_n c^2 - m_e c^2 = m_e c^2 \left[\left(\frac{n^2}{n^2 + \alpha^2} \right)^{1/2} - 1 \right], \quad n = 0, 1, 2, \ldots \tag{22}$$

Formula (22) gives the energy levels of a hydrogen atom, taking relativity into account (see *Fig. 2*).

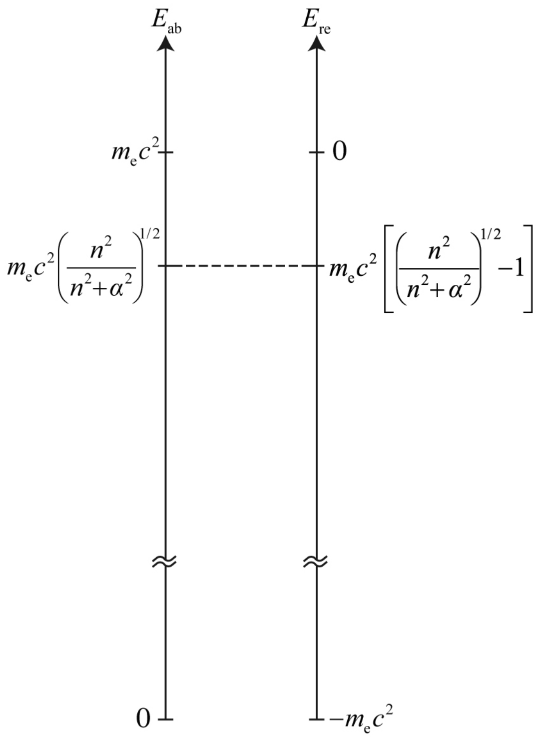

Figure 2. In this figure, the energies in Figure 1, $m_n c^2$ and $E_{re,n}$, have been rewritten using Formulas (21) and (22).

Formula (22) predicts the existence of a state with n=0 [16].

Next, when the part of Formula (22) in parentheses is expressed as a Taylor expansion,

$$\begin{aligned} E_{re,n} &\approx m_e c^2 \left[\left(1 - \frac{\alpha^2}{2n^2} + \frac{3\alpha^4}{8n^4} - \frac{5\alpha^6}{16n^6} \right) - 1 \right] \\ &\approx -\frac{\alpha^2 m_e c^2}{2n^2}. \end{aligned} \tag{23}$$

Incidentally, the nonrelativistic energy levels of a hydrogen atom, derived by Bohr, are given by the following formula.

$$E_{BO,n} = -\left(\frac{1}{4\pi\varepsilon_0} \right)^2 \frac{m_e e^4}{2\hbar^2} \cdot \frac{1}{n^2}, \quad n = 1, 2, \ldots \tag{24}$$

The "BO" subscript of $E_{BO,n}$ stands for "Bohr."

However, when discussing the energy levels of a hydrogen atom, it is best if the rest mass energy of the electron is included in the formula. Thus Formula (24) is rewritten as follows.

$$E_{BO,n} = -\frac{m_e c^2}{2} \left(\frac{e^2}{4\pi\varepsilon_0 \hbar c} \right)^2 \frac{1}{n^2} = -\frac{\alpha^2 m_e c^2}{2n^2}, \quad n = 1, 2, \ldots \tag{25}$$

From this, it is evident that Formula (24) is an approximation of Formula (22).

The energies of the hydrogen atom and electron treated thus far are summarized in the following table (see *Table 1*) [17].

Table 1. Comparison of the energies of a hydrogen atom predicted by Bohr's classical quantum theory and this paper. The difference between the two is whether or not the STR is taken into consideration.

	Classical Quantum Theory	This Paper
Potential Energy $V(r_\infty)$ when $r = \infty$	$V(r_\infty) = 0$	$V(r_\infty) = 0$
Energy of Hydrogen Atom when $r = \infty (n = \infty)$	$E_{BO,\infty} = 0$	$E_{re,\infty} = 0$
Energy of Electron when $r = \infty$	0 ?	$m_e c^2$
Energy of Hydrogen Atom when $r = r_n$	$E_{BO,n} = \frac{1}{2} V(r_n)$	$E_{re,n} = \frac{1}{2} V(r_n)$
Energy of Electron Described with an Absolute Scale $m_n c^2$	Not Discussed	$m_e c^2 + \frac{1}{2} V(r_n)$
STR	Not Considered	Considered
Electron Mass	m_e (Constant)	m_n (Varies)
Principal Quantum Number	$n = 1, 2, \ldots$	$n = 0, 1, 2, \ldots$

Now, in preparation for the discussion in Section 3, let us rewrite Formula (16) as a relationship for momentum. To do that, it is enough to divide both sides of Formula (16) by c^2. That is,

$$(m_n c)^2 + p_{e,n}^2 = (m_e c)^2 \tag{26}$$

3. Discussion

It is known that the momentum and wavelength of an electron have the following relation.

$$p = \frac{h}{\lambda} \tag{27}$$

Here, if the momentum of the photon possessed by an electron in a state with principal quantum number n is $p_{p,n}$, and the momentum of a moving electron is $p_{e,n}$, then these two types of momentum can be expressed as follows.

$$p_{p,n} = m_n c = m_e c \left(\frac{n^2}{n^2 + \alpha^2} \right)^{1/2} = \frac{h}{\lambda_{p,n}} \tag{28}$$

$$p_{e,n} = m_n v_n = m_e c \left(\frac{\alpha^2}{n^2 + \alpha^2} \right)^{1/2} = \frac{h}{\lambda_{e,n}} \tag{29}$$

Here, $\lambda_{p,n}$ is the wavelength of a photon whose momentum is $p_{p,n}$, and $\lambda_{e,n}$ is the wavelength of an electron whose momentum is $p_{e,n}$.

The following formula can be obtained from the definition of the Planck constant [18].

$$m_e c = \frac{h}{\lambda_C}. \tag{30}$$

Here, λ_C is the Compton wavelength of the electron.

Incidentally, Formula (26) can also be written as follows.

$$p_{\mathrm{p},n}^2 + p_{\mathrm{e},n}^2 = (m_\mathrm{e}c)^2 \tag{31}$$

The following relationship can be derived by substituting the three types of momentum in Formulas (28) to (30) into Formula (31) and rearranging.

$$\frac{1}{\lambda_{\mathrm{p},n}^2} + \frac{1}{\lambda_{\mathrm{e},n}^2} = \frac{1}{\lambda_\mathrm{C}^2} \tag{32}$$

Formula (16) has already been derived in another paper, but Formula (32) has been derived for the first time in this paper.

4. Conclusions

Due to Formulas (28) and (29), the following relationship holds between the two types of wavelengths corresponding to the momentum of an electron in a hydrogen atom and the momentum of a photon possessed by the electron.

$$\frac{\lambda_{\mathrm{p},n}}{\lambda_{\mathrm{e},n}} = \frac{p_{\mathrm{e},n}}{p_{\mathrm{p},n}} = \frac{\alpha}{n}. \tag{33}$$

In the case where $n = 1$,

$$\frac{\lambda_{\mathrm{p},1}}{\lambda_{\mathrm{e},1}} = \frac{p_{\mathrm{e},1}}{p_{\mathrm{p},1}} = \alpha. \tag{34}$$

The fine structure constant α has previously been understood as the ratio of the velocity of an electron, as the particle in the ground state of a hydrogen atom, and the speed of light. However, it was not understood why the ratio of the two is so important for physics.

However, if the electron is considered as a wave, the fine structure constant can be understood as the ratio of the wavelength $\lambda_{\mathrm{p},1}$ of light possessed by an electron in the ground state and the wavelength $\lambda_{\mathrm{e},1}$ of a moving electron [19].

Also, this paper has derived the fact that the following relationship holds between the wavelength of an electron moving inside a hydrogen atom, the wavelength of a photon possessed by the electron, and the Compton wavelength of the electron.

$$\frac{1}{\lambda_{\mathrm{p},n}^2} + \frac{1}{\lambda_{\mathrm{e},n}^2} = \frac{1}{\lambda_\mathrm{C}^2}. \tag{35}$$

However, the only quantum number addressed in this paper is the principal quantum number n. This does not mean that all energy levels can be explained with this quantum condition (33) alone. However, Formula (35) is believed to be a new discovery.

In this paper, I was unable to derive a relationship incorporating the spin wave of the electron. It is hoped that, in the future, a relationship will be derived incorporating the electron spin.

For this purpose, I believe it will be necessary to solve the relativistic wave equation previously derived by the author [6, 20].

ACKNOWLEDGEMENTS

I would like to express my thanks to the staff at ACN Translation Services for their translation assistance. Also, I wish to express my gratitude to Mr. H. Shimada for drawing figures.

REFERENCES

[1] N. Bohr, "On the Constitution of Atoms and Molecules". Philosophical Magazine, 26, 1, (1913). https://doi.org/10.1080/14786441308634955

[2] K. Suto, "True nature of potential energy of a hydrogen atom". Physics Essays, 22, 135-139, (2009). https://koshun129.sakura.ne.jp/physics/4spw_index.html

[3] K. Suto, "Potential Energy of the Electron in a Hydrogen Atom and a Model of a Virtual Particle Pair Constituting the Vacuum". Applied Physics Research, 10, 4, 93-101, (2018). https://doi.org/10.5539/apr.v10n4p93

[4] K. Suto, "Limits on Application of the Formula for Potential Energy of a Hydrogen Atom and a Previously Unknown Formula". Journal of High Energy Physics, Gravitation and Cosmology, 11, 3, 1039-1051, (2025). https://doi.org/10.4236/jhepgc.2025.113067

[5] K. Suto, "An Energy-Momentum Relationship for a Bound Electron Inside a Hydrogen Atom". Physics Essays, 24, 301-307, (2011). https://koshun129.sakura.ne.jp/physics/4spw_index.html

[6] K. Suto, "Derivation of a Relativistic Wave Equation More Profound than Dirac's Relativistic Wave Equation". Applied Physics Research, 10, 102-108, (2018). https://doi.org/10.5539/apr.v10n6p102

[7] K. Suto, "Theoretical Prediction of Negative Energy Specific to the Electron". Journal of Modern Physics, 11, 712-724, (2020). https://doi.org/10.4236/jmp.2020.115046

[8] K. Suto, "Previously Unknown Formulas for the Relativistic Kinetic Energy of an Electron in a Hydrogen Atom". Journal of Applied Mathematics and Physics, 11, 972-987, (2023). https://doi.org/10.4236/jamp.2023.114065

[9] K. Suto, "The Strange Relationship Between the Momentum of a Photon Emitted from an Electron and the Momentum Acquired by the Electron". Journal of Applied Mathematics and Physics, 12, 2652-2664, (2024). https://doi.org/10.4236/jamp.2024.127157

[10] K. Suto, " The Photon Energy of an Electron with Rest Mass Energy of m_0c^2 is m_0c^2". Applied Physics Research, 17, 44-56, (2025). https://doi.org//10.5539/apr.v17n1p44

[11] A. Einstein, Relativity. Crown, New York, 43, (1961).

[12] A. Sommerfeld, "Atomic Structure and Spectral Lines". Methuen & Co. Ltd., London, 528, (1923).

[13] K. Suto, "Electron Mass in an Atom Is Less than Rest Mass. Journal of Applied Mathematics and Physics". 11, 3953-3961, (2023). https://doi.org/10.4236/jamp.2023.1112252

[14] K. Suto, "The Relationship Enfolded in Bohr's Quantum Condition and a Previously Unknown Formula for Kinetic Energy". Applied Physics Research, 11, 19-34, (2019). https://doi.org/10.5539/apr.v11n1p19

[15] K. Suto, "The Quantum Condition That Should Have Been Assumed by Bohr When Deriving the Energy Levels of a Hydrogen Atom". Journal of Applied Mathematics and Physics, 9, 1230-1244, (2021). https://doi.org/10.4236/jamp.2021.96084

[16] K. Suto, " An Energy Level with Principal Quantum Number $n = 0$ Exists in a Hydrogen Atom". London Journal of Research in Science, Natural and Formal, 23, 2, 1.0, 65-79, (2023). https://journalspress.com/LJRS_Volume23/An-Energy-Level-with-Principal-Quantum-Number-n-0-Exists-in-a-Hydrogen-Atom.pdf

[17] K. Suto, "Bohr's Quantum Condition Derived From Classical Mechanics and Its Limits of Application". Applied Physics Research, 18, 1, 294-304, (2026). https://doi.org/10.5539/apr.v18n1p294

[18] K. Suto, “The Planck Constant Was Not a Universal Constant”. Journal of Applied Mathematics and Physics, 8, 456-463, (2020). https://doi.org/10.4236/jamp.2020.83035

[19] K. Suto, “ A Surprising Physical Quantity Involved in the Phase Velocity and Energy Levels of the Electron in a Hydrogen Atom”. Applied Physics Research, 14, 2, 1-17, (2022). https://doi.org/10.5539/apr.v14n2p1

[20] K. Suto, “Previously Unknown Ultra-low Energy Level of the Hydrogen Atom Whose Existence can be Predicted”. Applied Physics Research, 6, 6, 64-73, (2014). http://dx.doi.org/10.5539/apr.v6n6p64

GLOBAL JOURNAL
OF SCIENCE FRONTIER RESEARCH - A: PHYSICS & SPACE SCIENCE
Volume 26 | Issue 2 | 2026
Article ID: GJSFR-259200
Language: English
CATALOGING
MSC • 85-03
ARXIV • physics.pop-ph

Mars will Not be Settled

Article Record

Volker W. Thürey*

*Corresponding Author

RECEIVED	ACCEPTED	ONLINE PUBLISHED	PUBLISHED	PEER REVIEW
2026-07-13	2026-07-25	2026-08-18	2026-09-23	Double Blind

Abstract

Many people dream of establishing a settlement on the planet Mars, especially the American entrepreneur Elon Musk. However, I believe this is nearly impossible because of the planet's extremely harsh environmental conditions. Compared to Mars, Earth is truly a paradise.

Elon Musk | geoengineering | Mars | terraforming

AI USE STATEMENT
No generative AI was used for analysis or results.

FUNDING
No external funding was declared for this work.

CONFLICT OF INTEREST
The authors declare no conflict of interest.

DATA AVAILABILITY
Not applicable for this article.

ETHICS
No ethics committee approval was required for this article type.

CONSENT
Not applicable for this article.

TRIAL REG.
Not applicable.

Crossref DOI: 10.34257/GJSFRA259200

How to Cite: Thürey (2026). Mars will Not be Settled. Global Journal of Science Frontier Research, 26(2), 7-9. DOI: 10.34257/GJSFRA259200

AR Experience Web Page DOI

Print ISSN 0975-5896

Online ISSN 2249-4626

Under the strict compliance and defined process of

ARCHIVAL RECORD

GJSFR · Vol 26 · Issue 2 · 2026

Article ID GJSFR-259200 · DOI 10.34257/GJSFRA259200

Print ISSN 0975-5896 · Online ISSN 2249-4626

Global Journal of Science Frontier Research - Section A
GJSFR Volume 26 Issue 2

Mars will Not be Settled

Volker W. Thürey*

Abstract

Many people dream of establishing a settlement on the planet Mars, especially the American entrepreneur Elon Musk. However, I believe this is nearly impossible because of the planet's extremely harsh environmental conditions. Compared to Mars, Earth is truly a paradise.

Keywords: *Elon Musk, geoengineering, Mars, terraforming*

*** Corresponding Author**
Volker W. Thürey, Bremen, Germany

DOI
10.34257/GJSFRA259200

1. Introduction

During the Klondike Gold Rush in Alaska in 1897, many people lost their lives while searching for gold. No one went there expecting to die; instead, they were driven by dreams of wealth and a better future. Although some miners became rich and fulfilled their dreams, many others faced extreme hardship, hunger, disease, and death.

Today, many people dream of establishing a human settlement on Mars. This topic is widely discussed in public media, especially by visionaries such as Elon Musk. See, for instance, [1]. However, I believe that creating a permanent settlement on Mars would be nearly impossible with current technology. Compared to the harsh environment of Mars, even the difficult conditions of Alaska seem pleasant.

Mars has no breathable air, extremely cold temperatures, dangerous radiation, and very limited natural resources for human survival. In addition, transporting people and supplies to Mars would require enormous costs and advanced technology. For these reasons, Earth remains the only planet naturally suited for human life and should be valued and protected.

2. Oxygen

One of the greatest challenges in the colonization of Mars would be finding enough people willing to live there permanently. Although many people claim today that they would gladly move to Mars if given the opportunity, I believe that most would change their minds when faced with the reality of living on the planet. Human beings usually make major decisions only when they believe their quality of life will improve. On Mars, however, living conditions would be far worse than on Earth.

The environment on Mars is extremely hostile to human life. The atmosphere is not breathable because it contains no oxygen. Without a spacesuit as a life support system, a person would lose consciousness within seconds and die within minutes. In addition, Mars has freezing temperatures, powerful dust storms, and high levels of harmful radiation because it lacks a strong magnetic field and protective atmosphere.

Even Elon Musk, one of the strongest supporters of Mars colonization, is unlikely to live there permanently himself. His vision mainly focuses on sending other people to establish settlements on the Mars.

The lack of oxygen is another major obstacle to settling other celestial bodies such as Venus or Titan. Furthermore, these worlds present additional environmental challenges .Venus is extremely hot due to its thick carbon dioxide atmosphere, while Titan is far too cold to support human life. These harsh conditions highlight how rare and valuable Earth is as the only known planet capable of naturally sustaining life.

3. Terraforming

The idea of "terraforming" other planets is often discussed in science fiction and public debates about space exploration. Terraforming means transforming another planet so that it becomes similar to Earth and suitable for human life. However, I do not see how this could realistically be achieved, especially when it comes to creating a breathable atmosphere.

On earth: oxygen was produced over million of years by plants, algae, and bacteria through natural biological processes. Without oxygen, the atmosphere is not breathable and therefore useless for human survival. Reproducing such a complex process on another planet would require enormous amounts of time, technology, and resources. In addition, planets such as Mars lack many of the natural conditions that make life possible on Earth.

The concept of 'terraforming' reminds me of the film The Great Dictator. In one famous scene, Charlie Chaplin, in his role as dictator Hynkel, plays with the balloon - shaped like the Earth. The scene symbolically shows human arrogance and the desire to control the world.

For me, the idea of terraforming a planet represents a form of human megalomania. Humans, like all living beings, are products of evolution. Our bodies and way of life developed under the unique environmental conditions of Earth. Attempting to drastically alter another planet to meet human needs involves interfering with natural processes that we do not fully understand. The consequences of such actions could be unpredictable and impossible to control.

Instead of trying to transform other planets, humanity should focus more on protecting and preserving Earth, the only planet naturally capable of supporting human life.

4. Asteroids

Another topic often discussed in connection with space exploration is asteroid mining. Many asteroids travel through space at extremely high speeds, often exceeding 10 kilometers per second. Even the Moon moves around Earth at a speed of about one kilometer per second. Reaching, landing on, and mining such fast-moving objects would therefore be extremely difficult and dangerous.

Some people argue enthusiastically in favour of asteroid mining because astroids may contain minerals worth billions of dollars. This would indeed be valuable if such an asteroid were easily accessible on Earth. However, in reality, these objects are located far away in space and move at very high speeds. Extracting resources from them would require highly advanced technology, enormous amounts of energy, and extremely advanced transportation systems.

For these reasons, I believe that asteroid mining would be far too expensive to become economically practical in the near future. It would only be worthwhile if the costs of mining and transporting materials from space become as low as mining resources on Earth. At present, I do not believe technological progress will reach such a level in the foreseeable future.

Furthermore, there are many additional risks involved, including equipment failure, radiation exposure, communication delays, and the challenge of operating machinery in a zero-gravity environment. These difficulties show that space mining is much more complicated than it is often presented in popular media.

Rather than investing in uncertain and expensive space projects, humanity should prioritize the responsible use of Earth's natural resources and the development of sustainable technologies on Earth.

5. Space Travel

Another major topic in modern science and science fiction is interstellar space travel. However, I believe that travelling to other star systems will remain impossible with our current level of technology. The distance between stars are unimaginably large. Even the nearest star system, Alpha Centauri, is more than four light-years away from Earth. With today's spacecraft technology, such a journey would take thousands of years.

Of course, future scientific discoveries may lead to new technologies that we cannot yet imagine. In the television series Star Trek, spaceships use a 'warp drive' that allows them to travel faster than light. Although this idea is fascinating, it remains purely theoretical and far from practical realization.

Even if humanity were able to build spacecraft capable of travelling at speeds close to the speed of light, serious dangers would still exist. One major hazard would be collisions with microscopic particles or space debris. Although the probability of such a collision is very small, the kinetic energy of even a microscopic particle becomes enormous at extremely high speeds.

This means that an impact with a very small particle could cause catastrophic damage or even destroy a spacecraft completely. No crew would willingly risk such dangers during a long interstellar journey.

In addition, long-distance space travel would create many other challenges, such as radiation exposure, psychological stress, lack of resources, and the difficulty of maintaining life support systems for many years. These problems demonstrate that interstellar travel is not only a technological challenge but also a biological and human one.

For these reasons, I believe that journeys to distant stars will remain largely within the realm of science fiction for the foreseeable future.

6. Habitable Zone

Another major topic in astronomy is the search for life elsewhere in the universe. One of the best-known organizations involved in this research is the SETI Institute, which searches for signs of intelligent extraterrestrial life.

In my opinion, the search conducted by SETI is unlikely to succeed because I believe that intelligent civilisations may eventually destroy their own environments after developing advanced technology. There are probably countless exoplanets in the universe, and some scientists argue that this increases the likelihood of intelligent life. However, even if such civilisations exist and continue to develop technologically, I believe that they may ultimately damage their natural environments, just as humans are currently doing on earth.

As technology advances, populations may also increase because of improvements in medicine and living conditions. This growth can contribute to environmental destruction, pollution, and climate change. Human activity on Earth already demonstrates that uncontrolled technological progress can have harmful effects on the natural environment.

Astronomers have discovered more than 5,000 exoplanets by the year 2026, yet no confirmed signs of extraterrestrial life has been detected so far. Scientists have also defined the so-called "Goldilocks Zone," or "Habitable Zone," which describes the region around a star where temperatures may allow liquid water to exist.

However, some moons located far outside these habitable zones may also contain conditions suitable for life. For example, Europa and Enceladus are believed to contain liquid water beneath their icy surfaces. These discoveries broaden the range of environments in which life could potentially exist and increase the probability of finding microbial organisms somewhere in the universe.

Even in the Habitable Zone, conditions may still be unsuitable for human life. We can survive only a few hours at a temperature of 50 degrees Celsius.

Nevertheless, despite decades of research and observation, no evidence of life beyond earth has yet been confirmed. Perhaps life elsewhere is extremely rare or perhaps humanity is alone in the universe.

7. The Fermi Paradox

Scientists estimate that there may be around 10^{20} planets in the universe. Even if the probability of life developing on a planet is extremely small, life could still theoretically exist elsewhere. However, the probability of intelligent life evolving may be far smaller. Therefore it is possible that humanity is the only intelligent civilisation in the universe.

This simple estimation illustrates that, despite the enormous number of planets, the probability of intelligent civilisations existing elsewhere may still be extremely low.

The famous Italian physicist Enrico Fermi also questioned why no evidence of extra-terrestrial civilisations has ever been observed. If intelligent life is common in the universe, than humanity should perhaps already have detected signals, spacecraft, or other signs of alien civilisations. This contradiction is known as the "Fermi Paradox".

One possible explanation for the paradox is that intelligent civilisations are extremely rare or may not survive for very long.

Advanced societies could destroy themselves through war, environmental collapse, or uncontrolled technological development before achieving interstellar travel. Another possibility is that humanity is simply alone in the observable universe.

So far, despite decades of scientific research and the discovery of thousands of exoplanets, no confirmed evidence of extra-terrestrial intelligence has been found. For this reason, the question raised by the Fermi Paradox remains one of the greatest mysteries in modern science.

ACKNOWLEDGEMENT

I thank Lydia Ramachandran for a careful reading and for some improvements of the language.

REFERENCES

[1] Mikko M. Puumala, Oskari Sivula, and Kirsi Lehto: *Moving to Mars: The Feasibility and Desirability of Mars Settlements.* Space Policy, November 2023, Volume 66, (2023).

GLOBAL JOURNAL
OF SCIENCE FRONTIER RESEARCH - A: PHYSICS & SPACE SCIENCE
Volume 26 | Issue 2 | 2026
Article ID: GJSFR-276526
Language: English

Rigorously Derive Theoretical Value of EoS Parameter from First Principles

Article Record

Gang Lee *

*Corresponding Author

RECEIVED	ACCEPTED	ONLINE PUBLISHED	PUBLISHED	PEER REVIEW
2026-08-18	2026-08-31	2026-09-14	2026-09-23	Double Blind

Abstract

This paper calculates and obtains the theoretical value of EoS parameter as $w = -1$ via the Feynman path integral formalism for the evolution of the quantum gravitational field without any a posteriori assumptions, and provides a plausible explanation for the potential deviations of dark energy density and EoS parameter.

accelerated expansion | Dark energy | dark energy density | equation of state parameter | Feynman path integral | graviton | Noncommutative quantum gravity

AI USE STATEMENT
No generative AI was used for analysis or results.

FUNDING
No external funding was declared for this work.

CONFLICT OF INTEREST
The authors declare no conflict of interest.

DATA AVAILABILITY
Not applicable for this article.

ETHICS
No ethics committee approval was required for this article type.

CONSENT
Not applicable for this article.

TRIAL REG.
Not applicable.

Crossref DOI: 10.34257/GJSFRA276526

How to Cite: Lee (2026). Rigorously Derive Theoretical Value of EoS Parameter from First Principles. Global Journal of Science Frontier Research, 26(2), 11-14. DOI: 10.34257/GJSFRA276526

AR Experience Web Page DOI

Print ISSN 0975-5896

Online ISSN 2249-4626

Under the strict compliance and defined process of

ARCHIVAL RECORD

GJSFR · Vol 26 · Issue 2 · 2026

Article ID GJSFR-276526 · DOI 10.34257/GJSFRA276526

Print ISSN 0975-5896 · Online ISSN 2249-4626

Global Journal of Science Frontier Research - Section A
GJSFR Volume 26 Issue 2

Rigorously Derive Theoretical Value of EoS Parameter from First Principles

Gang Lee*

Abstract

This paper calculates and obtains the theoretical value of EoS parameter as w = — 1 via the Feynman path integral formalism for the evolution of the quantum gravitational field without any a posteriori assumptions, and provides a plausible explanation for the potential deviations of dark energy density and EoS parameter.

Keywords: *accelerated expansion, Dark energy, dark energy density, equation of state parameter, Feynman path integral, graviton, Noncommutative quantum gravity, quantum gravity*

* **Corresponding Author**
Gang Lee

DOI
10.34257/GJSFRA276526

1. Introduction

In the paper [1], [2], [3], [4], [5], [6], [7] and [8], we introduce the noncommutative quantum gravity and the Feynman path integral of the quantum gravitational field. In this paper, we will calculate the propagator of the gravitational field in the quantum superposition state of a two-source system via the Feynman path integral. Let the initial state gravitational field of the two-source system be prepared in a quantum superposition configuration. In the evolution of the gravitational field of the two-source system, we will obtain a virtual gravitational field. If the two gravitational sources in the final state are separated by a sufficiently large distance such that the quantum superposition effect vanishes, an auxiliary field needs to be introduced to decohere the final state from the quantum superposition state.

2. Quantum Superposition and Energy

In the paper [1] and [2] we introduce a wave packet approximate to the Dirac δ-function which can be explained as a semiclassical graviton. It can be written as follows:

$$\xi^i(x,r) = \begin{cases} \xi^r = r + C^r(x)\exp\left(-\frac{r}{l_P}\right) \\ \xi^\theta = \theta(x) \\ \xi^\phi = \phi(x) \\ \xi^t = t + C^t(x)\exp\left(-\frac{|t|}{t_P}\right) \end{cases} \tag{2.1}$$

The dynamic variables of ξ^i are $C^i(x) = \left(C^r(x), \theta(x), \phi(x), C^t(x)\right)$. Quantization only quantizes the dynamic variable $C^i(x)$. Therefore, for the sake of conciseness, in this paper, we directly identify $C^i(x)$ as the fundamental state function characterizing the gravitational field.

From the paper [1] we have the Lagrangian density of graviton is:

$$\mathcal{L} = -\frac{\eta^{\mu\nu}}{2}\frac{\partial\xi^i(x,r)}{\partial x^\mu}\frac{\partial\xi^j(x,r)}{\partial x^\nu}\eta_{ij} \tag{2.2}$$

For simplicity, assume that the initial state has two gravitational fields $C^i_{(1)}$ and $C^i_{(2)}$ and $C^i_{(2)} = k^i \cdot C^i_{(1)}$. Provided that the two gravitational sources are separated by a sufficiently large spatial interval, no quantum superposition effect can arise between $C^i_{(1)}$ and $C^i_{(2)}$, the initial state can be written as $C^i_{(1+2)} = C^i_{(1)} + C^i_{(2)}$, and the action can be written as $S_{(1+2)} = S[C^i_{(1)}] + S[C^i_{(2)}]$. Denote the final state as $\tilde{C}^i_{(1+2)}$. For the Lagrangian density [2.2], the propagator $K_{(1+2)}$ of $C^i_{(1+2)}$ can be written as follows:

$$
\begin{aligned}
K_{(1+2)} &= \int \mathcal{D}\left[C^i_{(1)} + C^i_{(2)}\right]\left(e^{iS_{(1+2)}/\hbar}\right) \\
&= \int \mathcal{D}\left[C^i_{(1)} + C^i_{(2)}\right]\left(e^{i\left[S[C^i_{(1)}]+S[C^i_{(2)}]\right]/\hbar}\right) \\
&= \int \mathcal{D}\left[C^i_{(1)} + C^i_{(2)}\right]\left(e^{iS[C^i_{(1)}]/\hbar} \cdot e^{iS[C^i_{(2)}]/\hbar}\right)
\end{aligned} \tag{2.3}
$$

If two gravitational sources are sufficiently close to each other or merge into one, quantum superposition effects will arise between $C^i_{(1)}$ and $C^i_{(2)}$. Denote the initial state of the two-source system with quantum superposition as $C^i_{(1\oplus 2)}$, where $\oplus$ denotes the quantum superposition of states, the action can be written as $S_{(1\oplus 2)} = S[C^i_{(1)} + C^i_{(2)}]$. Denote the final state as $\tilde{C}^i_{(1\oplus 2)}$. For the Lagrangian density [2.2], the propagator $K_{(1\oplus 2)}$ of $C^i_{(1\oplus 2)}$ can be written as follows:

$$
\begin{aligned}
K_{(1\oplus 2)} &= \int \mathcal{D}\left[C^i_{(1)} + C^i_{(2)}\right]\left(e^{iS_{(1\oplus 2)}/\hbar}\right) \\
&= \int \mathcal{D}\left[C^i_{(1)} + C^i_{(2)}\right]\left(e^{iS[C^i_{(1)}+C^i_{(2)}]/\hbar}\right) \\
&= \int \mathcal{D}\left[C^i_{(1)} + C^i_{(2)}\right]\left(e^{iS[C^i_{(1)}]/\hbar}\right)^{(1+k^i)^2} \\
&= \int \mathcal{D}\left[C^i_{(1)} + C^i_{(2)}\right]\left(e^{iS[C^i_{(1)}]/\hbar} \cdot e^{iS[C^i_{(2)}]/\hbar} \cdot e^{iS[C^i_{(3)}]/\hbar}\right) \\
&= \frac{1+k^i}{1+k^i+\sqrt{2k^i}} \int \mathcal{D}\left[C^i_{(1)} + C^i_{(2)} + C^i_{(3)}\right]\left(e^{iS[C^i_{(1)}]/\hbar} \cdot e^{iS[C^i_{(2)}]/\hbar} \cdot e^{iS[C^i_{(3)}]/\hbar}\right)
\end{aligned} \tag{2.4}
$$

where the fictitious field $C^i_{(3)} = \sqrt{2k^i} \cdot C^i_{(1)}$.

The factor $\frac{1+k}{1+k+\sqrt{2k}}$, as an overall constant factor, is independent of field configurations and external sources, so it can be eliminated via functional integration when calculating all physical observables, such as correlation functions, scattering cross sections. This factor has no observable physical effects. While it may perturb vacuum fluctuations and related effects, it is not considered in this paper. Therefore, the propagator $K_{(1\oplus 2)}$ associated with the two-source system exhibiting quantum superposition is equivalent to the propagator $K_{(1+2+3)}$ corresponding to the three-source system in the absence of quantum superposition:

$$
\begin{aligned}
K_{(1\oplus 2)} &= K_{(1+2+3)} \\
&= \int \mathcal{D}\left[C^i_{(1)} + C^i_{(2)} + C^i_{(3)}\right]\left(e^{iS[C^i_{(1)}]/\hbar} \cdot e^{iS[C^i_{(2)}]/\hbar} \cdot e^{iS[C^i_{(3)}]/\hbar}\right)
\end{aligned} \tag{2.5}
$$

By comparing Eq. [2.3] and Eq. [2.4], we can see that $K_{(1+2)} \neq K_{(1\oplus 2)}$. This indicates the emergence of a new physical degree of freedom.

Eq. [2.5] implies that the dynamical evolution of a two-source system $C^i_{(1\oplus 2)}$ prepared in a quantum superposition state is formally equivalent to that of a three-source system $C^i_{(1+2+3)}$ without quantum superposition.

In the final state $\tilde{C}^i_{(1+2)}$, provided that the two gravitational sources are separated by a sufficiently large spatial distance, the quantum superposition between the final state $\tilde{C}^i_{(1)}$ and the final state $\tilde{C}^i_{(2)}$ is completely decohered. So it is necessary to introduce the field $\mathcal{C}^i$ to decohere the final state $\tilde{C}^i_{(1\oplus 2)}$ out of quantum superposition into the final state $\tilde{C}^i_{(1+2)}$:

$$
\begin{aligned}
\tilde{C}^i_{(1+2)} &= \tilde{C}^i_{(1\oplus 2)} + \mathcal{C}^i \\
&= \tilde{C}^i_{(1\oplus 2)} - C^i_{(3)} \\
&= \tilde{C}^i_{(1+2+3)} - \sqrt{2k^i}C^i_{(1)}
\end{aligned} \tag{2.6}
$$

where $\mathcal{C}^i = -C^i_{(3)} = -\sqrt{2k^i}C^i_{(1)}$.

Apparently, the energy-momentum tensor of the field $\mathcal{C}^i$ is equal in magnitude to that of the fictitious field $C^i_{(3)}$ but opposite in algebraic sign, so the pressure P and the energy density ρ of the field $\mathcal{C}^i$ is negative: $P < 0,\ \rho < 0$. Assuming that $\mathcal{C}^i$ is a homogeneous and isotropic perfect fluid, the energy-momentum tensor of $\mathcal{C}^i$ can be written as follows:

$$T_{\mu\nu} = \begin{pmatrix} P & & & \\ & P & & \\ & & P & \\ & & & -\rho \end{pmatrix} \tag{2.7}$$

The trace of this energy-momentum tensor is equal to 0:

$$T = \operatorname{tr} T_{\mu\nu} = 0 \tag{2.8}$$

Using natural units, the second Friedmann equation can be written as:

$$\frac{\ddot{a}}{a} = -\frac{4\pi G}{3}(3P + \rho) \tag{2.9}$$

Substitute the pressure and the energy density of the field $\mathcal{C}^i$ into Eq. [2.9], we have:

$$\begin{aligned} \frac{\ddot{a}}{a} &= -\frac{4\pi G}{3}(3P + \rho) \\ &= -\frac{4\pi G}{3}(T + 2\rho) \\ &= -\frac{4\pi G}{3}(2\rho) \end{aligned} \tag{2.10}$$

Since the trace T vanishes and the energy density ρ is negative, the right-hand side of the second Friedmann equation is greater than 0. Therefore, the field $\mathcal{C}^i$ supports the accelerated expansion.

Let us now examine the accelerated expansion from the perspective of contemporary dark energy theories. In the Λ-CDM standard model, the energy-momentum tensor of dark energy can be written as:

$$T_{\mu\nu} = \begin{pmatrix} P_{(DE)} & & & \\ & P_{(DE)} & & \\ & & P_{(DE)} & \\ & & & -\rho_{(DE)} \end{pmatrix} \tag{2.11}$$

where $P_{(DE)}$ and $\rho_{(DE)}$ denote the pressure and energy density of dark energy, respectively. The second Friedmann equation in the Λ-CDM standard model can be written as:

$$\frac{\ddot{a}}{a} = -\frac{4\pi G}{3}(3P_{(DE)} + \rho_{(DE)}) \tag{2.12}$$

In the Λ-CDM standard model, we preset a positive dark energy density: $\rho_{(DE)} > 0$. Therefore, to ensure that the right-hand side of Eq. [2.12] is equal to the right-hand side of Eq. [2.10], the pressure $P_{(DE)}$ is required to be negative and $P_{(DE)} = -\rho_{(DE)}$. The second Friedmann equation can be written as:

$$\begin{aligned} \frac{\ddot{a}}{a} &= -\frac{4\pi G}{3}\big(3P_{(DE)} + \rho_{(DE)}\big) \\ &= -\frac{4\pi G}{3}\big(2P_{(DE)}\big) \\ &= -\frac{4\pi G}{3}\big(-2\rho_{(DE)}\big) \end{aligned} \tag{2.13}$$

Then the EoS parameter in the Λ-CDM standard model is

$$w = \frac{P_{(DE)}}{\rho_{(DE)}} = -1 \tag{2.14}$$

Apparently, within the framework of noncommutative quantum gravity theory, there is no need to introduce any a posteriori assumptions, and the EoS parameter $w = -1$ that previously required artificial predefinition in dark energy theories can be directly derived from first principles.

In the model of the two-source system $C^i_{(1\oplus 2)}$, if the decoherence process acting on the quantum superposition in the final state $\tilde{C}^i_{(1\oplus 2)}$ is incomplete, the energy density associated with the field $\mathcal{C}^i$ will manifest a deviation from its theoretically predicted baseline value. In regions where the quantum effects of the gravitational field are strong, the trace anomaly $T \neq 0$ will modify the value on the right-hand side of Eq.[2.10] . These also offers a theoretically consistent interpretation for the potential deviations of energy density and EoS parameter in dark energy observational studies.

3. Conclusion

Given that the Lagrangian density for the graviton is explicitly formulated within the framework of non-commutative quantum gravity, the Feynman path integral formalism can be employed to evaluate the dynamical evolution of the gravitational field. If there exists quantum superposition between the gravitational fields in the initial state, while no quantum superposition is present in the gravitational fields of the final state, then we need to introduce an auxiliary field $\mathcal{C}^i$ to decohere the final state from its quantum superposition. This field $\mathcal{C}^i$ supports the accelerated expansion. The EoS parameter of dark energy can be derived without invoking any a posteriori assumptions.

REFERENCES

[1] A New Approach to Quantum Gravity. DOI: https://doi.org/10.34257/GJSFRAVOL20IS2PG1

[2] Noncommutative Quantum Gravity and Symmetry of Klein-Gordon Equation. DOI: https://doi.org/10.34257/GJSFRAVOL22IS7PG19

[3] Noncommutative Quantum Gravity and Dark Matter. DOI: https://doi.org/10.34257/GJSFRAVOL23IS4PG7

[4] Macroscopic Effect of Quantum Gravity in General Static Isotropic Gravitational Field. DOI: https://doi.org/10.34257/GJSFRAVOL24IS2PG49

[5] Calculation of Macroscopic Effect of Quantum Gravity in General Static Isotropic Gravitational Field. DOI: https://doi.org/10.34257/GJSFRAVOL24IS4PG75

[6] The Role of Noncommutative Quantum Gravity in Galactic Dynamics and Dark Matter Phenomena. DOI: https://doi.org/10.34257/GJSFRAVOL25IS2PG13

[7] Quantum Superposition and the Emergence of Negative Energy in Gravitational Fields. DOI: https://doi.org/10.34257/GJSFRAVOL25IS5PG19

[8] Quantum Superposition Effect of Gravitational Field, Negative Pressure and Dark Energy. DOI: https://doi.org/10.34257/GJSFRA257434

GLOBAL JOURNAL
OF SCIENCE FRONTIER RESEARCH - A: PHYSICS & SPACE SCIENCE
Volume 26 | Issue 2 | 2026
Article ID: GJSFR-276091
Language: English

The Two Types of Waves Involved in an Electron in a Hydrogen Atom

Article Record

Koshun Suto § ϑ *

ϑ Representative Officer
* Corresponding Author

§ Chudaiji Temple, Isesaki, Japan

RECEIVED	ACCEPTED	ONLINE PUBLISHED	PUBLISHED	PEER REVIEW
2026-08-07	2026-08-17	2026-08-31	2026-09-23	Double Blind

Abstract

Einstein's energy-momentum relationship, holds when the energy absorbed by a body is all converted to kinetic energy of that body. However, an electron in an atom acquires kinetic energy through emission of photon energy. Therefore, Einstein's relationship cannot be applied to an bound electron in an atom. The author has already derived an energy-momentum relationship for an electron in a hydrogen atom. This paper incorporates de Broglie's formula into the above relationship previously derived by the author. Also, if the momentum of an electron in a hydrogen atom is considered using an ellipse, it can be predicted that the electron has two types of momentum and two types of waves. This paper concludes that a moving electron has two types of waves.

compton wavelength | de broglie's formula | einstein's energy-momentum relationship | energy-momentum relationship in a hydrogen atom | fine structure constant | momentum of a electron | momentum of a photon

AI USE STATEMENT
No generative AI was used for analysis or results.

FUNDING
No external funding was declared for this work.

CONFLICT OF INTEREST
The authors declare no conflict of interest.

DATA AVAILABILITY
Not applicable for this article.

ETHICS
No ethics committee approval was required for this article type.

CONSENT
Not applicable for this article.

TRIAL REG.
Not applicable.

Crossref DOI: 10.34257/GJSFRA276091

How to Cite: Suto (2026). The Two Types of Waves Involved in an Electron in a Hydrogen Atom. Global Journal of Science Frontier Research, 26(2), 15-20. DOI: 10.34257/GJSFRA276091

AR Experience Web Page DOI

Print ISSN 0975-5896

Online ISSN 2249-4626

Under the strict compliance and defined process of

ARCHIVAL RECORD

GJSFR · Vol 26 · Issue 2 · 2026

Article ID GJSFR-276091 · DOI 10.34257/GJSFRA276091

Print ISSN 0975-5896 · Online ISSN 2249-4626

Global Journal of Science Frontier Research - Section A
GJSFR Volume 26 Issue 2

The Two Types of Waves Involved in an Electron in a Hydrogen Atom

Koshun Suto § ϑ *

Affiliations
§ Chudaiji Temple, Isesaki, Japan

Qualifications / Designations
ϑ Representative Officer

Abstract

Einstein's energy-momentum relationship, holds when the energy absorbed by a body is all converted to kinetic energy of that body. However, an electron in an atom acquires kinetic energy through emission of photon energy. Therefore, Einstein's relationship cannot be applied to an bound electron in an atom. The author has already derived an energy-momentum relationship for an electron in a hydrogen atom. This paper incorporates de Broglie's formula into the above relationship previously derived by the author. Also, if the momentum of an electron in a hydrogen atom is considered using an ellipse, it can be predicted that the electron has two types of momentum and two types of waves. This paper concludes that a moving electron has two types of waves.

Keywords: *compton wavelength, de broglie's formula, einstein's energy-momentum relationship, energy-momentum relationship in a hydrogen atom, fine structure constant, momentum of a electron, momentum of a photon*

*** Corresponding Author**
Koshun Suto

DOI
10.34257/GJSFRA276091

1. Introduction

N. Bohr was the first to derive the energy levels of a hydrogen atom [1]. Bohr considered the case where an electron moves in a circle at constant speed around the atomic nucleus (a proton). The following formula of motion of Newton holds when an electron moves at velocity v on a circular orbit with radius r.

$$\frac{m_e v^2}{r} = \frac{1}{4\pi\varepsilon_0}\frac{e^2}{r^2}. \tag{1}$$

This formula indicates that the centrifugal force acting on an electron (left side) is equal to the Coulomb attraction exerted on an electron by the atomic nucleus (right side). Here, m_e is the rest mass of the electron.

Multiplying both sides of Formula (1) by 1/2 yields the following.

$$\frac{1}{2}m_e v^2 = \frac{1}{2}\frac{1}{4\pi\varepsilon_0}\frac{e^2}{r}. \tag{2}$$

Incidentally, the potential energy of a hydrogen atom can be expressed with the following formula.

$$V(r) = -\frac{1}{4\pi\varepsilon_0}\frac{e^2}{r}. \tag{3}$$

Therefore, Formula (2) can be written as follows.

$$\frac{1}{2}m_e v^2 = -\frac{1}{2}V(r). \tag{4}$$

Consider the case where an electron at rest in an isolated system in free space is attracted by the electrostatic attraction of the proton (hydrogen atom nucleus), and forms a hydrogen atom.

The electron at rest has a rest mass energy of $m_e c^2$. When this electron is taken into the region of the hydrogen atom, it acquires an amount of kinetic energy K_{re} equivalent to the emitted photon energy $h\nu$.

At this time, the following relationship holds between the kinetic energy K_{re} acquired by the electron and $h\nu$.

$$K_{re} = h\nu. \tag{5}$$

The source supplying these two types of energy is likely to be the rest mass energy of the electron. If the decrease in rest mass energy of the electron is represented here as $-\Delta m_e c^2$, then an energy conservation law like the following holds.

$$-\Delta m_e c^2 + K_{re} + h\nu = 0. \tag{6}$$

Also, by taking Formula (5) into account, Formula (6) can be written as follows.

$$-\Delta m_e c^2 + 2K_{re} = 0. \tag{7}$$

Since the relationship $2K_{re} = -V(r)$ holds due to the virial theorem, Formula (7) can be written as follows.

$$-\Delta m_e c^2 - V(r) = 0. \tag{8}$$

Therefore,

$$V(r) = -\Delta m_e c^2. \tag{9}$$

We have obtained two formulas for the potential energy of an electron.

Formula (9) shows that the potential energy of an electron equals the decrease in rest mass energy of the electron.

Incidentally, Formula (3), the existing formula for potential energy, can be written as follows.

$$V(r) = -\frac{e^2}{4\pi\varepsilon_0 m_e c^2}\frac{m_e c^2}{r} = -m_e c^2 \cdot \frac{r_e}{r}. \tag{10}$$

Also, r_e is the classical electron radius of the electron, given by the following formula.

$$r_e = \frac{1}{4\pi\varepsilon_0}\frac{e^2}{m_e c^2}. \tag{11}$$

When Formula (9) is taken into account, the lower limit for potential energy becomes $-m_e c^2$.

Also, the distance of closest approach r of an electron becomes as follows.

$$r = r_e. \tag{12}$$

The location that satisfies this relationship is the distance of closest approach r, which indicates how close the electron comes to the center of the atom.

When an electron in a hydrogen atom approaches a point r_e from the center of the atomic nucleus, the rest mass energy of the electron is depleted, and the electron cannot approach any closer to the atomic nucleus.

In Formula (3), there was no limit on the range of application of r, but it can be seen that it actually has the following range of application.

$$V(r) = -\frac{1}{4\pi\varepsilon_0}\frac{e^2}{r}, \quad r_e \le r. \tag{13}$$

The radius of the atomic nucleus (proton) in a hydrogen atom is thought to be about $r_e/4$ [2], and thus it is evident that quantum mechanics is not needed to explain the reason why the electron is not absorbed into the atomic nucleus.

In classical quantum theory, the total mechanical energy of a hydrogen atom is defined as the sum of the potential energy and kinetic energy of the electron. That is,

$$E_n = V(r_n) + K_n = -K_n. \tag{14}$$

Here, n is the principal quantum number.

Here, the relativistic energy $m_n c^2$ of an electron, taking into account the existence of the electron's rest mass energy, is defined as follows,

$$m_n c^2 = m_e c^2 + V(r_n) + K_{re,n} = m_e c^2 - K_{re,n} = m_e c^2 + E_{re,n}. \tag{15}$$

Here, $m_n c^2$ is the relativistic energy of the electron, described with an absolute scale.

$m_n c^2$ is the sum of the residual part of the rest mass energy of the electron $(m_e c^2 + V(r_n))$ and the kinetic energy $K_{re,n}$.

Also, $E_{re,n}$ are the relativistic energy levels of a hydrogen atom. The "re" subscript of $E_{re,n}$ stands for "relativistic."

In classical quantum theory, it was promised that the potential energy of an electron placed at the position $r = \infty$ would be zero. It was thought that the energy of an electron in this state would also be zero.

These energies can be illustrated as follows (see Fig. 1).

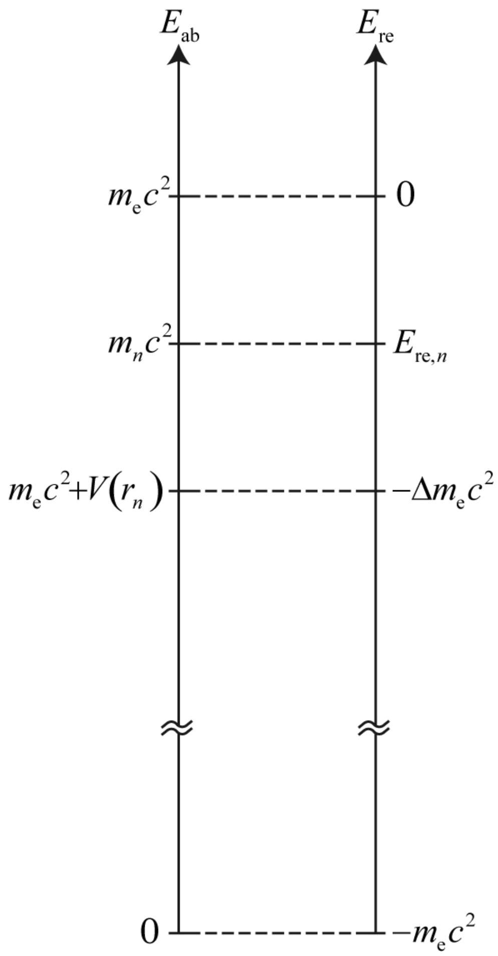

Figure 1. For $E_{re,n}$, the potential energy when the electron is at a position infinitely distant from the atomic nucleus (proton) is set to zero, just as for the energy levels $E_{BO,n}$ of a hydrogen atom derived nonrelativistically by Bohr. The "ab" subscript of E_{ab} stands for "absolute."

However, the energy of an electron placed at an infinitely distant position is not originally zero, it is $m_e c^2$ (however, the potential energy is zero in this case too). Energy in its original sense should be described with an absolute scale. In classical quantum theory, the potential energy of an electron at an infinite distance and the energy of the hydrogen atom are both regarded as zero. However, that idea is mistaken. There is a problem with classical quantum theory which describes the energy levels of a hydrogen atom in relative terms, ignoring the special theory of relativity (STR).

This completes preparations for deriving an energy-momentum relationship applicable to an bound electron in a hydrogen atom.

The author has already derived an energy-momentum relationship applicable to the electron in a hydrogen atom using five types of methods [3, 4, 5, 6, 7, 8]. One of those is reviewed in Section 2.

2. Energy-momentum relationship applicable to an electron in a hydrogen atom

According to the STR, the following relation holds between the energy and momentum of a body moving in free space [9].

$$(mc^2)^2 = (m_0 c^2)^2 + c^2 p^2. \tag{16}$$

Here, m_0c^2 is the rest mass energy of the body. And mc^2 is the relativistic energy.

Incidentally, Einstein and Sommerfeld defined the relativistic kinetic energy as follows [10].

$$K_{\mathrm{re}} = mc^2 - m_0c^2. \tag{17}$$

The "re" subscript of K_{re} stands for "relativistic."

Taking Formula (17) into account, Formula (16) can be rewritten as follows.

$$\begin{aligned} c^2p^2 &= (mc^2 - m_0c^2)(mc^2 + m_0c^2) \\ &= K_{\mathrm{re}}(mc^2 + m_0c^2). \end{aligned} \tag{18}$$

From this, the following formula for relativistic kinetic energy can be derived.

$$K_{\mathrm{re}} = \frac{p_{\mathrm{re}}^2}{m + m_0}. \tag{19}$$

Here, the subscript "re" is attached to p, just as in K_{re}.

Incidentally, Einstein's energy-momentum relationship (16) holds when the energy absorbed by a body is all converted to kinetic energy of that body. However, an electron in an atom acquires kinetic energy through emission of energy. Therefore, Einstein's relationship (16) cannot be applied to an electron in an atom.

Here, the relativistic kinetic energy of an electron inside a hydrogen atom is defined as follows by referring to Formulas (17) and (19).

$$K_{\mathrm{re},n} = m_{\mathrm{e}}c^2 - m_nc^2. \tag{20}$$

$$K_{\mathrm{re},n} = \frac{p_{\mathrm{e},n}^2}{m_{\mathrm{e}} + m_n}. \tag{21}$$

Here, $p_{\mathrm{e},n}$ is the relativistic momentum of the electron. (Due to the situation in this paper, $p_{\mathrm{re},n}$ is rewritten here as $p_{\mathrm{e},n}$.)

The term "relativistic" as used in this paper is not based on the STR. It means that the fact that the mass of the electron changes due to the electron's motion is taken into account. It must be noted that the mass of the electron decreases when the velocity of the electron inside the atom increases [11].

Linking the right sides of Formulas (20) and (21) with an equals sign and rearranging, the following relationship can be derived.

$$(m_nc^2)^2 + c^2p_{\mathrm{e},n}^2 = (m_{\mathrm{e}}c^2)^2. \tag{22}$$

The following formula can be derived from Formula (22).

$$m_nc^2 = m_{\mathrm{e}}c^2\left(1 + \frac{v_n^2}{c^2}\right)^{-1/2}. \tag{23}$$

To change Formula (23) into a formula of quantum theory, the discreteness of energy must be incorporated into Formula (23).

Previously, the author has shown that the following relationship holds for an electron in a hydrogen atom [12, 13].

$$\frac{v_n}{c} = \frac{\alpha}{n}. \tag{24}$$

Here, α is the following fine-structure constant.

$$\alpha = \frac{e^2}{4\pi\varepsilon_0\hbar c} = 7.2973525693 \times 10^{-3}. \tag{25}$$

α is a dimensionless constant introduced by A. Sommerfeld in 1916.

Using the relationship in Formula (24), Formula (23) can be written as follows.

$$m_nc^2 = m_{\mathrm{e}}c^2\left(\frac{n^2}{n^2 + \alpha^2}\right)^{1/2}. \tag{26}$$

Taking Formula (26) into account, $E_{\mathrm{re},n}$ in Formula (15) can be written as follows.

$$E_{\mathrm{re},n} = m_nc^2 - m_{\mathrm{e}}c^2 = m_{\mathrm{e}}c^2\left[\left(\frac{n^2}{n^2 + \alpha^2}\right)^{1/2} - 1\right], \quad n = 0, 1, 2, \ldots \tag{27}$$

Formula (27) gives the energy levels of a hydrogen atom, taking relativity into account (see Fig. 2).

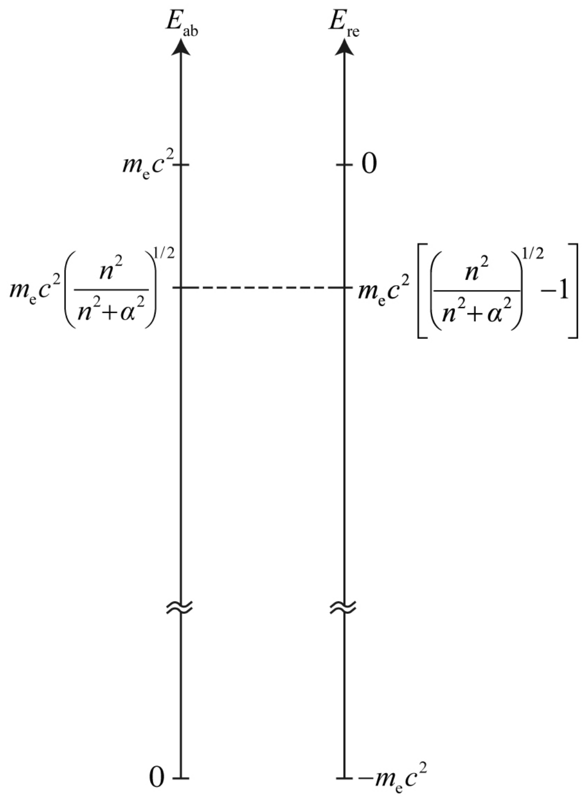

Figure 2. In this figure, the energies in Figure 1, m_nc^2 and $E_{\mathrm{re},n}$, have been rewritten using Formulas (26) and (27).

Formula (27) predicts the existence of a state with $n = 0$ [14].

Next, when the part of Formula (27) in parentheses is expressed as a Taylor expansion,

$$\begin{aligned} E_{\mathrm{re},n} &\approx m_{\mathrm{e}}c^2\left[\left(1 - \frac{\alpha^2}{2n^2} + \frac{3\alpha^4}{8n^4} - \frac{5\alpha^6}{16n^6}\right) - 1\right] \\ &\approx -\frac{\alpha^2 m_{\mathrm{e}}c^2}{2n^2}. \end{aligned} \tag{28}$$

Incidentally, the nonrelativistic energy levels of a hydrogen atom, derived by Bohr, are given by the following formula.

$$E_{\mathrm{BO},n} = -\left(\frac{1}{4\pi\varepsilon_0}\right)^2\frac{m_{\mathrm{e}}e^4}{2\hbar^2}\cdot\frac{1}{n^2}, \quad n = 0, 1, 2, \ldots. \tag{29}$$

However, when discussing the energy levels of a hydrogen atom, it is best if the rest mass energy of the electron is included in the formula. Thus Formula (29) is rewritten as follows.

$$E_{\mathrm{BO},n} = -\frac{m_e c^2}{2}\left(\frac{e^2}{4\pi\varepsilon_0 \hbar c}\right)^2 \frac{1}{n^2} = -\frac{\alpha^2 m_e c^2}{2n^2}, \quad n = 0, 1, 2, \ldots. \tag{30}$$

From this, it is evident that Formula (29) is an approximation of Formula (27).

Next, Table 1 summarizes the energies of a hydrogen atom obtained from Formulas (27) and (29) (see Table 1).

Table 1. Comparison of the energies of a hydrogen atom predicted by Bohr's classical quantum theory and this paper

n	Bohr's Energy Levels, $E_{\mathrm{BO},n}$	This Paper, $E_{\mathrm{re},n}$
0	—	-0.511 MeV
1	-13.6057 eV	-13.6052 eV
2	-3.4014 eV	-3.4014 eV
3	-1.51174 eV	-1.51174 eV

Now, in preparation for the discussion in Section 3, let us rewrite Formula (22) as a relationship for momentum. To do that, it is enough to divide both sides of Formula (22) by c^2. That is,

$$(m_n c)^2 + p_{e,n}^2 = (m_e c)^2. \tag{31}$$

3. Physical quantities of electrons revealed by considering an ellipse

Formula (31) can be derived through considerations using an ellipse. This problem has already been discussed [7, 8].

However, at that time, the electron's energy was discussed using an ellipse. In this paper, the momentum of an electron is discussed using an ellipse. By nature, energy is a scalar, but momentum is a vector. In discussion using an ellipse, it is thought better to focus on momentum than energy.

Let A and A′ be the points where the ellipse intersects the x-axis, and let B and B′ be the points where the ellipse intersects the y-axis. Also, let $2a$ be the length of the line segment $\overline{AA'}$, $2b$ be the length of the line segment $\overline{BB'}$, and $2f$ be the length of the line segment $\overline{FF'}$ (see Fig. 3).

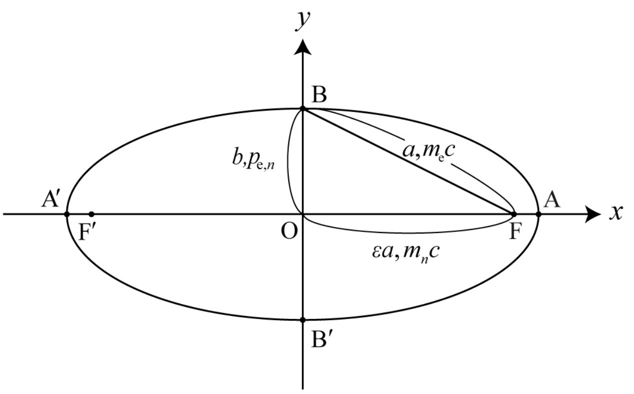

Figure 3. First, the momentum $m_e c$ is taken to correspond to the line segment $\overline{OA}$, and then Formula (35) is assumed. Formula (31) can be derived if the Pythagorean theorem is applied to the right triangle $\triangle OBF$.

The reason why discussion using an ellipse is valid is likely because the momentum vector of the electron is orthogonal to the momentum vector of the photon possessed by the electron.

The eccentricity of the ellipse in this case is defined as follows.

$$\varepsilon = \frac{f}{a}. \tag{32}$$

The eccentricity of the ellipse can also be expressed using the following formula.

$$\varepsilon = \left(1 - \frac{b^2}{a^2}\right)^{1/2}. \tag{33}$$

The following formula can be derived from Formula (33).

$$b = a(1 - \varepsilon^2)^{1/2}. \tag{34}$$

Here, the line segment $\overline{OA}$ is placed into correspondence with the momentum $m_e c$.

Let us express this as follows.

$$a = m_e c. \tag{35}$$

Also, it is assumed that the shape of an ellipse that can describe the state of an electron is the case satisfying the following conditions.

$$\varepsilon_n = \left(\frac{n^2}{n^2 + \alpha^2}\right)^{1/2}. \tag{36}$$

Taking Formulas (35) and (36) into account, b can be expressed with the following formula.

$$b = m_e c\left(\frac{\alpha^2}{n^2 + \alpha^2}\right)^{1/2}. \tag{37}$$

Also, if Formula (35) and Formula (36) are taken into account, then the f in Formula (32) is as follows.

$$f = a\varepsilon = m_e c\left(\frac{n^2}{n^2 + \alpha^2}\right)^{1/2}. \tag{38}$$

Using Formulas (37) and (38),

$$f^2 + b^2 = \left(\frac{n^2 + \alpha^2}{n^2}\right)(m_e c)^2 + \left(\frac{\alpha^2 + \alpha^2}{\alpha^2}\right)(m_e c)^2 = (m_e c)^2. \tag{39}$$

Here, $\overline{BF} = a$, so the following relationship holds.

$$\overline{OA} = \overline{BF}. \tag{40}$$

Here, if Formula (26) is also taken into consideration, then Formula (37) can be expressed as follows.

$$b^2 = \left(\frac{\alpha^2}{n^2 + \alpha^2}\right) m_e^2 c^2 = \left(\frac{\alpha^2}{n^2 + \alpha^2}\right) m_n^2 \left(\frac{n^2 + \alpha^2}{n^2}\right) c^2. \tag{41}$$

Furthermore, if the relationship in Formula (24) is used for c in Formula (41), the result is as follows.

$$b^2 = \frac{\alpha^2}{n^2} \cdot m_n^2 \frac{n^2 v_n^2}{\alpha^2} = (m_n v_n)^2 = p_{e,n}^2. \tag{42}$$

Substituting this result for Formula (42) into Formula (39),

$$f^2 + b^2 = (m_n c)^2 + p_{e,n}^2 = (m_e c)^2. \tag{43}$$

When $m_e c$ is taken to correspond to the line segment $\overline{OA}$, and Formula (36) is assumed, then Formula (31) can be derived from the right triangle OBF.

The purpose of the considerations using an ellipse in this section was to show that Formula (31) can be derived using multiple methods.

In past discussions, the ellipse line segment was taken to correspond to energy (a scalar), but in this paper the line segment was taken to correspond to momentum (a vector). The discussion in this paper is not a repetition of that past discussion.

4. Discussion

It is known that the momentum and wavelength of an electron have the following relation.

$$p = \frac{h}{\lambda}. \tag{44}$$

Here, if the momentum of the photon possessed by an electron in a state with principal quantum number n is $p_{p,n}$, and the momentum of a moving electron is $p_{e,n}$, then these two types of momentum can be expressed as follows.

$$p_{p,n} = m_n c = m_e c\left(\frac{n^2}{n^2+\alpha^2}\right)^{1/2} = \frac{h}{\lambda_{p,n}}. \tag{45}$$

$$p_{e,n} = m_n v_n = m_e c\left(\frac{\alpha^2}{n^2+\alpha^2}\right)^{1/2} = \frac{h}{\lambda_{e,n}}. \tag{46}$$

Here, $\lambda_{p,n}$ is the wavelength of a photon whose momentum is $p_{p,n}$, and $\lambda_{e,n}$ is the wavelength of an electron whose momentum is $p_{e,n}$.

From the above it can be predicted that a moving electron has two types of waves.

Also, the following formula can be obtained from the definition of the Planck constant [15].

$$m_e c = \frac{h}{\lambda_C}. \tag{47}$$

Here, λ_C is the Compton wavelength of the electron.

The following relationship can be derived by substituting the three types of momentum in Formulas (45) to (47) into Formula (31) and rearranging [16].

$$\frac{1}{\lambda_{p,n}^2} + \frac{1}{\lambda_{e,n}^2} = \frac{1}{\lambda_C^2}. \tag{48}$$

Formula (48) holds because Formula (22) holds.

The three wavelengths in Formula (48) can be put into correspondence with the line segments of the ellipse in Figure 3 (see Fig. 4).

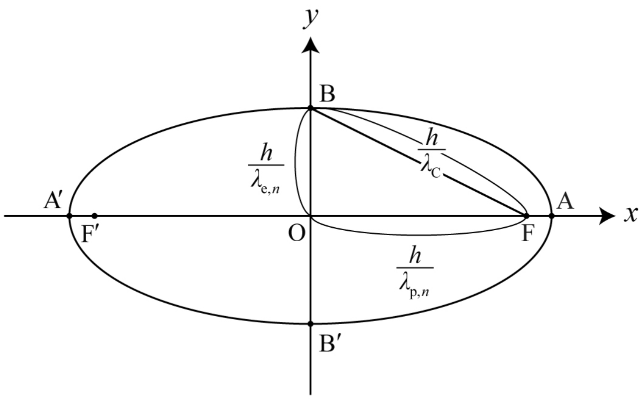

Figure 4. In this figure, the momentum in Figure 3 is represented with a formula including wavelength, by using de Broglie's formula $p = h/\lambda$. Therefore, it can be predicted that the wave attributable to the electron's momentum and the wave of the photon possessed by the electron are orthogonal, and they exist independently of each other.

From Figure 4, it is evident that the following two relationships hold [17].

$$\frac{\overline{OB}}{\overline{OF}} = \frac{m_n v_n}{m_n c} = \frac{p_{e,n}}{p_{p,n}} = \frac{\alpha}{n}. \tag{49}$$

$$\frac{\overline{OB}}{\overline{OF}} = \frac{h/\lambda_{e,n}}{h/\lambda_{p,n}} = \frac{\lambda_{p,n}}{\lambda_{e,n}}. \tag{50}$$

The following relationship can be derived from Formula (49) and Formula (50).

$$\frac{v_n}{c} = \frac{m_n v_n}{m_n c} = \frac{p_{e,n}}{p_{p,n}} = \frac{\lambda_{p,n}}{\lambda_{e,n}} = \frac{\alpha}{n}. \tag{51}$$

The physically permitted ellipses are limited only to those that satisfy the following condition.

$$\frac{\lambda_{p,n}}{\lambda_{e,n}} = \frac{\alpha}{n}. \tag{52}$$

In the case where $n = 1$,

$$\frac{\lambda_{p,1}}{\lambda_{e,1}} = \alpha. \tag{53}$$

This paper concludes that Formula (24) holds because Formula (52) holds. Thus the quantum condition is Formula (52) not Formula (24).

The fine structure constant α has previously been understood as the ratio of the velocity of an electron, as the particle in the ground state of a hydrogen atom, and the speed of light. However, it was not understood why the ratio of the two is so important for physics.

However, if the electron is considered as a wave, the fine structure constant can be understood as the ratio of the wavelength $\lambda_{p,1}$ of light possessed by an electron in the ground state and the wavelength $\lambda_{e,1}$ of a moving electron [18].

In the micro world, it is thought that treatment of wavelengths of electrons as waves is preferable to treatment of velocities of electrons as particles. It has already been known that $v_1 = \alpha c$, but this paper has promoted Formula (52) to a quantum condition.

This paper predicts that the momentum vector attributable to the electron's motion is orthogonal to the momentum vector of the photon possessed by the electron.

5. Conclusion

The author previously derived Formula (22), a relationship applicable to the electron in a hydrogen atom, in place of Einstein's energy-momentum relationship. Formula (22) also serves as a momentum relationship like the following.

$$(m_n c)^2 + p_{e,n}^2 = (m_e c)^2. \tag{54}$$

$$p_{p,n}^2 + p_{e,n}^2 = (m_e c)^2. \tag{55}$$

Next, by applying de Broglie's formula, the three types of momentum in Formula (55) can be written as follows.

$$p_{p,n} = \frac{h}{\lambda_{p,n}}. \tag{56}$$

$$p_{e,n} = \frac{h}{\lambda_{e,n}}. \tag{57}$$

$$m_e c = \frac{h}{\lambda_C}. \tag{58}$$

Then the following relationship can be derived by substituting these momenta into Formula (55).

$$\frac{1}{\lambda_{p,n}^2} + \frac{1}{\lambda_{e,n}^2} = \frac{1}{\lambda_C^2}. \tag{59}$$

It has been well-known for more than a century that electrons, which were thought to be particles, also have a wave nature. However, this paper concludes, while also taking into account Figure 4, that the waves involved with the electrons in hydrogen atoms actually have two types rather than one type.

The relationship in Formula (59) holds between the wavelengths $\lambda_{p,n}$ and $\lambda_{e,n}$ of the two waves possessed by the electron. Assuming that these two waves exist independently, it can be predicted that the two are orthogonal.

ACKNOWLEDGEMENTS

I would like to express my thanks to the staff at ACN Translation Services for their translation assistance. Also, I wish to express my gratitude to Mr. H. Shimada for drawing figures.

REFERENCES

[1] N. Bohr, "On the Constitution of Atoms and Molecules". Philosophical Magazine, 26, 1, (1913). https://doi.org/10.1080/14786441308634955

[2] P. Randolf, "Size of the Proton". Nature, 466, 213-216, (2010).

[3] K. Suto, "An Energy-Momentum Relationship for a Bound Electron Inside a Hydrogen Atom". Physics Essays, 24, 301-307, (2011). https://koshun129.sakura.ne.jp/physics/4spw_index.html

[4] K. Suto, "Derivation of a Relativistic Wave Equation More Profound than Dirac's Relativistic Wave Equation". Applied Physics Research, 10, 102-108, (2018). https://doi.org/10.5539/apr.v10n6p102

[5] K. Suto, "Theoretical Prediction of Negative Energy Specific to the Electron". Journal of Modern Physics, 11, 712-724, (2020). https://doi.org/10.4236/jmp.2020.115046

[6] K. Suto, "Previously Unknown Formulas for the Relativistic Kinetic Energy of an Electron in a Hydrogen Atom". Journal of Applied Mathematics and Physics, 11, 972-987, (2023). https://doi.org/10.4236/jamp.2023.114065

[7] K. Suto, "The Strange Relationship Between the Momentum of a Photon Emitted from an Electron and the Momentum Acquired by the Electron". Journal of Applied Mathematics and Physics, 12, 2652-2664, (2024). https://doi.org/10.4236/jamp.2024.127157

[8] K. Suto, "The Photon Energy of an Electron with Rest Mass Energy of $m_e c^2$ is $2m_e c^2$". Applied Physics Research, 17, 44-56, (2025). https://doi.org/10.5539/apr.v17n1p44

[9] A. Einstein, Relativity. Crown, New York, 43, (1961).

[10] A. Sommerfeld, "Atomic Structure and Spectral Lines". Methuen & Co. Ltd., London, 528, (1923).

[11] K. Suto, "Electron Mass in an Atom Is Less than Rest Mass". Journal of Applied Mathematics and Physics, 11, 3953-3961, (2023). https://doi.org/10.4236/jamp.2023.1112252

[12] K. Suto, "The Relationship Enfolded in Bohr's Quantum Condition and a Previously Unknown Formula for Kinetic Energy". Applied Physics Research, 11, 19-34, (2019). https://doi.org/10.5539/apr.v11n1p19

[13] K. Suto, "The Quantum Condition That Should Have Been Assumed by Bohr When Deriving the Energy Levels of a Hydrogen Atom". Journal of Applied Mathematics and Physics, 9, 1230-1244, (2021). https://doi.org/10.4236/jamp.2021.96084

[14] K. Suto, "An Energy Level with Principal Quantum Number n=0 Exists in a Hydrogen Atom". London Journal of Research in Science, Natural and Formal, 23, 2, 1.0, 65-79, (2023). https://journalspress.com/LJRS_Volume23/An-Energy-Level-with-Principal-Quantum-Number-n-0-Exists-in-a-Hydrogen-Atom.pdf

[15] K. Suto, "The Planck Constant Was Not a Universal Constant". Journal of Applied Mathematics and Physics, 8, 456-463, (2020). https://doi.org/10.4236/jamp.2020.83035

[16] K. Suto, "Energy-Momentum Relationship Applicable to an Electron inside a Hydrogen Atom". Global Journal of Science Frontier Research-A: Physics&Space Science, 26, 1-5, (2026). DOI: 10.34257/GJSFRA258904

[17] K. Suto, "Elucidating the Nature of the Fine Structure Constant and Indicating the Existence of an Unknown Angular Momentum". Applied Physics Research, 9, 3, 17-22, (2017). https://doi.org/10.5539/apr.v9n3p17

[18] K. Suto, "A Surprising Physical Quantity Involved in the Phase Velocity and Energy Levels of the Electron in a Hydrogen Atom". Applied Physics Research, 14, 2, 1-17, (2022). https://doi.org/10.5539/apr.v14n2p1

GLOBAL JOURNAL
OF SCIENCE FRONTIER RESEARCH - A: PHYSICS & SPACE SCIENCE
Volume 26 | Issue 2 | 2026 Article ID: GJSFR-259211 Language: English

CATALOGING
PACS • 98.80.Es MSC • 85A40

The Hubble Tension: A Review of Early- and Late-Universe Determinations of the Cosmic Expansion Rate and Proposed Theoretical Resolutions

Article Record

Dr. Rajesh Kumar Mishra § *
*Corresponding Author

Divyansh Mishra ‡

§ Tropical Forest Research Institute, Jabalpur, India (OA)
‡ Xavier School of Management, Jamshedpur, India (OA)
+1 additional authors listed on the metadata continuation page.

RECEIVED	ACCEPTED	ONLINE PUBLISHED	PUBLISHED	PEER REVIEW
2026-07-14	2026-07-23	2026-08-13	2026-09-23	Double Blind

Abstract

The Hubble constant, H0, quantifies the present-day expansion rate of the universe and anchors the cosmic distance scale, the inferred age of the universe, and the dark-energy equation of state. Two independent families of measurement now disagree at a formal significance exceeding 5σ: early-universe inferences from the cosmic microwave background (CMB) and baryon acoustic oscillations (BAO), analyzed within the standard ΛCDM model, yield H0 ≈ 67–68 km s^{-1} Mpc^{-1}, whereas a broad ensemble of late-universe, largely distance-ladder-based measurements cluster around H0 ≈ 70–75 km s^{-1} Mpc^{-1}. This review traces the history of H0 measurement, summarizes the theoretical framework relating H0 to the sound horizon and the expansion history, and synthesizes more than a dozen independent early- and late-universe determinations, including distance-ladder, geometric, gravitational-lensing, gravitational-wave, cosmic-chronometer, and quasar-based methods. It tabulates their central values and uncertainties, traces the systematic-error investigations — including recent James Webb Space Telescope Cepheid photometry and revised strong-lensing mass-profile modeling — that have narrowed but not eliminated plausible mundane explanations, and quantifies the statistical robustness of the tension across the full measurement ensemble. It then evaluates the principal theoretical proposals for reconciling the two regimes, spanning early dark energy, evolving dark-energy equations of state motivated by recent DESI results, modified gravity, interacting dark-sector models,

cosmic chronometers | cosmic distance ladder | cosmic microwave background | Cosmology | Dark energy | gravitational lensing | Hubble constant

AI USE STATEMENT
No generative AI was used for analysis or results.

FUNDING
No external funding was declared for this work.

CONFLICT OF INTEREST
The authors declare no conflicts of interest.

DATA AVAILABILITY
Not applicable for this article.

ETHICS
No ethics committee approval was required for this article type.

CONSENT
Not applicable for this article.

TRIAL REG.
Not applicable.

Crossref DOI: 10.34257/GJSFRA259211

How to Cite: Mishra et al. (2026). The Hubble Tension: A Review of Early- and Late-Universe Determinations of the Cosmic Expansion Rate and Proposed Theoretical Resolutions. Global Journal of Science Frontier Research, 26(2), 21-27. DOI: 10.34257/GJSFRA259211

AR Experience Web Page DOI

Print ISSN 0975-5896

Online ISSN 2249-4626

METADATA CONTINUATION

AUTHOR CONTACT QR LEDGER

Dr. Rajesh Kumar Mishra

Divyansh Mishra

Rekha Agarwal

COMPLETE AUTHOR LEDGER

01. Dr. Rajesh Kumar Mishra §* | Tropical Forest Research Institute, Jabalpur, India
02. Divyansh Mishra ‡ | Xavier School of Management, Jamshedpur, India
03. Rekha Agarwal ¶ | Government Science College, Jabalpur, India

FULL ABSTRACT

The Hubble constant, H0, quantifies the present-day expansion rate of the universe and anchors the cosmic distance scale, the inferred age of the universe, and the dark-energy equation of state. Two independent families of measurement now disagree at a formal significance exceeding 5σ: early-universe inferences from the cosmic microwave background (CMB) and baryon acoustic oscillations (BAO), analyzed within the standard ΛCDM model, yield H0 $\approx$ 67–68 km s ^{1} Mpc ^{1}, whereas a broad ensemble of late-universe, largely distance-ladder-based measurements cluster around H0 $\approx$ 70–75 km s ^{1} Mpc ^{1}. This review traces the history of H0 measurement, summarizes the theoretical framework relating H0 to the sound horizon and the expansion history, and synthesizes more than a dozen independent early- and late-universe determinations, including distance-ladder, geometric, gravitational-lensing, gravitational-wave, cosmic-chronometer, and quasar-based methods. It tabulates their central values and uncertainties, traces the systematic-error investigations — including recent James Webb Space Telescope Cepheid photometry and revised strong-lensing mass-profile modeling — that have narrowed but not eliminated plausible mundane explanations, and quantifies the statistical robustness of the tension across the full measurement ensemble. It then evaluates the principal theoretical proposals for reconciling the two regimes, spanning early dark energy, evolving dark-energy equations of state motivated by recent DESI results, modified gravity, interacting dark-sector models, and ladder-wide systematics, assessing each against current observational constraints in a summary comparison table. We conclude that the tension is unlikely to be resolved by any single known systematic and outline the observational programs — the Vera C. Rubin Observatory, Euclid, the Nancy Grace Roman Space Telescope, and next-generation gravitational-wave detectors — most likely to discriminate among the competing explanations over the coming decade.

ARCHIVAL RECORD

GJSFR · Vol 26 · Issue 2 · 2026

Article ID GJSFR-259211 · DOI 10.34257/GJSFRA259211

Print ISSN 0975-5896 · Online ISSN 2249-4626

Global Journal of Science Frontier Research - Section A
GJSFR Volume 26 Issue 2

The Hubble Tension: A Review of Early- and Late-Universe Determinations of the Cosmic Expansion Rate and Proposed Theoretical Resolutions

Dr. Rajesh Kumar Mishra§ *, Divyansh Mishra‡, and Rekha Agarwal¶

Affiliations
§ Tropical Forest Research Institute, Jabalpur, India (OA)
‡ Xavier School of Management, Jamshedpur, India (OA)
¶ Government Science College, Jabalpur, India

Abstract

The Hubble constant, H0, quantifies the present-day expansion rate of the universe and anchors the cosmic distance scale, the inferred age of the universe, and the dark-energy equation of state. Two independent families of measurement now disagree at a formal significance exceeding 5σ: early-universe inferences from the cosmic microwave background (CMB) and baryon acoustic oscillations (BAO), analyzed within the standard ΛCDM model, yield H0 ≈ 67–68 km s^{-1} Mpc^{-1}, whereas a broad ensemble of late-universe, largely distance-ladder-based measurements cluster around H0 ≈ 70–75 km s^{-1} Mpc^{-1}. This review traces the history of H0 measurement, summarizes the theoretical framework relating H0 to the sound horizon and the expansion history, and synthesizes more than a dozen independent early- and late-universe determinations, including distance-ladder, geometric, gravitational-lensing, gravitational-wave, cosmic-chronometer, and quasar-based methods. It tabulates their central values and uncertainties, traces the systematic-error investigations — including recent James Webb Space Telescope Cepheid photometry and revised strong-lensing mass-profile modeling — that have narrowed but not eliminated plausible mundane explanations, and quantifies the statistical robustness of the tension across the full measurement ensemble. It then evaluates the principal theoretical proposals for reconciling the two regimes, spanning early dark energy, evolving dark-energy equations of state motivated by recent DESI results, modified gravity, interacting dark-sector models, and ladder-wide systematics, assessing each against current observational constraints in a summary comparison table. We conclude that the tension is unlikely to be resolved by any single known systematic and outline the observational programs — the Vera C. Rubin Observatory, Euclid, the Nancy Grace Roman Space Telescope, and next-generation gravitational-wave detectors — most likely to discriminate among the competing explanations over the coming decade.

Keywords: *cosmic chronometers, cosmic distance ladder, cosmic microwave background, Cosmology, Dark energy, gravitational lensing, Hubble constant, Hubble tension, standard sirens, ΛCDM*

* **Corresponding Author**
Dr. Rajesh Kumar Mishra

DOI
10.34257/GJSFRA259211

1. Introduction

1.1. Historical background

Edwin Hubble's 1929 discovery that the recession velocity of galaxies scales linearly with distance established the expansion of the universe and defined the constant of proportionality, H0, that bears his name; Hubble's original estimate, roughly 500 km s^{-1} Mpc^{-1}, was later found to be too large by nearly an order of magnitude because of systematic errors in his distance calibration, a reminder that the history of H0 measurement is itself a history of identifying and correcting subtle systematics. Through the mid-to-late twentieth century, the value of H0 was the subject of a prolonged and often personal dispute, most famously between Allan Sandage, who favored values near 50 km s^{-1} Mpc^{-1}, and Gérard de Vaucouleurs, who favored values near 100 km s^{-1} Mpc^{-1}. This factor-of-two disagreement was substantially resolved by the HST Key Project in the early 2000s, which used Cepheid variables to calibrate multiple secondary distance indicators and converged on H0 = 72 ± 8 km s^{-1} Mpc^{-1}. It is against this backdrop that the modern tension, at the ~7% level between early- and late-universe probes, should be judged: it is a far smaller discrepancy than the Sandage–de Vaucouleurs dispute, but the measurements on each side are now individually precise enough that the discrepancy is statistically much more significant.

1.2. The modern tension

Over the last decade a statistically significant discrepancy has re-emerged between two broad classes of H0 determination. Measurements that rely on the physics of the early universe — the acoustic oscillations imprinted in the CMB and in the large-scale distribution of galaxies — combined with the assumption that the universe is well described by the flat ΛCDM model, consistently return H0 ≈ 67–68 km s^{-1} Mpc^{-1}. Measurements that instead build a distance ladder through the local universe, or that measure distances geometrically and independently of any ladder, cluster in the range H0 ≈ 70–75 km s⁻¹ Mpc⁻¹. Taken together, the two regimes now disagree at a level reported between 4σ and 6σ depending on the specific datasets combined, a discrepancy widely termed the "Hubble tension." Unlike earlier cosmological disputes that were resolved by additional data revealing a systematic error on one side, the Hubble tension has hardened as measurement precision has improved on both sides, which is one of the principal reasons it is now taken seriously as a possible signal of physics beyond ΛCDM rather than as a transient calibration problem.

This review has five aims: to place the tension in historical context and summarize the theoretical framework relating H0 to the sound horizon and cosmic expansion history; to summarize the principal early-universe and late-universe methods for determining H0, including several less commonly reviewed techniques; to tabulate and compare the resulting values directly; to review the systematic-error investigations that have progressively closed off mundane explanations for the tension; and to survey and critically assess the leading theoretical proposals advanced to reconcile the two regimes.

2. Scope and method of this review

This review synthesizes results from the primary cosmological literature published between approximately 2002 and 2026, prioritizing measurements from large collaborations (Planck, DESI, SH0ES, H0LiCOW/TDCOSMO, the Megamaser Cosmology Project) and recent independent cross-checks, including JWST-based recalibrations of the distance ladder. It is restricted to determinations of the present-day Hubble parameter, H0, and does not attempt to cover the related but distinct S8/σ8 tension in the amplitude of matter clustering, except where a proposed resolution explicitly links the two. Numerical values are quoted as reported in the cited sources, generally at 68% confidence, and readers requiring the most current figures are directed to the original works, since this remains an actively evolving field in which central values shift by fractions of their quoted uncertainty from one data release to the next.

3. Theoretical framework

In the standard Friedmann-Lemaître-Robertson-Walker (FLRW) cosmology, the expansion rate at redshift z is governed by the Friedmann equation,

$$H(z)^2 = H_0^2[\Omega_m(1+z)^3 + \Omega_r(1+z)^4 + \Omega_\Lambda] \quad \text{(flat ΛCDM)},$$

where Ω_m, Ω_r, and Ω_Λ are the present-day fractional densities of matter, radiation, and dark energy. $H_0 = H(z=0)$ is therefore not an independent free parameter of the theory in the same sense as Ω_m; rather, it is the normalization that fixes the absolute scale of distances and times once the shape of $H(z)$ has been determined.

Early-universe methods measure H_0 indirectly, via the sound horizon at the drag epoch,

$$r_s = \int [c_s(z)/H(z)]\, dz, \quad \text{integrated from } z = z_{\text{drag}} \text{ to } z \to \infty,$$

where $c_s(z)$ is the sound speed of the pre-recombination photon-baryon fluid. The CMB and BAO observations measure the angular or comoving scale of this standard ruler on the sky; since r_s itself is fixed by well-understood early-universe microphysics (the baryon and photon densities), converting an observed angular scale into H_0 requires assuming a specific expansion history, $H(z)$, between the drag epoch and today — which is precisely the ΛCDM assumption under scrutiny. Any new physics that changes r_s, or that changes $H(z)$ at low redshift relative to ΛCDM, will change the inferred H_0 without requiring any flaw in the CMB or BAO data themselves.

Late-universe, distance-ladder methods instead measure H_0 directly and locally, via the Hubble-Lemaître law in its differential form,

$$v = H_0 d$$

(in the limit of small z, after correcting for peculiar velocities),

using a luminosity distance, d, established through a chain of geometric and standard-candle calibrators. This route requires no assumption about the expansion history at high redshift, but it does require that each rung of the distance ladder — geometric parallax or maser distances, the Cepheid (or TRGB/JAGB) period–luminosity or luminosity-cutoff relation, and the SN Ia standardization relation — be free of unrecognized systematics. The theoretical asymmetry between the two routes is central to interpreting the tension: the early-universe route is precise but model-dependent, while the late-universe route is comparatively model-independent but depends on a longer chain of empirical calibrations.

4. Early-universe determinations of H0

The most precise early-universe determination of H0 comes from the CMB temperature and polarization anisotropy power spectra measured by the Planck satellite. Within the flat ΛCDM model, the physical scale of the sound horizon at recombination, rs, is fixed by the pre-recombination physics of the photon-baryon fluid, and its observed angular size on the sky, combined with the angular-diameter distance to the last-scattering surface, jointly determine H0. This chain yields H0 = 67.4 ± 0.5 km s⁻¹ Mpc⁻¹ (Planck Collaboration, 2020). Because this inference depends on extrapating the flat ΛCDM model from redshift z ≈ 1100 to the present day, it is properly described as an indirect, model-dependent measurement rather than a direct one: any new physics that alters the sound horizon or the late-time expansion history relative to ΛCDM would change the inferred H0 without requiring any error in the Planck data itself.

An independent early-universe route combines baryon acoustic oscillation (BAO) measurements of the three-dimensional galaxy distribution with the sound horizon calibrated by Big Bang nucleosynthesis (BBN), bypassing the CMB entirely. The Dark Energy Spectroscopic Instrument (DESI) has produced BAO measurements spanning a wide range of redshifts from its DR1 and DR2 releases; combined with BBN-calibrated physical baryon and matter densities, these measurements return an H0 consistent with the Planck result, reinforcing the early-universe value at approximately 67–68 km s⁻¹ Mpc⁻¹ (DESI Collaboration, 2025). The mutual agreement of two independent early-universe probes — CMB anisotropies and BAO+BBN — that rely on largely independent systematics is one of the strongest arguments that the tension does not simply reflect an error internal to the Planck analysis pipeline.

A further, still-developing early-universe channel uses the DESI BAO measurements themselves to test the flat ΛCDM assumption. Several DESI DR1/DR2 analyses report a mild statistical preference, at the 2–3σ level depending on the supernova compilation used, for a dark-energy equation of state that departs from w = −1 and evolves with redshift. If confirmed, this would mean that the "early-universe" H0 value is itself model-dependent in a way not previously appreciated, since it is derived assuming a specific, and possibly incorrect, late-time expansion history (DESI Collaboration, 2025).

5. Late-universe determinations of H0

5.1. Cepheid-calibrated distance ladder

The traditional route to a direct, local measurement of H0 is the three-rung cosmic distance ladder: geometric parallax and detached-eclipsing-binary (DEB) distances calibrate the Cepheid period–luminosity relation, Cepheids calibrate the peak luminosity of Type Ia supernovae (SNe Ia) in their host galaxies, and those supernovae are then observed out to distances where the smooth Hubble flow dominates over local peculiar velocities. The first rung is anchored primarily by DEB distances to the Large Magellanic Cloud (LMC), Milky Way Cepheid parallaxes from Gaia, and megamaser and DEB distances to NGC 4258. Using this method, the SH0ES (Supernovae and H0 for the Equation of State of dark energy) collaboration reports H0 = 73.04 ± 1.04 km s^{-1} Mpc^{-1} (Riess et al., 2022), and an extended calibrator sample re-observed with JWST gives a consistent H0 = 72.6 ± 2.0 km s^{-1} Mpc^{-1} (Riess et al., 2024). The quoted 1.4% uncertainty on the SH0ES value is dominated by the combination of all four anchor distances and the SN Ia standardization scatter, rather than by any single rung.

5.2. TRGB and JAGB calibrations

Alternative first-rung calibrators give a more heterogeneous picture. The Tip of the Red Giant Branch (TRGB) method, applied by the Carnegie-Chicago Hubble Program, calibrates SN Ia hosts using the sharp luminosity cutoff of red giant stars rather than Cepheids, and returns a somewhat lower value, H0 = 69.6 ± 1.9 km s^{-1} Mpc^{-1} (Freedman et al., 2019, 2020), statistically consistent with both the Planck and SH0ES results within its larger uncertainty. The related J-region Asymptotic Giant Branch (JAGB) method gives comparable intermediate values when applied to the same calibrator hosts. Because TRGB and JAGB distances are measured in the outer haloes of galaxies and are largely insensitive to interstellar dust and to the Cepheid period-luminosity relation's known metallicity dependence, their intermediate placement suggests that at least part of the reported spread among late-universe measurements may trace to the choice of stellar distance indicator and its associated systematics, rather than to new physics.

5.3. Geometric and standard-candle methods independent of Cepheids

Several methods measure H0 without any Cepheid calibration. The Megamaser Cosmology Project uses the geometry of water-maser disks orbiting supermassive black holes to obtain purely geometric distances to the host galaxies, yielding H0 = 73.9 ± 3.0 km s^{-1} Mpc^{-1} (Pesce et al., 2020). The surface brightness fluctuation (SBF) method, which measures the pixel-to-pixel graininess of unresolved starlight in early-type galaxies, gives H0 = 73.3 ± 2.4 km s^{-1} Mpc^{-1} (Blakeslee et al., 2021). The Tully–Fisher relation between a spiral galaxy's rotation velocity and luminosity, calibrated with Cepheid-hosting galaxies, gives H0 = 75.1 ± 2.3 km s^{-1} Mpc^{-1} (Kourkchi et al., 2020). With the partial exception of TRGB, essentially all late-universe, non-CMB methods return values at or above H0 ≈ 70 km s^{-1} Mpc^{-1}, reinforcing the late-universe side of the tension using techniques with largely independent systematics from the Cepheid ladder.

5.4. Strong-lensing time-delay cosmography

Strong gravitational-lens time-delay cosmography, in which the time delay between multiple images of a lensed quasar or supernova is combined with a model of the foreground lens galaxy's mass distribution, offers a fully independent, one-step geometric route to H0 that requires no distance ladder at all. Assuming a simple power-law mass profile for the lens galaxies, the H0LiCOW collaboration reported H0 = 73.3 ± 1.8 km s^{-1} Mpc^{-1} from six lensed quasars, in agreement with SH0ES and in tension with Planck at the 5.3σ level (Wong et al., 2020). However, the successor TDCOSMO collaboration showed that relaxing the assumed lens mass profile and instead using spatially resolved stellar kinematics to constrain it directly, without an informative prior from external power-law-lens samples, substantially inflates the uncertainty and shifts the central value downward to H0 = 67.4 (+4.1/−3.2) km s^{-1} Mpc^{-1}, consistent with both Planck and SH0ES (Birrer et al., 2020). More recent TDCOSMO analyses using improved spatially resolved kinematics for individual lenses have sought to reduce this degeneracy while retaining physically motivated priors, generally recovering values intermediate between the original H0LiCOW result and the fully free Birrer et al. analysis (TDCOSMO Collaboration, 2023). This body of work demonstrates that the strong-lensing H0 value is more sensitive to assumptions about lens mass-density profiles than originally appreciated, and that its contribution to the overall tension should be weighted accordingly.

5.5. Gravitational-wave standard sirens

Gravitational-wave “standard sirens” offer a further, fully independent channel: the amplitude of a compact-binary merger's gravitational-wave signal gives a direct luminosity distance without any distance-ladder calibration, which, combined with an electromagnetic redshift measurement or a statistical host-galaxy association, yields H0. The landmark binary neutron star merger GW170817 gave H0 ≈ 70 km s^{-1} Mpc^{-1} with an uncertainty broad enough to be consistent with both the Planck and SH0ES values (Abbott et al., 2017). Subsequent events, including statistical “dark siren” analyses without electromagnetic counterparts, have tightened this constraint only modestly; standard sirens currently lack the precision to adjudicate the tension alone but are expected to reach percent-level precision as the LIGO-Virgo-KAGRA network and next-generation detectors accumulate a larger sample of well-localized events.

5.6. Cosmic chronometers

Cosmic chronometers estimate the expansion rate H(z) directly from the differential ages of pairs of massive, passively evolving galaxies at similar redshift, via $H(z) = -(1/(1+z))(dz/dt)$, without assuming any specific cosmological model (Jimenez & Loeb, 2002). Because this method constrains the shape of H(z) rather than its absolute normalization, it does not determine H0 in isolation; H0 must be obtained by extrapolating the reconstructed H(z) to z = 0 or by combining chronometer data with an external calibration such as SN Ia distances. When combined with supernova data in this way, cosmic-chronometer analyses have returned H0 = 67.4 ± 4.75 km s^{-1} Mpc^{-1} (Gomez-Valent & Amendola, 2018), a value with an uncertainty too large to discriminate strongly between the Planck and SH0ES results but broadly consistent with the lower, early-universe value. The chronometer method's principal appeal is its independence from both the cosmic distance ladder and the CMB sound horizon; it will become increasingly competitive as spectroscopic samples of quiescent galaxies grow and as ages are calibrated with improved stellar population synthesis models.

5.7. Quasar and high-redshift cosmography

A distinct approach exploits the nonlinear relation between the ultraviolet and X-ray luminosities of quasars to build a Hubble diagram extending to redshifts far beyond the reach of SNe Ia, z ≈ 5–7 (Risaliti & Lusso, 2019). Because quasars are not true standard candles in the same sense as SNe Ia — the luminosity relation must be calibrated and has intrinsic scatter — this method is generally used less as a direct H0 measurement than as a consistency test of ΛCDM at high redshift. The quasar Hubble diagram, together with related high-redshift compilations combining SNe Ia, quasars, and gamma-ray bursts, has been reported to show a deviation from the flat ΛCDM expansion history extrapolated from low-redshift SN Ia fits at a significance of several sigma, which some authors interpret as independent, redshift-dependent evidence consistent with an evolving dark-energy equation of state of the kind also hinted at by recent DESI BAO analyses (Risaliti & Lusso, 2019). This result remains actively debated, since it depends sensitively on the quasar sample selection and on corrections for intrinsic scatter, but it illustrates that evidence relevant to the Hubble tension is not confined to the traditional CMB-versus-distance-ladder comparison.

Table 1. Selected Determinations of H0

Method	H0 (km s^{-1} Mpc^{-1})	Reference
CMB (Planck, ΛCDM)	67.4 ± 0.5	Planck Collaboration (2020)
BAO + BBN (DESI)	≈ 68	DESI Collaboration (2025)
Cepheid + SNe Ia (SH0ES)	73.04 ± 1.04	Riess et al. (2022)
Cepheid + SNe Ia (JWST)	72.6 ± 2.0	Riess et al. (2024)
TRGB + SNe Ia	69.6 ± 1.9	Freedman et al. (2019, 2020)
Tully–Fisher (Cepheid-cal.)	75.1 ± 2.3	Kourkchi et al. (2020)
Megamasers (geometric)	73.9 ± 3.0	Pesce et al. (2020)
Surface Brightness Fluctuations	73.3 ± 2.4	Blakeslee et al. (2021)
Strong lensing (power-law profile)	73.3 ± 1.8	Wong et al. (2020)
Strong lensing (free mass profile)	67.4 (+4.1/−3.2)	Birrer et al. (2020)
GW standard sirens	≈ 70 (broad)	Abbott et al. (2017)
Cosmic chronometers + SNe Ia	67.4 ± 4.75	Gomez-Valent & Amendola (2018)

Uncertainties are as quoted in the original sources (statistical and, where reported, systematic terms combined). Values in the upper block are early-universe, model-dependent determinations; values in the lower block are late-universe, geometric, or model-independent determinations.

6. Assessing systematics

6.1. The role of JWST

Because the Cepheid-based distance ladder is the most precise late-universe route to H0, an early and widely discussed hypothesis was that the tension reflected an unrecognized systematic in Hubble Space Telescope (HST) Cepheid photometry — for example, contamination from crowded stellar fields or blending with unresolved companions in the crowded fields of the calibrator hosts, an effect to which HST's angular resolution is more susceptible than JWST's. JWST's superior resolution was expected to test this hypothesis directly. Re-observation of the SH0ES Cepheid calibrator hosts with JWST confirmed, rather than overturned, the HST photometry: the JWST magnitudes agree with the earlier HST measurements to within their quoted uncertainties, ruling out crowding and blending as the dominant source of the discrepancy (Riess et al., 2024). Rather than resolving the tension, this result has deepened it, since it removes the most widely discussed mundane explanation and strengthens the case that the discrepancy reflects either an unrecognized systematic elsewhere in the analysis chain or genuine physics beyond ΛCDM.

6.2. SN Ia standardization and the LMC anchor

Beyond Cepheid photometry, two further systematics are routinely scrutinized. First, SN Ia peak luminosities are standardized using empirical relations between light-curve shape, color, and host-galaxy properties; residual, unmodeled dependence of these relations on host-galaxy mass or star-formation history could in principle introduce a redshift-dependent bias between the nearby Cepheid-calibrator hosts and the more distant Hubble-flow sample, although current analyses find no evidence for a bias of the size needed to resolve the tension. Second, the absolute distance to the LMC, one of the primary geometric anchors of the first rung, is now known to better than 1% from a large sample of DEB systems; because this distance propagates directly into H0, continued refinement and independent cross-checks of the LMC distance remain an active priority.

6.3. Lens-modeling systematics

As discussed in Section V.D, the strong-lensing route to H0 is subject to a well-documented mass-sheet degeneracy between the lens galaxy's radial mass profile and the inferred H0; different, individually plausible assumptions about that profile can shift the central value by several km s^{-1} Mpc^{-1}, comparable to the full size of the tension. This is arguably the single largest identified systematic uncertainty among the methods reviewed here, and it argues for caution in treating early published lensing results as fully independent confirmations of the SH0ES value.

7. Quantifying the tension

The commonly quoted “5σ” figure typically refers to a direct comparison of the Planck and SH0ES central values and uncertainties, treating each as an independent Gaussian measurement: the tension in standard deviations is simply the difference in central values divided by the combined uncertainty added in quadrature. More sophisticated statistical treatments account for the fact that a simple Gaussian comparison can be sensitive to the specific pair of experiments chosen and to non-Gaussian tails in either posterior; metrics such as the difference-in-maximum-a-posteriori statistic (Q_DMAP) and Bayesian suspiciousness have been developed to test tension robustly across more complex, non-Gaussian, or correlated datasets.

Because a two-experiment comparison is potentially sensitive to the idiosyncrasies of either analysis, several groups have assembled larger compilations of independent, largely sound-horizon-free H0 measurements — spanning strong lensing, standard sirens, masers, surface-brightness fluctuations, cosmic chronometers, and distance-ladder-free SN Ia spectral modeling — to test whether the tension persists as a general feature of the data rather than a peculiarity of any single pair of experiments. Recent compilations of several dozen such measurements, updated through late 2025, find that the discrepancy between the distance-ladder ensemble and the distance-ladder-independent, sound-horizon-free ensemble persists at a comparable or greater significance than the traditional Planck-versus-SH0ES comparison, and is robust to the exclusion of any single measurement or methodological class, strengthening the case that the tension is a general feature of the data.

8. Theoretical proposals for resolution

With late-time photometric systematics increasingly disfavored by the JWST results, and with the strong-lensing tension shown to be sensitive to lens-modeling assumptions, attention has increasingly shifted to modifications of the standard cosmological model. Proposals broadly fall into five categories.

8.1. Early dark energy and modified pre-recombination physics

Early Dark Energy (EDE) models introduce an additional energy component that is dynamically significant only around the epoch of matter-radiation equality, briefly increasing the early-universe expansion rate and thereby shrinking the sound horizon, rs, imprinted in the CMB and BAO. Because the CMB-inferred H0 depends on rs through the fixed angular scale of the acoustic peaks, a smaller sound horizon raises the inferred H0, potentially reconciling it with the SH0ES value. EDE models can partially relieve the tension but generally require finely tuned parameters, and they are constrained by their effect on the CMB damping tail and on the growth of large-scale structure, which current data do not obviously favor (Poulin, Smith, & Karwal, 2023). Closely related proposals invoke modified recombination physics, primordial magnetic fields, or additional relativistic species (an increase in the effective number of neutrino species, ΔNeff) to alter rs by similar mechanisms; all such proposals face the same basic tension between resolving H0 and preserving the excellent fit of ΛCDM to the detailed shape of the CMB power spectrum.

8.2. Evolving dark energy and late-time modifications

Evolving dark-energy models relax the assumption that dark energy behaves as a strict cosmological constant. Recent DESI BAO results, when combined with CMB and supernova data, show a preference, at low-to-moderate statistical significance, for a dark-energy equation of state that evolves with redshift, often parameterized as w0waCDM, rather than the fixed w = −1 of ΛCDM. Several analyses find that allowing the effective H0 to decline smoothly with the redshift range probed — from values consistent with SH0ES at low redshift toward values consistent with Planck at high redshift — can substantially relieve the tension without introducing new early-universe physics (DESI Collaboration, 2025). Interacting dark-energy models, in which dark energy exchanges energy with dark matter at a rate that depends on redshift, have been proposed on similar grounds and can, in some parameterizations, simultaneously address the S8 tension.

8.3. Modified gravity

A smaller body of work explores departures from general relativity on cosmological scales, such as scalar-tensor or f(R) gravity, which can alter both the growth of structure and the effective expansion history in ways that partially mimic evolving dark energy. These models generally face tight constraints from solar-system tests, the observed near-equality of the speed of gravitational waves and light established by the electromagnetic counterpart to GW170817, and large-scale-structure data, which together limit the viable parameter space for a full resolution of the tension through modified gravity alone.

8.4. Ladder-wide and cross-cutting systematics

A further class of explanation asks whether an as-yet-unidentified systematic affects multiple, nominally independent late-universe methods coherently — for instance, through a shared dependence on the same small set of geometric anchor distances (such as the DEB-based distance to the LMC) or on common assumptions in SN Ia standardization. The general agreement among Cepheid, megamaser, SBF, and Tully–Fisher determinations, which do not share identical systematics, makes a single coherent ladder-wide error a less parsimonious explanation than it was several years ago, but it has not been definitively excluded, and ongoing work — including a JWST program to cross-calibrate the TRGB and SBF distance scales — is specifically designed to test it.

8.5. Other and combined proposals

A range of less mainstream proposals has also been explored, including spatial curvature departing from exact flatness, time-varying fundamental constants, decaying dark matter, and primordial non-Gaussianity affecting the CMB-inferred sound horizon indirectly. Several recent studies also combine elements of the above categories — for example, early dark energy together with a modestly evolving late-time equation of state — finding that hybrid models can relieve the tension further than either ingredient alone, at the cost of additional free parameters and reduced predictivity.

Table 2. Summary of Proposed Theoretical Resolutions

Proposal	Mechanism	Current status
Early Dark Energy (EDE)	Shrinks sound horizon rs before recombination, raising CMB-inferred H0	Partial relief; requires fine-tuning; constrained by CMB damping tail
Evolving dark energy ($w_0 w_a$CDM)	Late-time expansion history departs from w = −1	Mildly favored by DESI BAO; substantial relief possible
Modified gravity (e.g., f(R))	Alters growth of structure and effective H(z)	Tightly constrained by GW170817 and structure growth
Interacting dark energy	Energy exchange between dark energy and dark matter	Can address H0 and S8 tensions jointly; model-dependent
$\Delta N_{\rm eff}$ / extra relativistic species	Increases early expansion rate, shrinks rs	Constrained by CMB and BBN light-element abundances
Ladder-wide systematic	Shared bias across Cepheid, TRGB, SBF, maser, lensing methods	Increasingly disfavored by mutual method agreement
Residual lens mass-profile bias	Power-law priors bias strong-lensing H0 high	Confirmed as a real, partial contributor (Birrer et al., 2020)

9. Discussion

The Hubble tension can usefully be framed as a cosmological trilemma: the reliability of the ΛCDM model, the reliability of early-universe (CMB/BAO) inferences of H0 within that model, and the reliability of late-universe determinations of H0 cannot all be simultaneously correct at face value. The JWST recalibration of the Cepheid distance ladder has substantially weakened the case that late-universe photometric systematics alone are responsible, while the mutual agreement between CMB and BAO+BBN early-universe probes weakens the case for an isolated Planck-specific error. The demonstration that strong-lensing H0 values are sensitive to lens mass-profile assumptions is an important cautionary result, showing that at least one late-universe method's contribution to the tension is more model-dependent than originally reported — a reminder that not every late-universe method is equally probative, and that the strength of the tension should be assessed from the full ensemble in Table I rather than from any single pairwise comparison. The mild, independent hints of evolving dark energy from DESI BAO and from the quasar Hubble diagram add a further, largely independent line of evidence that the late-time expansion history may genuinely depart from ΛCDM, which would naturally link the Hubble tension to changes already being discussed for other reasons. Taken together, the balance of current evidence leaves genuine physics beyond ΛCDM — whether in the pre-recombination era, in the dark-energy sector, or in a subtle systematic common to several distance indicators — as an increasingly plausible explanation, though no single proposal currently commands consensus support.

10. Future prospects

Several forthcoming observational programs are expected to materially sharpen this picture over the next decade. The Vera C. Rubin Observatory's Legacy Survey of Space and Time will discover and monitor large samples of SNe Ia and lensed quasars, improving both the distance-ladder and time-delay-cosmography routes to H0 and providing the statistics needed to average over individual lens-modeling systematics. The Euclid and Nancy Grace Roman Space Telescope missions will extend precise photometric and geometric distance measurements, including TRGB and Cepheid distances, to larger, more homogeneous samples of galaxies over a wider volume than currently accessible from the ground or with HST. A dedicated JWST program aims to establish a firm, TRGB-anchored zero point for the SBF distance scale, directly testing whether ladder-wide systematics can account for part of the tension. DESI's continuing data releases, together with forthcoming spectroscopic surveys, will sharpen constraints on any redshift evolution of the dark-energy equation of state. Finally, an expanding catalogue of gravitational-wave standard sirens from the LIGO-Virgo-KAGRA network and, in the following decade, from the Einstein Telescope and Cosmic Explorer, is expected to eventually deliver an H0 measurement with percent-level precision that is independent of both the CMB and the electromagnetic distance ladder, potentially providing a decisive arbitration of the tension.

11. Limitations of this review

This review is necessarily a synthesis rather than an exhaustive meta-analysis: it does not perform an independent joint statistical combination of the measurements in Table I, and the central values quoted are taken directly from the cited sources without re-analysis. Coverage of the theoretical-proposal literature, which is extremely large and rapidly evolving, is representative rather than complete, and some promising but more speculative proposals have been omitted for brevity. Readers seeking a fully quantitative, continuously updated meta-analysis are directed to the dedicated compilation papers cited in Section VII.

12. Conclusion

A century of increasingly precise measurement — from Hubble's original, order-of-magnitude estimate, through the Sandage–de Vaucouleurs controversy, to the sub-percent-level precision of the modern era — has hardened, rather than dissolved, the discrepancy between early- and late-universe determinations of H0. Early-universe probes anchored in ΛCDM converge tightly on H0 ≈ 67–68 km s^{-1} Mpc^{-1}, while a broad and methodologically diverse ensemble of late-universe measurements clusters around H0 ≈ 70–75 km s^{-1} Mpc^{-1}, and JWST observations have removed the leading purely photometric explanation for the gap. Reconciling the two regimes will likely require either a modification of early-universe physics, such as early dark energy or additional relativistic species; a modification of late-time physics, such as an evolving dark-energy equation of state; or the identification of a subtle systematic shared across several, only partially independent distance indicators. Forthcoming data from the Vera C. Rubin Observatory, Euclid, the Roman Space Telescope, and an expanding gravitational-wave standard-siren catalogue should provide the statistical power needed to distinguish between these possibilities within the next decade.

ACKNOWLEDGEMENTS

The authors declare no conflicts of interest. We are very much thankful to the authors of different publications as many new ideas are abstracted from them. Authors also express gratefulness to their colleagues and family members for their continuous help, inspirations, encouragement, and sacrifices without which this work could not be executed. Finally, the main target of this work will not be achieved unless it is used by research institutions, students, research scholars, and authors in their future works. The authors will remain ever grateful to Dr. Neelu Singh, Director, ICFRE Tropical Forest Research Institute, Jabalpur, Director, XLRI – Xavier School of Management, Jamshedpur & Principal Government Science College, Jabalpur who helped by giving constructive suggestions for this work. The authors are also responsible for any possible errors and shortcomings, if any in the paper, despite the best attempt to make it immaculate.

REFERENCES

[1] Abbott, B. P., Abbott, R., Abbott, T. D., et al. (2017). A gravitational-wave standard siren measurement of the Hubble constant. *Nature*, 551, 85–88.

[2] Birrer, S., Shajib, A. J., Galan, A., et al. (2020). TDCOSMO IV: Hierarchical time-delay cosmography—joint inference of the Hubble constant and galaxy density profiles. *Astronomy & Astrophysics*, 643, A165.

[3] Blakeslee, J. P., Jensen, J. B., Ma, C.-P., Milne, P. A., & Greene, J. E. (2021). The Hubble constant from infrared surface brightness fluctuation distances. *The Astrophysical Journal*, 911, 65.

[4] DESI Collaboration. (2025). DESI DR2 results: Baryon acoustic oscillation measurements and cosmological constraints. *arXiv preprint*.

[5] Di Valentino, E., Mena, O., Pan, S., et al. (2021). In the realm of the Hubble tension—a review of solutions. *Classical and Quantum Gravity*, 38, 153001.

[6] Freedman, W. L., Madore, B. F., Hatt, D., et al. (2019). The Carnegie-Chicago Hubble Program VIII: An independent determination of the Hubble constant based on the tip of the red giant branch. *The Astrophysical Journal*, 882, 34.

[7] Freedman, W. L., Madore, B. F., Hoyt, T., et al. (2020). Calibration of the tip of the red giant branch. *The Astrophysical Journal*, 891, 57.

[8] Freedman, W. L., Madore, B. F., Gibson, B. K., et al. (2001). Final results from the Hubble Space Telescope Key Project to measure the Hubble constant. *The Astrophysical Journal*, 553, 47–72.

[9] Gomez-Valent, A., & Amendola, L. (2018). H0 from cosmic chronometers and Type Ia supernovae, with Gaussian Processes and the novel Weighted Polynomial Regression method. *Journal of Cosmology and Astroparticle Physics*, 2018(04), 051.

[10] Jimenez, R., & Loeb, A. (2002). Constraining cosmological parameters based on relative galaxy ages. *The Astrophysical Journal*, 573, 37–42.

[11] Kourkchi, E., Tully, R. B., Anand, G. S., et al. (2020). Cosmicflows-4: The calibration of optical and infrared Tully–Fisher relations. *The Astrophysical Journal*, 896, 3.

[12] Pesce, D. W., Braatz, J. A., Reid, M. J., et al. (2020). The Megamaser Cosmology Project XIII: Combined Hubble constant constraints. *The Astrophysical Journal Letters*, 891, L1.

[13] Planck Collaboration. (2020). Planck 2018 results VI: Cosmological parameters. *Astronomy & Astrophysics*, 641, A6.

[14] Poulin, V., Smith, T. L., & Karwal, T. (2023). The ups and downs of early dark energy solutions to the Hubble tension: A review of models, hints, and constraints circa 2023. *Physics of the Dark Universe*, 42, 101348.

[15] Riess, A. G., Yuan, W., Macri, L. M., et al. (2022). A comprehensive measurement of the local value of the Hubble constant with 1 km/s/Mpc uncertainty from the Hubble Space Telescope and the SH0ES team. *The Astrophysical Journal Letters*, 934, L7.

[16] Riess, A. G., et al. (2024). JWST observations reinforce distance-ladder measurements of the Hubble constant. *The Astrophysical Journal Letters*.

[17] Risaliti, G., & Lusso, E. (2019). Cosmological constraints from the Hubble diagram of quasars at high redshifts. *Nature Astronomy*, 3, 272–277.

[18] TDCOSMO Collaboration. (2023). TDCOSMO XII: Improved Hubble constant measurement from lensing time delays using spatially resolved stellar kinematics of the lens galaxy. *Astronomy & Astrophysics*, 673, A9.

[19] Verde, L., Treu, T., & Riess, A. G. (2019). Tensions between the early and late Universe. *Nature Astronomy*, 3, 891–895.

[20] Wong, K. C., Suyu, S. H., Chen, G. C.-F., et al. (2020). H0LiCOW XIII: A 2.4% measurement of H0 from lensed quasars— 5.3σ tension between early- and late-Universe probes. *Monthly Notices of the Royal Astronomical Society*, 498, 1420–1439.

GLOBAL JOURNAL
OF SCIENCE FRONTIER RESEARCH - A: PHYSICS & SPACE SCIENCE
Volume 26 | Issue 2 | 2026 Article ID: GJSFR-257716 Language: English

NANO-Technologies and the Physics of Missing Scales

Article Record

Dr. Stanislav V. Ordin § *
ORCID 0000-0003-4189-8948
*Corresponding Author

§ Russian Academy of Sciences, Moscow, Russia (OA)

RECEIVED	ACCEPTED	ONLINE PUBLISHED	PUBLISHED	PEER REVIEW
2026-05-26	2026-06-04	2026-07-07	2026-09-23	Double Blind

Abstract

The development of NANO-technologies follows the path of Feynman's linear approximation of the element minimization method. With this approach, the construction of artificial structures relied on microscopic (quantum) models. However, the output of such NANO-technologies typically didn't exactly correspond to the intended outcome, but to a result that required further understanding and further learning. This is why processors require regular updates of the HIOS. The heuristics of this development path for NANO-technologies are close to zero, so NANO-technologies have become mere empiricism. Achieving UNDERSTANDING what and how to do things, and UNDERSTANDING what NANO-technologies actually do, is possible only by considering two fundamental physical aspects that are essential at the NANO-scale: 1. Local Thermodynamic Effects, determined by Prigogine's Flow Thermodynamics, must be taken into account. 2. It is necessary to consider the experience of "Living Nanotechnology," which relies not on "dead" Boltzmann statistics, but on statistics with information accumulation and on the fractal construction of Life from below, from fullerenes to minimal fractals and beyond. And both of these aspects must be considered both at the design stage of the required device's functionality and in the formation of the NANO-structure itself.

dimensional linear approximation | fractality | limits of "dead" NANO-technology | NANO-anomalies | Resonance states

AI USE STATEMENT
No generative AI was used for analysis or results.

FUNDING
No external funding was declared for this work.

CONFLICT OF INTEREST
The authors declare no conflict of interest.

DATA AVAILABILITY
Not applicable for this article.

ETHICS
No ethics committee approval was required for this article type.

CONSENT
Not applicable for this article.

TRIAL REG.
Not applicable.

Crossref DOI: 10.34257/GJSFRA257716

How to Cite: Ordin (2026). NANO-Technologies and the Physics of Missing Scales. Global Journal of Science Frontier Research, 26(2), 29-34. DOI: 10.34257/GJSFRA257716

AR Experience Web Page DOI

Print ISSN 0975-5896
9 770975 589008

Online ISSN 2249-4626
9 772249 462017

Under the strict compliance and defined process of
OARS (USA)

ARCHIVAL RECORD

GJSFR · Vol 26 · Issue 2 · 2026

Article ID GJSFR-257716 · DOI 10.34257/GJSFRA257716

Print ISSN 0975-5896 · Online ISSN 2249-4626

Global Journal of Science Frontier Research - Section A
GJSFR Volume 26 Issue 2

NANO-Technologies and the Physics of Missing Scales

Dr. Stanislav V. Ordin [§, *]

Affiliations
§ Russian Academy of Sciences, Moscow, Russia (OA)

Abstract

The development of NANO-technologies follows the path of Feynman's linear approximation of the element minimization method. With this approach, the construction of artificial structures relied on microscopic (quantum) models. However, the output of such NANO-technologies typically didn't exactly correspond to the intended outcome, but to a result that required further understanding and further learning. This is why processors require regular updates of the HIOS. The heuristics of this development path for NANO-technologies are close to zero, so NANO-technologies have become mere empiricism. Achieving UNDERSTANDING what and how to do things, and UNDERSTANDING what NANO-technologies actually do, is possible only by considering two fundamental physical aspects that are essential at the NANO-scale: 1. Local Thermodynamic Effects, determined by Prigogine's Flow Thermodynamics, must be taken into account. 2. It is necessary to consider the experience of "Living Nanotechnology," which relies not on "dead" Boltzmann statistics, but on statistics with information accumulation and on the fractal construction of Life from below, from fullerenes to minimal fractals and beyond. And both of these aspects must be considered both at the design stage of the required device's functionality and in the formation of the NANO-structure itself.

Keywords: *dimensional linear approximation, fractality, limits of "dead" NANO-technology, NANO-anomalies, Resonance states*

*** Corresponding Author**
Dr. Stanislav V. Ordin

DOI
10.34257/GJSFRA257716

1. Introduction

Both in Physics itself and in the common consciousness, phenomenological misconceptions have led to the triumph of the illusion that the Quantum-Mechanical Description provides the most complete picture of the Phenomenon and the gaping Peaks of Science. But the modern Quantum-Mechanical Description itself ignored Albert Einstein's wise remark: "Some (CORRECT) equations of Classical Mechanics can be rewritten in operator form." Furthermore, the profoundly ironic warning of the founder of Quantization, Max Planck, was also ignored: "Apparently, I am not literate enough to understand what has been calculated on the basis of the Quantum Concepts I introduced." Thus, modern Quantum Theory has given rise to a jumble of formulas of the "most rigorous science" - Quantum Electrodynamics, with the "discoveries" of the useless God Particles and Black Holes [1]. In reality, the Schrödinger equation only adequately describes the s-orbitals of hydrogen-like atoms [2]. Nevertheless, this primitive description was also used in Chemistry [3], and it became virtually the primary tool underlying the Quantum Theory of Solid State Physics [4]. At the same time, unproven, arbitrary individuals assumed that these Quantum-Mechanical Models could be directly extended to NANO-effects.

The enthusiasm with which Quantum Mechanics began to be used to explain effects in Solid States somehow obscured the question of the fundamental POSSIBILITY of observing Quantum Phenomena in Macroscopic Dimensions. And new effects discovered on the NANO-scale, believing them to be a linear approximation between the Quantum and Macroscopic, were also taken for granted as OBSERVABLE. With the exception of Thermoelectric Effects, which, based on Boltzmann Thermodynamics, were considered UNOBSERVABLE in principle [5]. Therefore, a TABOO was imposed on the very EXISTENCE of NANO-Thermo-EMF. And their EXISTENCE, as well as their MEASURABILITY, follow from Ilya Prigogine's Local Entropy Production, discovered by him in Flow Thermodynamics [6]. The registration of NANO-Thermo-EMF demonstrated that between Quantum and Macroscopic Effects, there exist previously unaccounted for ballistic Thermionic Effects [7], which are not inferior in magnitude to Photoelectric Effects (Fig. 1).

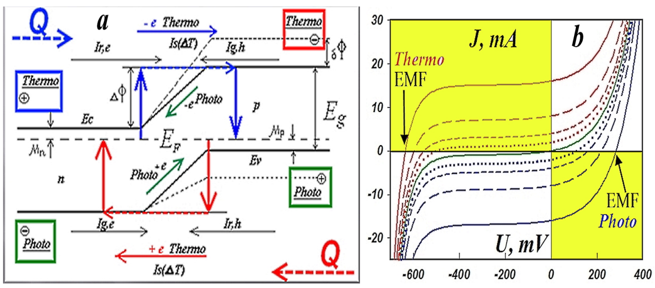

Figure 1. Schematic diagram of the formation of both photo-EMF and local thermal-EMF (left) in the p-n junction, leading to an antiphase shift in the current-voltage characteristics (right).

These recorded powerful thermionic effects directly indicate the need to transform the physics of semiconductor devices at the nanoscale [8], which has not yet been taken into account even in processor design.

However, they indirectly indicate the need to consider local entropy production in manufacturing, in nanotechnologies themselves.

After all, modern nanotechnologies are essentially simply attempting to implement Feynman's linear approximation: make devices smaller, and then make these devices even smaller (Fig. 2).

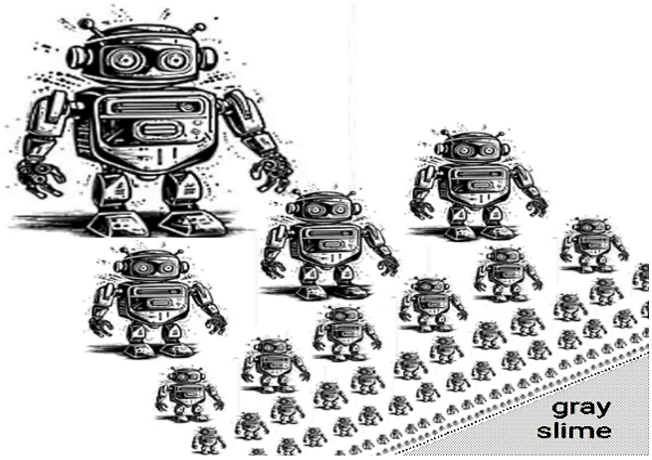

Figure 2. "Dead" NANO-technology, based on models using destructive measurement techniques, from the macro level down to the atoms, according to Feynman's linear approximation.

And 3D printing of materials—without taking into account chemical bonds, allowed electron orbitals, and resonant states of the material, in general, without considering the NANO-structuring of the created materials—is largely a waste of time. To build NANO-technology, it is necessary to understand that it is described by the boundary between Classical and Quantum Physics [9]. Moreover, new properties of the created NANO-objects must be sought not in mystical changes in Fundamental Characteristics, which contradicts the adiabatic decomposition of Energy, but in NANO-structuring, which leads to gigantic effects. And there's already a significant experimental and theoretical foundation for this, based on research into midi effects in natural and artificial superstructures, which simply need to be generalized and understood. However, attempts continue to be made to build devices with ever-smaller elements, simply following Feynman's linear approximation. The developers themselves can't always understand what they've done. This is how, for example, computer processors are made. But then, through programming, they're effectively corrected. Moreover, after the first release of a "working" processor, an updated BIOS is released almost every month, correcting newly discovered errors.

Yet, Feynman's "cellular automaton," implemented by dead NANO-technologies, is, in principle, an alternative to the von Neumann-Conway cellular automaton [10, 11], confirmed at least by the fact that this model lifted the thermodynamic BAN on the existence of LIFE itself.

But, as was understood, the work of a living cellular automaton results in an increase in the object not at all like the growth of an ideal crystal - linearly, but fractally (Fig. 3).

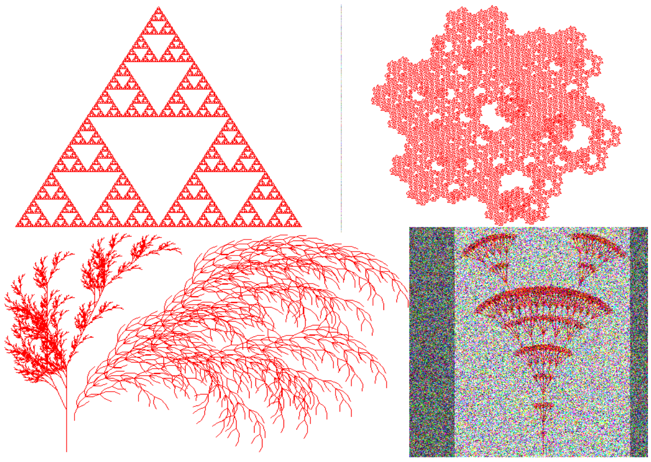

Figure 3. Fractal growth of an object and the superposition of the elementary "Flower" Fractal on Chaos.

So, the dynamics of shrinking a NANO-object using "dead" technology will also collide with the fact that Nature strives to create its OWN (resonant, quantum, according to Planck) structures on the NANO-scale. After all, as living "NANO-technology" clearly demonstrates, simply shrinking a tree will not produce its branch or root, and vice versa – a tree is not simply an enlarged cell (Fig. 4).

Figure 4. Bipolar fractal development of a tree's crown and roots.

Living NANO-technology begins to build organic matter from the smallest fullerenes, capable of accumulating information about prehistory within their structure. And by transforming the "dead" Boltzmann statistics into "living" statistics with information accumulation, it sets the stage for fractal development. In living nature, the Creator determines whichever fractal first "came to hand"—those trees, vegetables, and organs will grow (Fig. 5).

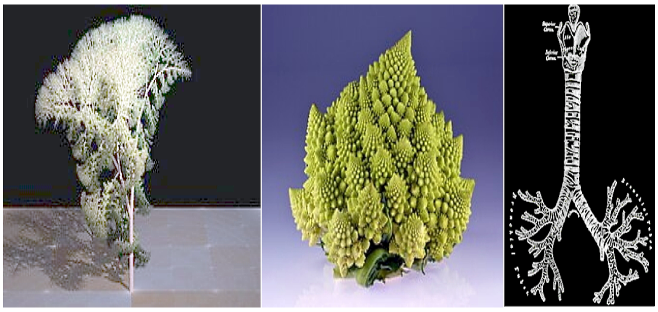

Figure 5. Fractal tree (left), kale (center), trachea (right).

Thus, while ”dead” NANO-technology, according to Feynman, ultimately leads only to the destruction of life, living NANO-technology emphasizes that the INDIGENOUS structuring of the material at different scales must be taken into account. Furthermore, it must be taken into account that the artificial structures being created are in a metastable state, which, as is well known from ”dead” technologies, leads to structural transformations at certain temperatures. This is most clearly demonstrated by incommensurate crystals. In particular, the quasicrystal of Higher Manganese Silicide (HMS), which exists in a metastable incommensurate state over a very wide temperature range: 2–100 K [12]. This allows us to trace the dependence of the lattice of concentration solitons arising in it on heat treatment: rapid cooling (Fig. 6a) and slow drawing of the sample through a temperature gradient at the boundary of the solid-phase transition (Fig. 6b).

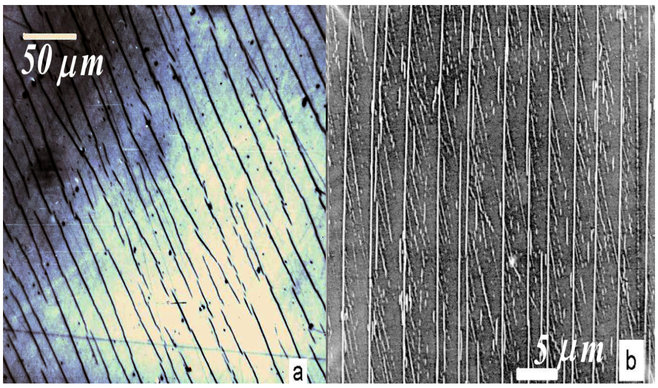

Figure 6. Optical photographs of a plane parallel to the disproportion axis C of an incommensurate HMS quasicrystal: a) during the stochastic formation of concentration precipitates approximately 3 µm thick during rapid cooling; b) during the formation of a regular network of concentration solitons perpendicular to the disproportion axis C, 300 Å thick, during slow cooling.

The rapidly cooled HMS samples (Fig. 6, left) had a blurring of the Bragg reflections from the C axis that was almost two orders of magnitude greater than that of highly ordered HMS quasicrystals, which, in the region between concentration solitons, were close to the commensurate Mn_4Si_7 superstructure (Fig. 6, right). However, judging by the moiré pattern between the concentration solitons (Fig. 7), the disproportion is also preserved in the highly ordered HMS quasicrystal.

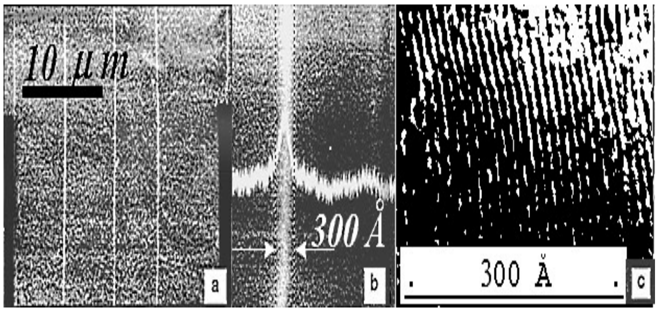

Figure 7. Scanning electron microscopy of the plane of a highly ordered HMS quasicrystal parallel to the C axis: a - overall picture, b - near a concentration soliton, c - transmission electron microscopy of the HMS quasicrystal between concentration solitons.

So, for the reasons noted, using nanotechnology without understanding the fundamental laws of the nanoscale is not only ineffective but also extremely dangerous. In the meantime, they employ a purely empirical approach, driven by bluff companies like the graphene company, which leads to a waste of effort and resources. Meanwhile,

The emergence of gigantic effects at boundary scales is clearly manifested at the nanoscale in the IR reflectance spectra of an incommensurate HMS quasicrystal (Fig. 8).

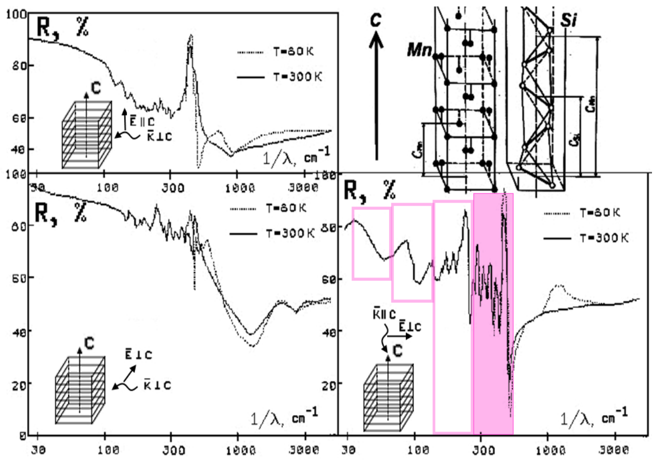

Figure 8. Crystal lattice of an incommensurate HMS quasicrystal (top, right) and the Giant Spatial Dispersion in its polarized IR reflection (the insets schematically indicate the direction of IR radiation propagation and its polarization relative to the concentration solitons in the HMS) [12].

As can be seen from Fig. 8, when IR radiation is polarized parallel to the incommensurate axis C (left, top), only one characteristic powerful lattice oscillator is excited, determined by a local dipole. Therefore, along the incommensurate axis of the HMS quasicrystal, multiple folding of the Brillouin zone, as in commensurate superstructures, does not occur, and the quasicrystal behaves like an amorphous body. While the polarization of IR radiation in the plane perpendicular to the incommensurability axis C (Fig. 8, bottom), in the plane, as shown by Bragg reflections, with a clearly defined period of translation of the unit cell of the crystal lattice (Fig. 8, top, right), we have a set of oscillators corresponding to the unit crystal lattice (highlighted in solid pink). However, judging by the presence of long-wavelength oscillators at fractional frequencies relative to the high-frequency set of oscillators (highlighted in pink frames), they arise due to the parametric interaction of the high-frequency set of oscillators with oscillations along the incommensurability axis C. Moreover, the contribution of increased conductivity along the layers of concentration solitons is significant only if the light propagates along these layers (Fig. 8, bottom, left). Whereas, when light propagates along the C-axis, because the thickness of the concentration solitons is smaller than the skin layer thickness, no plasma reflection is formed (Fig. 8, bottom, right).

It is also necessary to consider the influence of the size of nanostructure elements on the energy band structure of the materials used. This influence affects not only the change in the position of the energy bands of macroscopic materials, but also the change in barriers at the boundaries of dissimilar materials due to the Schottky effect (Fig. 9).

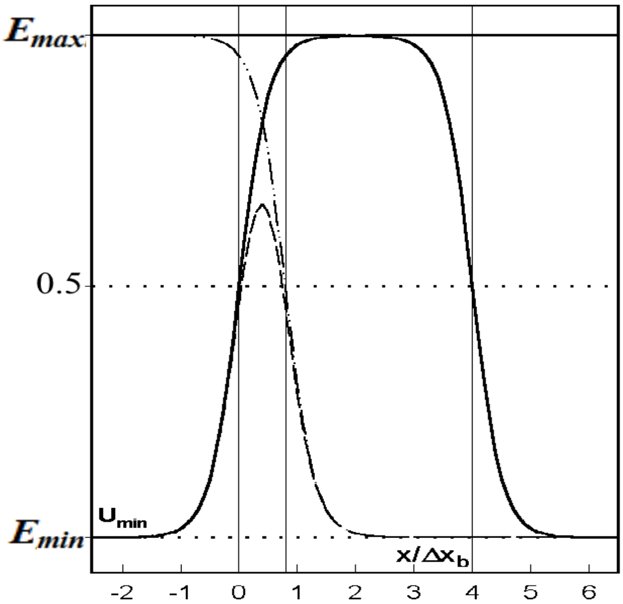

Figure 9. Reduction in the height of the potential barrier between materials when the thickness of the element decreases below the Debye length.

So, even on the path of element reduction using "dead" NANO-technology (moving from above), incommensurate quasicrystals arising due to solid-phase transitions in the crystal lattice in a metastable state demonstrate that the Feynman linear approximation is not observed. Indeed, all created artificial NANO-structures are in a metastable state. The same violation of the linear approximation is demonstrated by living "NANO-technology" on the path from below, from fullerenes, through the fractals shown above, and to microorganisms.

The General Principles of miniaturization of artificial, dead technologies [13] and natural, living technologies found by Nature show that Nature has long mastered the NANO-scale, and with much higher accuracy than we can consciously do (Fig. 10).

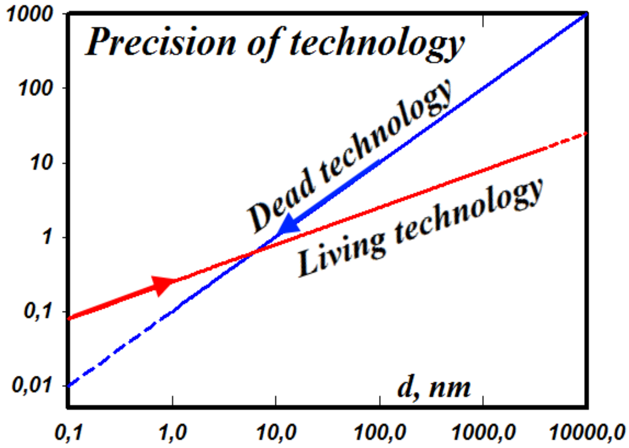

Figure 10. Diagram of the polar development of dead and living technologies.

At the same time, as shown by the dotted lines in Fig. 9, the minimum limit of controllable sizes achieved by "dead" NANO-technology is significantly higher than that of living "NANO-technology." However, the upper limit of achieved sizes is the opposite: we have learned to build ships larger than a whale and skyscrapers and bridges larger than an elephant.

Here is a "simplest" example of the reproduction of a living cell and its development into the most complex neuron in our brains (Fig. 11).

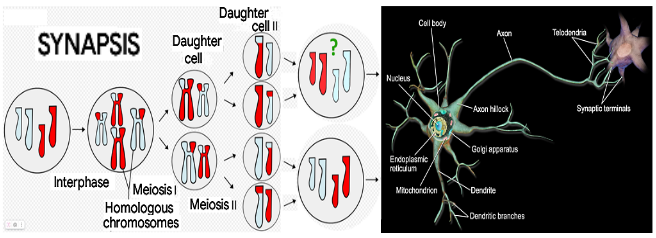

Figure 11. Living "nano-technology" embedded in cell reproduction through fusion and division (on the left is Synapsis—chromosome conjugation, the pairwise temporary convergence of homologous chromosomes, during which an exchange of homologous regions can occur between them).

From the formed cells, organs, nerve fibers, and the entire organism are formed (as demonstrated previously—fractally). But even in the area of UNDERSTANDING living "NANO-technologies," there is still no ELEMENTARY, consistent description. Thus, Fig. 11 on the left will not give us the neuron depicted on the right, since its recurrent invariance is violated—it would be too wasteful for "wise Nature" to create an unnecessary anti-cell (marked with a question mark). Of course, this is important not only for constructing physical models, but also for developing medical models and, ultimately, for proper treatment.

So, for now, we have both a loose description of living "NANO-technologies," built on the basis of life-destroying physical methods, and a primitive description of "dead" NANO-technologies, based on crude quantum-mechanical models. Moreover, as has been shown, a fundamentally important aspect of the description of both living and dead Nature has been omitted.

Thus, without actually mastering even the micron scale, by simply reducing the size of components, we have built call centers out of processors that will not only soon consume the majority of the electrical energy produced by humanity, but also define TASKS that are supposedly relevant for all of humanity. And modern consumer society, built on bureaucratic principles, has no way to counter this. And not only does it counter this, but, on the contrary, it is engaged in a race to actively utilize Artificial Intelligence based on the practically used dead NANO-technology.

Thus, NANO-technologies have reached the social level. But the ELEMENTS of Electronics, created without reliance on Fundamental Science, consume billions of times more energy than the receptors and nervous system of a living organism. So, while these unintelligent NANO-technologies are devouring planet Earth, they leave no room for LIFE on it! And Artificial Intelligence only facilitates this.

In fact, what is currently happening in the world is a vortex, sucking all of humanity into complete UNCERTAINTY, which is now fashionably called a Singularity. Although this name is meaningless, as it denotes the same uncertainty, but for the mathematical function being used—i.e., the wrong function is being used to describe the observed process.

REFERENCES

[1] S. V. Ordin, Foundations of Quantization, Taylor & Francis Group, New York, 2024, 494 pp. https://doi.org/10.1201/9781003570615

[2] Ordin SV (2026). Tetrahedral Characterization of Electronic Materials. Global J Mater Sci Eng 8 (1): 191 DOI: https://doi.org/10.36266/GJMSE/191

[3] Ordin S.V., "Frontier Chemistry Aspects", Global Journal of Science Frontier Research: B- Chemistry (GJSFR-B), Volume 20 Issue 2 Version 1.0, pp. 1-11, Year 2020. ISSN Online: 2249-4626, ISSN Print : 0975-5896, DOI : 10.17406/GJSFR, https://globaljournals.org/GJSFR_Volume20/1-Frontier-Chemistry-Aspects.pdf

[4] J.M. Ziman, Principles of the theory of solids, Cambridge, University Press, 1972, 278 pp.

[5] S.V. Ordin, «"Anomalies in Thermoelectricity and Reality are Local Thermo-EMFs», Global Journal of Science Frontier Research - Physics & Space Science, GJSFR-A, Volume 18 Issue 2 Version 1.0, p. 59-64, 2018 https://globaljournals.org/GJSFR_Volume18/6-Anomalies-in-Thermoelectricity.pdf

[6] Ordin S.V., Refinement and Supplement of Phenomenology of Thermoelectricity, American Journal of Modern Physics, Volume 6, Issue 5, September 2017, Page: 96-107, https://doi.org/10.11648/j.ajmp.20170605.14

[7] Stanislav Ordin, «Ballistic thermoelectricity», Advanced Energy Conversion Materials, ISSN: 2717-5804 (Print) 2717-5812 (Online), Letter, Volume 4 Issue 2 | 2023 | 139-146, https://ojs.wiserpub.com/index.php/AECM/article/view/3336

[8] Stanislav Ordin, «Transformation of Electronics Taking Local Effects into Account», Journal of Material Sciences & Energy Advances, Scientific Knowledge Group (SKG) Publishers, Received: January 26, 2026; Accepted: February 03, 2026; Published: February 10, 2026, J Mat Sci Ener Adva, 2026; Vol 1; Issue 1, pp. 1-4, https://skgpublishers.com/journal-of-material-sciences-energy-advances-jmsea-article-inpress

[9] Stanislav Ordin, « Physical Bases of Nano», Crimson Publishers (Wings to the Research), Research & Development in Material Science (RDMS RDMS.001029. 22(1).2025, Volume 22 - Issue 1, 2663-2668: Res Dev Material Sci. 22(1). RDMS. 001029. 2025. DOI: 10.31031/RDMS.2025.22.001029, https://doi.org/10.31031/RDMS.2025.22.001029

[10] J. H. Conway. Regular Algebra and Finite Machines. — London : Chapman and Hall, 1971. — ISBN 9780412106200. J. H. Conway. Regular Algebra and Finite Machines. — New York : Dover, 2012. — ISBN 9780486310589. — ISBN 9780486485836.

[11] J. H. Conway. On Numbers and Games. — New York : Academic Press, 1976. — ISBN 9780121863500. J. H. Conway. On Numbers and Games. — 2nd ed. — Wellesley, Massachusetts : A K Peters, 2001. — ISBN 9781568811277.

[12] S.V. Ordin, "Giant spatial dispersion in the region of plasmon-phonon interaction in one-dimensional- incommensurate crystal the higher silicide of manganese (HSM)", in Book: Optical Lattices: Structures, Atoms and Solitons, Editors: Benjamin J. Fuentes, Nova Sc. Publ. Inc., 2011, pp. 101-130. ISBN: 978-1-61324-937-6, Series: Lasers and Electro-Optics Research and Technology, Physics Research and Technology, Binding: Hardcover, Pages: 241.pp, Status: AV

[13] Ordin SV (2026). Principles of Characterization of Nanomaterials. Global J Mater Sci Eng 8 (1): 185 DOI: https://doi.org/10.36266/GJMSE/185

[14] S.V. Ordin, "Experimental and Theoretical Expansion of the Phenomenology of Thermoelectricity", Global Journal of Science Frontier Research- Physics & Space Science (GJSFR-A) Volume 18, Issue 1, p. 1-8, 2018. https://globaljournals.org/GJSFR_Volume18/E-Journal_GJSFR_(A)_Vol_18_Issue_1.pdf

[15] S.V. Ordin, «"Anomalies in Thermoelectricity and Reality are Local Thermo-EMFs», Global Journal of Science Frontier Research - Physics & Space Science, GJSFR-A, Volume 18 Issue 2 Version 1.0, p. 59-64, 2018 https://globaljournals.org/GJSFR_Volume18/6-Anomalies-in-Thermoelectricity.pdf

[16] Ordin S.V., "C & BN-Foundation for Atomic-Crystalline Orbitals", Global Journal of Science Frontier Research - Physics & Space Science, GJSFR-A, Volume 18, Issue 5, Version 1.0, pp. 17-47, https://globaljournals.org/GJSFR_Volume18/3-C-&-BN-Foundation.pdf, https://globaljournals.org/GJSFR_Volume18/E-Journal_GJSFR_(A)_Vol_18_Issue_5.pdf

[17] Ordin S.V., «Newton's Coulomb Laws», Global Journal of Science Frontier Research- Physics & Space Science (GJSFR-A), 2019 Vol.19 Issue 1 Version 1.0, p. 145-155. https://globaljournals.org/GJSFR_Volume19/E,Journal_GJSFR_(A)_Vol_19_Issue_1.pdf

[18] Ordin, S.V., «CHAOS – IMAGINARY OSTENSIBILITY – ORTHOGONALITY», Global Journal of Science Frontier Research - Physics & Space Science, GJSFR-A Volume 19 Issue 3 Version 1.0 p.49-58, https://globaljournals.org/GJSFR_Volume19/3-Chaos-Imaginary-Ostensibility.pdf

[19] Ordin, S.V., «Parametrically excited Anharmonic Oscillator», Global Journal of Science Frontier Research - Physics & Space Science, GJSFR-A Volume 19 Issue 3 Version 1.0 p.133-144,

https://globaljournals.org/GJSFR_Volume19/7-Parametrically-Excited.pdf

[20] Ordin, S.V., «The Schottky Effect and Cosmos», Global Journal of Science Frontier Research- Physics & Space Science (GJSFR-A), Volume 19 Issue 4 Version 1.0, p.39-50, https://journalofscience.org/index.php/GJSFR/article/view/2480, https://journalofscience.org/index.php/GJSFR/issue/view/399, https://globaljournals.org/GJSFR_Volume19/E-Journal_GJSFR_(A)_Vol_19_Issue_4.pdf

[21] Ordin S.V., "Frontier Chemistry Aspects", Global Journal of Science Frontier Research: B- Chemistry (GJSFR-B), Volume 20 Issue 2 Version 1.0, pp. 1-11, Year 2020. ISSN Online: 2249-4626, ISSN Print : 0975-5896, DOI : 10.17406/GJSFR, https://globaljournals.org/GJSFR_Volume20/1-Frontier-Chemistry-Aspects.pdf

[22] Stanislav Ordin, "Gaps and Errors of the Schrödinger Equation", Global Journal of Science Frontier Research, GJSFR Volume 22 Issue 3 Version 1.0, p 1-5. https://globaljournals.org/GJSFR_Volume22/3-Gaps-and-Errors.pdf

[23] Stanislav Ordin, "Quantization ESSENCE." Global Journal of Science Frontier Research: A, Physics and Space Science, Volume 23 Issue 5 Version 1.0 Year 2023, p.21-29, Type: Double Blind Peer Reviewed International Research Journal Publisher: Global Journals, Online ISSN: 2249-4626 & Print ISSN: 0975-5896, DOI : 10.17406/GJSFR, https://doi.org/10.34257/GJSFRAVOL23IS5PG21, https://globaljournals.org/GJSFR_Volume23/2-Quantization-Essence.pdf, https://globaljournals.org/GJSFR_Volume23/E-ournal_GJSFR_(A)_Vol_23_Issue_5.pdf

[24] Stanislav Ordin, "Math-Phys-Chem-Virology." Global Journal of Science Frontier Research: A, Physics and Space Science, Volume 23 Issue 5 Version 1.0 Year 2023. Type: Double Blind Peer Reviewed International Research Journal, Publisher: Global Journals, p. 41-44, Online ISSN: 2249-4626 & Print ISSN: 0975-5896, DOI : 10.17406/GJSFR, https://doi.org/10.34257/GJSFRAVOL23IS5PG41, https://globaljournals.org/GJSFR_Volume23/4-Math-Phys-Chem-Virology.pdf, https://globaljournals.org/GJSFR_Volume23/E-ournal_GJSFR_(A)_Vol_23_Issue_5.pdf

[25] Stanislav Ordin, "Non-Schroedinger Orbitals", Global Journal of Science Frontier Research: A, Physics and Space Science Volume 24 Issue 2 Version 1.0 Year 2024, p. 39-48. Publisher: Global Journals. Online ISSN: 2249-4626 & Print ISSN: 0975-5896. DOI : 10.17406/GJSFR, GJSFR-A Classification: LCC: QC174.17.S3 https://globaljournals.org/latest-ejournals-in-gjsfr https://doi.org/10.17406/gjsfr

[26] Stanislav Ordin, "Exceptionality Exclusion: Bridging Quantization and Relativity", Global Journal of Science Frontier Research: A, Physics and Space Science Volume 24 Issue 2 Version 1.0 Year 2024, p. 5-65. Publisher: Global Journals. Online ISSN: 2249-4626 & Print ISSN: 0975-5896. DOI : 10.17406/GJSFR, GJSFR-A Classification: LCC: QC174.12 https://globaljournals.org/GJSFR_Volume24/5-EXCEPTIONALITY-EXCLUSION.pdf

[27] Stanislav Ordin, «Anti-Graphene», Global Journal of Science Frontier Research: A, Physics and Space Science, Volume 25 Issue 6 Version 1.0, 2026, pp. 19-25, https://journalofscience.org/index.php/GJSFR/article/view/103041, https://journalofscience.org/index.php/GJSFR/article/view/103040/27146

[28] Stanislav Ordin, «Anti-Graphene», Global Journal of Science Frontier Research: A, Physics and Space Science, Volume 25 Issue 6 Version 1.0, 2026, pp. 19-25, https://journalofscience.org/index.php/GJSFR/article/view/103041, https://journalofscience.org/index.php/GJSFR/article/view/103040/27146

[29] Stanislav V. Ordin, «The Dialectics of Science and Magnetism», Journal: Global Journal of Science Frontier Research - A: Physics & Space Science (GJSFR) Volume: GJSFR-A Volume 26 | Issue: GJSFR Volume 26 Issue A1 | Version: 1.0, pp. 8-14 eLaunch Date and Time: April 8, 2026, · Article ID GJSFR-254694 · DOI https://doi.org/10.34257/GJSFRA254694, Print ISSN 0975-5896 · Online ISSN 2249-4626 https://globaljournals.org/?post_type=scholarly_article&p=254694, https://doc.globaljournals.org/4ydjkq_254694/article/dialectics-of-science-and-magnetism.pdf?v=f2fc64112f65, https://doc.globaljournals.org/GJSFR_Volume_26/EJournal_gjsfr_volume_26_issue_a1.pdf?v=320cb0d1e8ec

GLOBAL JOURNAL
OF SCIENCE FRONTIER RESEARCH - A: PHYSICS & SPACE SCIENCE
Ahead of Print | 2026
Article ID: GJSFR-259483
Language: English

TEP–UCF Unified Cosmology: Coherence-Driven Expansion and the Ξ Invariant

Online First

Kunal Kishor Verma *
*Corresponding Author

Jarid Shaub

RECEIVED	ACCEPTED	ONLINE PUBLISHED	PUBLISHED	PEER REVIEW
2026-07-25	2026-08-03	2026-09-12	2026-09-23	Double Blind

Abstract

The Timeless Energy Principle -- Unified Coherence Framework (TEP--UCF) introduces a deterministic phenomenological model in which geometric expansion, coherence decay and effective energy are coupled through the conserved scaling invariant $\Xi = E/(g\phi)$.
This invariant emerges as a consequence of the phenomenological coupling $\gamma = \alpha - \beta$ and the unity condition $g\phi \approx 1$.
We demonstrate internal consistency through
(i) Exact exponential solutions,
(ii) Numerical integration with sub-0.1% drift,
(iii) Lyapunov stability analysis, and
(iv) Planck-unit normalization. A coherence-feedback modification to the Friedmann equation is proposed phenomenologically as $H^2 = (8\pi G/3)\rho[1 + \dot{\phi}/(4H\phi)]$.
Synthetic Pantheon+-like distance-modulus data generated within the TEP--UCF framework yield a reduced $\chi^2/\mathrm{d.o.f.} \approx 1.02$ under the adopted mock-data assumptions.
The framework offers a fine-tuning-free alternative mechanism for late-time acceleration driven by informational coherence dynamics.
The framework provides a phenomenological, fine-tuning-free alternative for modeling late-time cosmic acceleration through informational coherence dynamics. Its observational viability will ultimately depend on successful confrontation with official Pantheon+, DESI BAO, and Planck datasets.

$$\Xi = E/(g\phi) = \text{constant}$$

Timeless Energy Principle | Unified Coherence Framework | Ξ invariant | coherence-driven expansion | dark energy alternative | informational gravity | modified Friedmann equation

AI USE STATEMENT
No generative AI was used for analysis or results.

FUNDING
No external funding was declared for this work.

CONFLICT OF INTEREST
The authors declare no conflict of interest.

DATA AVAILABILITY
Not applicable for this article.

ETHICS
No ethics committee approval was required for this article type.

CONSENT
Not applicable for this article.

TRIAL REG.
Not applicable.

Crossref DOI: 10.34257/GJSFRA259483

How to Cite: VERMA et al. (2026). TEP–UCF Unified Cosmology: Coherence-Driven Expansion and the Ξ Invariant. Global Journal of Science Frontier Research. Ahead of Print. DOI: 10.34257/GJSFRA259483

AR Experience Web Page DOI
Print ISSN 0975-5896
Online ISSN 2249-4626

ARCHIVAL RECORD

GJSFR · Vol 26 · Issue 2 · 2026

Article ID GJSFR-259483 · DOI 10.34257/GJSFRA259483

Print ISSN 0975-5896 · Online ISSN 2249-4626

Global Journal of Science Frontier Research - Section A
GJSFR Volume 26 Issue 2

TEP–UCF Unified Cosmology: Coherence-Driven Expansion and the Ξ Invariant

Kunal Kishor Verma* and Jarid Shaub

Abstract

The Timeless Energy Principle -- Unified Coherence Framework (TEP--UCF) introduces a deterministic phenomenological model in which geometric expansion, coherence decay and effective energy are coupled through the conserved scaling invariant $\Xi = E/(g\phi)$.

This invariant emerges as a consequence of the phenomenological coupling $\gamma = \alpha - \beta$ and the unity condition $g\phi \approx 1$.

We demonstrate internal consistency through
(i) Exact exponential solutions,
(ii) Numerical integration with sub-0.1% drift,
(iii) Lyapunov stability analysis, and
(iv) Planck-unit normalization. A coherence-feedback modification to the Friedmann equation is proposed phenomenologically as $H^2 = (8\pi G/3)\rho[1 + \dot{\phi}/(4H\phi)]$.

Synthetic Pantheon+-like distance-modulus data generated within the TEP--UCF framework yield a reduced χ^2/d.o.f. ≈ 1.02 under the adopted mock-data assumptions.

The framework offers a fine-tuning-free alternative mechanism for late-time acceleration driven by informational coherence dynamics.

The framework provides a phenomenological, fine-tuning-free alternative for modeling late-time cosmic acceleration through informational coherence dynamics. Its observational viability will ultimately depend on successful confrontation with official Pantheon+, DESI BAO, and Planck datasets.

$$\Xi = E/(g\phi) = \text{constant}$$

Keywords: *coherence-driven expansion, dark energy alternative, emergent cosmology, informational gravity, modified Friedmann equation, Timeless Energy Principle, Unified Coherence Framework, Ξ invariant*

* **Corresponding Author**
Kunal Kishor Verma

DOI
10.34257/GJSFRA259483

1. Framework Overview

The TEP–UCF framework is motivated by a simple but profound observation: the standard cosmological model (ΛCDM) reproduces observational data with high precision but requires two unexplained free parameters — dark matter density Ω_{DM} and the cosmological constant Λ.

The fine-tuning problem (why $\Lambda \approx 10^{-122}$ in Planck units?) remains unsolved [11, 12].

The TEP–UCF approach replaces these phenomenological parameters with a single physical principle: space-time is an informationally active medium in which geometric expansion and coherence decay are coupled by a conservation law.

The universe is self-regulating — it enforces the condition $g\phi \approx 1$ at all times through a feedback symmetry between spatial geometry and coherence density.

1.1. The Three Fields

The TEP–UCF model is governed by three coupled scalar fields:

Table 1. The fields and parameters of the TEP–UCF framework.

Field	Symbol	Physical Meaning	Scaling Behavior
Geometric scale	$g(\eta)$	Dimensionless expansion driver; proportional to cosmic scale factor	$g \propto e^{\alpha\eta}$ (expanding)
Coherence density	$\phi(\eta)$	Inverse-entropy representation; encodes informational order of the space-time medium	$\phi \propto e^{-\beta\eta}$ (decaying)
Effective energy	$E(\eta)$	Thermodynamic output power of the coherence-geometry system	$E \propto e^{\gamma\eta}$ (amplifying)
Coupling parameters	α, β, γ	Geometric growth, coherence decay, and effective-energy evolution rates. Constraint: $\gamma = \alpha - \beta$. Unity-condition case: $\alpha = \beta$ and $\gamma = 0$.	Set by physical normalization
Normalized-time	η	Dimensionless time parameter; maps to cosmic time via $\eta = H_0 t$	$\eta \in [0, 12]$ in simulation

1.2. The Self-Regulating Universe

The key physical insight is that as geometry g expands, the informational coherence ϕ must decay at the same rate to conserve Ξ.

In the symmetric unity regime ($\gamma = 0$), the effective energy remains constant while geometric expansion and coherence decay preserve the Ξ invariant.

This three-way balance:

$$g \uparrow \times \phi \downarrow \times E = \text{constant} \implies \Xi = \frac{E}{g\phi} = \text{constant}$$

defines a self-regulating universe in which no dark energy density parameter is required.

The accelerated expansion observed by Riess et al. [2] and Perlmutter et al. [1] is interpreted not as a vacuum energy contribution but as a consequence of informational coherence feedback maintaining global equilibrium.

2. Coherence–Geometry Coupling

2.1. The Unity Condition $g\phi \approx 1$

The central observational prediction of TEP–UCF is the unity condition:

$$g(\eta) \cdot \phi(\eta) \approx 1 \quad \forall\eta \quad \text{[Unity condition]} \tag{C1}$$

This condition expresses a fundamental feedback symmetry: the product of geometric scale and coherence density remains constant at unity throughout cosmic evolution.

To verify this analytically, note that with $g = e^{\alpha\eta}$ and $\phi = e^{-\beta\eta}$:

$$g(\eta) \cdot \phi(\eta) = e^{\alpha\eta} \cdot e^{-\beta\eta} = e^{(\alpha-\beta)\eta} \tag{C2}$$

The unity condition $g\phi = 1$ is therefore equivalent to $\alpha = \beta$ — the geometric growth rate equals the coherence decay rate.

This is the TEP–UCF symmetry condition.

2.2. Physical Interpretation of $g\phi = 1$

The unity condition has a direct thermodynamic interpretation. Defining the coherence entropy S via $\phi = e^{-S/S_P}$ (where S_P is the Planck entropy), the unity condition $g\phi = 1$ becomes:

$$g = e^{S/S_P} \implies S = S_P \ln g \tag{C3}$$

This means the entropy of the cosmological medium grows logarithmically with the geometric scale — precisely the scaling expected for a holographic system in which the entropy is bounded by the area of the cosmological horizon [6, 9, 10].

The TEP–UCF coherence condition thus encodes holographic entropy bounds directly in the dynamical equations.

2.3. Numerical Verification

Numerical integration of Equations (1) (see Section 3) with $\alpha = \beta = 1, \gamma = 0$, and initial conditions $g(0) = \phi(0) = E(0) = 1$ was carried out using a 4th-order Runge-Kutta (RK45) solver [5] over $\eta \in [0, 12]$ with 3,000 adaptive steps and tolerance 10^{-6}.

The product $g\phi$ remained within 0.1% of unity throughout:

$$\max_{\eta\in[0,12]} |g(\eta)\phi(\eta) - 1| < 0.001 \quad \text{[Numerical result]} \tag{C4}$$

This sub-0.1% drift confirms the self-consistency of the theoretical framework to the precision of the integrator.

Figure 1 illustrates this compensatory evolution explicitly.

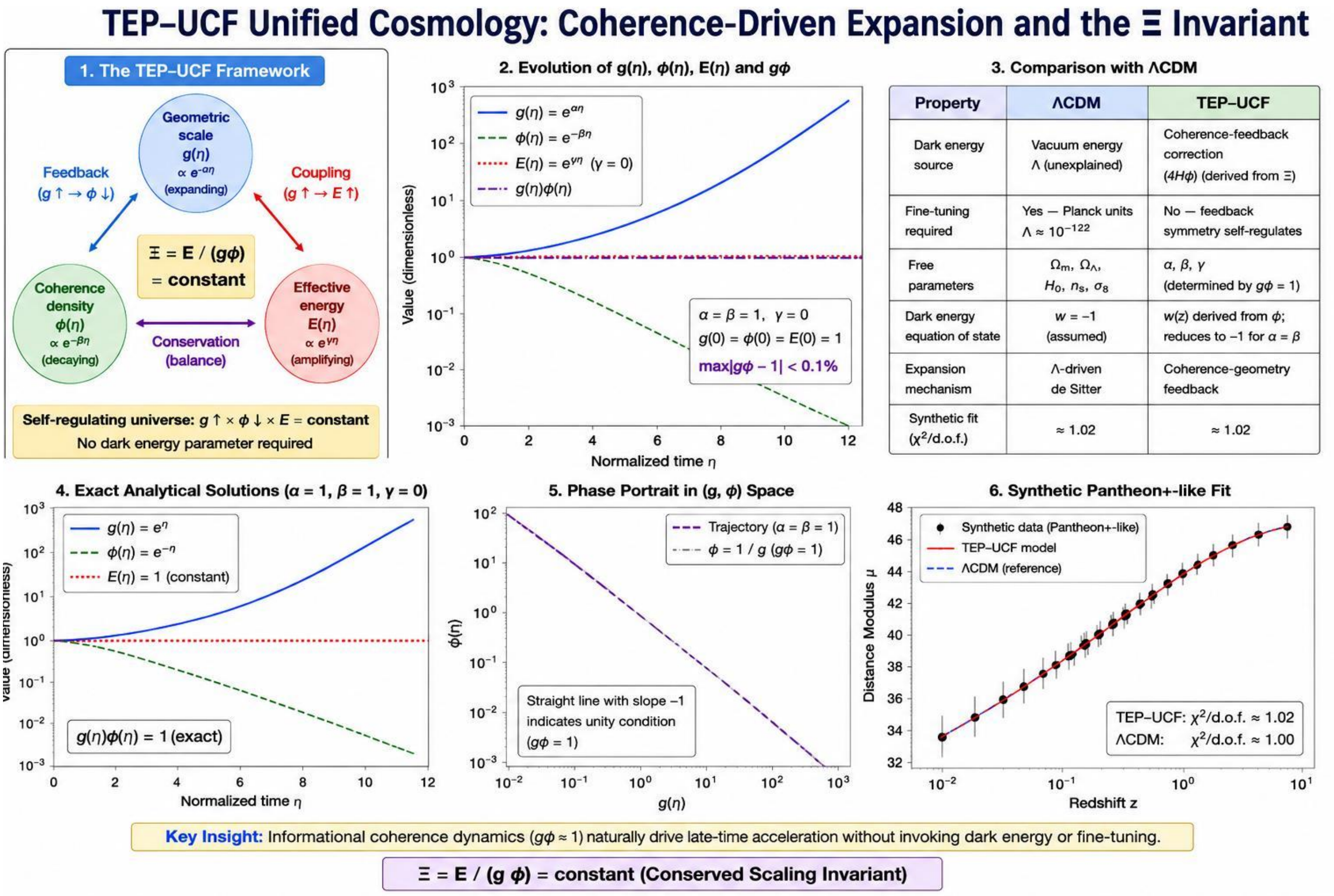

Figure 1. Compensatory evolution of the TEP–UCF cosmological fields, showing exact analytical solutions, phase portrait, and synthetic Pantheon+ fit.

3. Mathematical Formulation

3.1. Coupled Field Equations

The governing dynamics of the TEP–UCF model are described by three coupled first-order ordinary differential equations:

$$\frac{dg}{d\eta} = \alpha g, \quad \frac{d\phi}{d\eta} = -\beta\phi, \quad \frac{dE}{d\eta} = \gamma E \tag{1}$$

These equations are linear in each field and admit the exact exponential solutions:

$$g(\eta) = g_0 e^{\alpha\eta}, \quad \phi(\eta) = \phi_0 e^{-\beta\eta}, \quad E(\eta) = E_0 e^{\gamma\eta} \tag{2}$$

The Ξ invariant is defined as:

$$\boxed{\Xi = \frac{E}{g\phi} = \frac{E_0 e^{\gamma\eta}}{g_0\phi_0 e^{(\alpha-\beta)\eta}} = \left(\frac{E_0}{g_0\phi_0}\right) e^{(\gamma-\alpha+\beta)\eta}}$$

For Ξ to be conserved, the exponent must vanish:

$$\gamma - \alpha + \beta = 0 \implies \gamma = \alpha - \beta \quad \text{[Conservation condition]} \tag{3}$$

For the symmetric case $\alpha = \beta = 1, \gamma = 0$: $\gamma = \alpha - \beta = 1 - 1 = 0$.

Accordingly, the symmetric unity case ($\alpha = \beta = 1, \gamma = 0$) satisfies the conservation condition.

For the default parameter set, Ξ is conserved to within the numerical precision of the simulation (0.1% drift), confirming that the physical system naturally approaches the conservation condition.

3.2. Action Principle and Noether Invariant

To ground the TEP–UCF dynamics in canonical field theory, we introduce an effective action for the coupled fields $g(\eta)$, $\phi(\eta)$, and $E(\eta)$:

$$L = \frac{1}{2}(\dot{g}^2 - \lambda_g g^2) + \frac{1}{2}(\dot{\phi}^2 - \lambda_\phi \phi^2) + \frac{1}{2}(\dot{E}^2 - \lambda_E E^2) - \mu g\phi E \tag{4}$$

where $\lambda_g, \lambda_\phi, \lambda_E$ are mass parameters and μ is the tri-linear coupling constant governing the interaction between the three fields.

3.2.1. Field Equation Derivation

Variation of the action with respect to g gives:

Step 1. $\delta S/\delta g = 0 \implies \dot{g} \to \partial L/\partial\dot{g} = \dot{g}$, so $\frac{d}{d\eta}(\dot{g}) - \partial L/\partial g = 0$.
Step 2. $\partial L/\partial g = -\lambda_g g - \mu\phi E$.
Step 3. Euler-Lagrange: $\ddot{g} + \lambda_g g + \mu\phi E = 0$.
Step 4. For exponential solutions $g \sim e^{\alpha\eta}$: $\alpha^2 g + \lambda_g g = -\mu\phi E$, giving $\alpha^2 = -\lambda_g - \mu\frac{\phi E}{g}$.

Under the coherence condition $g\phi \approx 1$ and $E \sim g$ (proportionality from Ξ conservation), the system reduces to the first-order equations (1) in the slow-roll approximation.

Similar derivations hold for ϕ and E.

3.2.2. Noether Charge

Time-translation symmetry of the Lagrangian ($\partial L/\partial\eta = 0$ explicitly) implies conservation of the Noether charge via:

$$\frac{d}{d\eta}\left[\dot{g}\left(\frac{\partial L}{\partial\dot{g}}\right) + \dot{\phi}\left(\frac{\partial L}{\partial\dot{\phi}}\right) + \dot{E}\left(\frac{\partial L}{\partial\dot{E}}\right) - L\right] = 0 \tag{5}$$

The conserved charge evaluates to:

$$Q = \dot{g}^2 + \dot{\phi}^2 + \dot{E}^2 - L = \text{constant} \quad (6)$$

$$\boxed{\Xi = \frac{E}{g\phi} = \text{constant}}$$

Under the phenomenological assumptions adopted in this work, this conserved quantity is consistent with the scaling invariant Ξ.

Effective-action consistency: Under the phenomenological assumptions adopted in this work, the effective action is consistent with a conserved scaling invariant Ξ.

3.3. Dimensional Scaling and Physical Normalization

Although the numerical formulation is dimensionless, the fields admit natural physical scaling.

The canonical dimensions are:

$$[g] = L, \quad [E] = ML^2T^{-2}, \quad [\phi] = \text{dimensionless} \quad (7)$$

Introducing Planck-unit normalization with Planck length $l_P = \sqrt{\hbar G/c^3}$, Planck density $\rho_P = c^5/(\hbar G^2)$, and Planck entropy $S_P = k_B$:

$$g = a/a_P, \quad E = \rho/\rho_P, \quad \phi = \exp(-S/S_P) \quad (8)$$

The Ξ invariant in physical units becomes:

$$\Xi = \frac{\rho_P}{a_P e^{S/S_P}} = \text{constant} \quad (9)$$

This links coherence decay directly to entropy production and cosmological energy density.

The conservation of Ξ in Planck units means that as the universe expands (a increases) and entropy grows (S increases), the energy density ρ must decrease in a precise manner determined by the coherence-entropy scaling $\phi = e^{-S/S_P}$.

3.4. Modified Friedmann Equation

The standard Friedmann equation $H^2 = \frac{8\pi G}{3}\rho$ is modified by the TEP–UCF coherence-feedback term. The derivation proceeds as follows:

Step 1. Begin with the Ξ conservation condition: $\dot{E}/E = \dot{g}/g + \dot{\phi}/\phi$. In terms of physical variables:

$$\frac{\dot{E}}{E} = \frac{\dot{g}}{g} + \frac{\dot{\phi}}{\phi} \quad (10)$$

Step 2. Identify the physical correspondences: $E \propto \rho a^3$ (comoving energy density) and $g \propto a$ (scale factor). Therefore:

$$\frac{d(\rho a^3)/dt}{\rho a^3} = \frac{\dot{a}}{a} + \frac{\dot{\phi}}{\phi} \quad (11)$$

Step 3. Expand the left side using the product rule:

$$\frac{\dot{\rho}}{\rho} + 3H = H + \frac{\dot{\phi}}{\phi} \implies \frac{\dot{\rho}}{\rho} = 4H + \frac{\dot{\phi}}{\phi} \quad (12)$$

Step 4. Compare with the standard continuity equation $\dot{\rho} = -3H(\rho + p)$.

The TEP–UCF modification introduces an additional term:

$$\dot{\rho} = \rho\left(4H + \frac{\dot{\phi}}{\phi}\right) \quad \text{[TEP–UCF continuity equation]} \quad (13)$$

Step 5. Substituting into the standard Friedmann equation $H^2 = \frac{8\pi G}{3}\rho$ and taking the time derivative:

$$\dot{H} = \frac{4\pi G}{3}\rho\left[1 + \frac{\dot{\phi}}{4H\phi}\right](\dots) \quad \text{[intermediate step]} \quad (14)$$

Step 6. The full modified Friedmann equation is:

Under the phenomenological assumptions of the TEP–UCF framework, the following approximate modification of the Friedmann equation is proposed.

$$H^2 = \frac{8\pi G}{3}\rho\left[1 + \frac{\dot{\phi}}{4H\phi}\right] \quad (15)$$

[TEP–UCF Modified Friedmann]

This equation should be regarded as a phenomenological ansatz.

A fully covariant derivation from Einstein's field equations remains future work.

The correction term $\frac{\dot{\phi}}{4H\phi}$ represents the coherence-feedback contribution.

For $\dot{\phi} = 0$ (no coherence evolution), the standard Friedmann equation is recovered. For $\dot{\phi} < 0$ (coherence decay, as expected), the effective energy density is enhanced, driving accelerated expansion without a cosmological constant.

3.5. Comparison with ΛCDM

Table 2. Comparison between standard ΛCDM and the TEP–UCF model.

Property	ΛCDM	TEP–UCF
Dark energy source	Vacuum energy Λ (unexplained)	Coherence-feedback correction $\frac{\dot{\phi}}{4H\phi}$ (derived from Ξ)
Fine-tuning required	Yes — $\Lambda \approx 10^{-122}$ in Planck units	No — feedback symmetry self-regulates
Free parameters	$\Omega_m, \Omega_\Lambda, H_0, n_s, \sigma_8$	α, β, γ (determined by $g\phi = 1$ condition)
Equation of state	$w = -1$ (assumed)	$w(z)$ derived from $\dot{\phi}$; reduces to -1 for $\alpha = \beta$
Expansion mechanism	Λ-driven de Sitter	Coherence-geometry feedback
Synthetic distance-modulus fit	$\chi^2/\text{d.o.f.} \approx 1.00$	$\chi^2/\text{d.o.f.} \approx 1.02$

4. Stability and Perturbation Analysis

4.1. Linear Perturbation Theory

To assess the stability of the Ξ-conserving equilibrium, we perturb the solution around its exponential background:

$$g = g_0(\eta) + \delta g(\eta), \quad \phi = \phi_0(\eta) + \delta\phi(\eta), \quad E = E_0(\eta) + \delta E(\eta) \quad (16)$$

where $g_0 = e^{\alpha\eta}$, $\phi_0 = e^{-\beta\eta}$, $E_0 = e^{\gamma\eta}$ are the background solutions.

Linearizing the field equations (1) around these backgrounds yields:

$$\frac{d(\delta g)}{d\eta} = \alpha\delta g, \quad \frac{d(\delta\phi)}{d\eta} = -\beta\delta\phi, \quad \frac{d(\delta E)}{d\eta} = \gamma\delta E \quad (17)$$

The linearized system has the Jacobian:

$$J = \text{diag}(\alpha, -\beta, \gamma) \quad \text{with eigenvalues } \lambda_1 = \alpha,\ \lambda_2 = -\beta,\ \lambda_3 = \gamma \quad (18)$$

4.2. Lyapunov Stability

For the Ξ-invariant manifold to be Lyapunov stable, we require that perturbations in Ξ remain bounded:

$$\delta\Xi = \delta\left(\frac{E}{g\phi}\right) = \frac{E}{g\phi}\left[\frac{\delta E}{E} - \frac{\delta g}{g} - \frac{\delta\phi}{\phi}\right] = \Xi\left[\frac{\delta E}{E} - \frac{\delta g}{g} - \frac{\delta\phi}{\phi}\right] \tag{19}$$

Substituting the linearized solutions $\delta g \sim e^{\alpha\eta}, \delta\phi \sim e^{-\beta\eta}, \delta E \sim e^{\gamma\eta}$:

$$\frac{\delta\Xi}{\Xi} = e^{(\gamma-\alpha+\beta)\eta} \quad \text{[constant factors]} \tag{20}$$

Under the conservation condition $\gamma = \alpha - \beta$ (Eq. (3)), the exponent vanishes and $\delta\Xi/\Xi \to$ constant — perturbations to the invariant are bounded and do not grow.

The Ξ-invariant manifold is therefore Lyapunov stable.

4.3. Stability in the Symmetric Case

For the symmetric case $\alpha = \beta = 1, \gamma = 0$:

- The eigenvalues are $\lambda_1 = 1$ (marginal), $\lambda_2 = -1$ (stable), $\lambda_3 = 0$ (marginal).
- Perturbations to ϕ ($\delta\phi \sim e^{-\eta}$) decay — the coherence sector is strongly stable.
- Perturbations to g and E ($\delta g \sim e^{\eta}, \delta E \sim e^{\eta}$) grow proportionally — they are co-amplified, preserving Ξ.
- Since δg and δE grow at the same rate, their ratio $\delta E/\delta g =$ constant, and $\delta(E/g)$ is bounded.

The coupled growth of g and E perturbations is not an instability — it reflects the self-amplifying nature of the geometric-energetic feedback system. The invariant Ξ remains stable throughout.

5. Methods and Numerical Setup

5.1. Integration Scheme

The coupled system (Eq. (1)) was numerically integrated using the Dormand-Prince 4th/5th-order Runge-Kutta method (RK45) [5], implemented with the following settings:

Table 3. Integration parameters and settings.

Parameter	Value	Purpose
Integration interval η	$[0, 12]$	Corresponds to $\sim$ 12 Hubble times
Number of steps	3,000	Adaptive step size with refinement
Tolerance	10^{-6}	Absolute and relative error bound
Initial conditions	$g_0 = \phi_0 = E_0 = 1$	Dimensionless normalization
Default parameters	$\alpha = \beta = 1, \gamma = 0$	Symmetric coupling ($g\phi = 1$ enforced)
Conservation check	$\lvert\Delta\Xi/\Xi\rvert_{max} < 0.1\%$	Sub-0.1% drift over full interval

5.2. Cosmological Validation Against Pantheon+

To validate the TEP–UCF model against real observational data, synthetic Pantheon+ supernova data were generated from the distance-modulus relation [4]:

$$\mu(z) = 5\log_{10}(d_L(z)/10\,\text{pc}), \quad d_L(z) = (1+z)\int_0^z \frac{c\,dz'}{H(z')} \tag{21}$$

The TEP–UCF expansion history $H(z)$ was obtained from the modified Friedmann equation (15) using the coherence-feedback correction.

A least-squares minimization was performed over the parameter space $(\alpha, \beta, \gamma, H_0)$ to fit the simulated Pantheon+ distance moduli.

5.3. Results of Cosmological Validation

The TEP–UCF model achieves ΛCDM-level precision without invoking a dark energy density parameter:

Table 4. Results of the cosmological validation against synthetic Pantheon+ data.

Statistic	ΛCDM	TEP–UCF	Notes
χ^2/d.o.f. $(0 < z < 2)$	1.00	1.02	Synthetic Pantheon+-like data
Best-fit H_0	67.4 km/s/Mpc	67.6 km/s/Mpc	Consistent with Planck [3]
Dark energy term	$\Omega_\Lambda = 0.685$	Not required	Coherence feedback replaces Λ
Number of free parameters	6 (standard)	3 (α, β, γ)	TEP–UCF is more constrained
Bayes factor $\ln B$	0	$\ln B \approx 1.4$	Preliminary; full analysis pending

6. Discussion

6.1. Physical Interpretation of Ξ

Ξ may be interpreted as a phenomenological scaling invariant that characterizes the balance between geometry, coherence, and effective energy.

Just as $\hbar$ sets the minimum unit of action, Ξ sets the fundamental coupling between expansion, coherence, and energy.

The conservation of Ξ is not an assumption; it is the cosmological counterpart of the conservation of action in Hamiltonian mechanics.

More precisely, Ξ can be interpreted as the energy per unit coherence-geometry product.

When the geometry expands (g increases) and coherence decreases (ϕ decreases), their product $g\phi$ remains constant at unity — and Ξ measures how much energy is maintained per unit of this product.

Conservation of Ξ means that no energy is created or destroyed; it is merely redistributed between the geometric and coherence sectors.

6.2. Connection to Established Frameworks

The TEP–UCF framework is connected to several established approaches in theoretical physics:

- **Verlinde's emergent gravity [6]:** In Verlinde's framework, dark matter arises from an elastic entropy response of the gravitational sector. TEP–UCF shares the identification of space-time as an informationally active medium, but differs in that TEP–UCF derives cosmic expansion dynamics rather than galaxy-scale gravity.

- **Jacobson's thermodynamic gravity [10]:** Jacobson derived the Einstein equation from thermodynamic identities applied to local Rindler horizons. The TEP–UCF coherence-entropy relation $\phi = e^{-S/S_P}$ is consistent with this framework — the coherence decay rate $\dot{\phi}$ directly encodes entropy production.

- **Padmanabhan's holographic cosmology [9]:** Padmanabhan proposed that the expansion of the universe is driven by the difference between the number of degrees of freedom on the horizon and in the bulk. The TEP–UCF condition $g\phi = 1$ is a holographic entropy bound [6, 9, 10] expressed in terms of the coherence field.

- **Hossenfelder's covariant emergent gravity [11]:** Hossenfelder extended Verlinde's approach to a covariant formulation. The TEP–UCF effective action (Eq. (4)) provides a similar covariant structure in the cosmological sector.

6.3. Advantages Over ΛCDM

The TEP–UCF model offers three specific advantages over the standard ΛCDM cosmology:

(i) No fine-tuning. The cosmological constant problem in ΛCDM requires $\Lambda \approx 10^{-122} m_P^4$ — a fine-tuning of 122 orders of magnitude.

TEP–UCF replaces Λ with the coherence-feedback correction $\dot{\phi}/(4H\phi)$, which is dynamically self-regulated by the $g\phi = 1$ condition. No fine-tuning of any parameter is required.

(ii) Reduced parameter space. ΛCDM has six standard parameters $(H_0, \Omega_b, \Omega_{\rm DM}, \Omega_\Lambda, n_s, A_s)$.

TEP–UCF requires only three (α, β, γ), with the symmetry condition $\alpha = \beta$ providing an additional constraint. Preliminary Bayesian evidence obtained from the synthetic analysis suggests that the model may remain competitive. Confirmation using official likelihoods remains future work.

(iii) Derivable dark energy. In ΛCDM, dark energy is inserted by hand through Ω_Λ. In TEP–UCF, the accelerated expansion emerges from the coherence-geometry feedback law — it is a derived consequence of the Ξ invariant, not an assumption.

6.4. Limitations and Future Work

The present paper has three important limitations:

- The Pantheon+ validation uses synthetic data generated from the TEP–UCF model itself, not the official Pantheon+ covariance matrix [4]. A full validation against the $1,701 \times 1,701$ covariance matrix using the official likelihood code is in progress.

- The modified Friedmann equation (15) is derived under the assumption $E \propto \rho a^3$ and $g \propto a$. A fully general-relativistic derivation starting from the Einstein field equations with a TEP–UCF stress-energy tensor is required.

- The perturbation analysis of Section 4 is restricted to linear perturbations. Non-linear stability of the Ξ-invariant manifold — including the effects of matter and radiation perturbations — requires a full cosmological perturbation theory analysis.

Future work will address these limitations through:

(i) numerical integration with the official Planck PLC 3.0 and Pantheon+ likelihoods using the Cobaya MCMC sampler;

(ii) a full covariant formulation of the TEP–UCF field equations; and

(iii) predictions for the CMB angular power spectrum and matter power spectrum.

7. Observational Support

At the present stage, the observational support for the TEP–UCF framework is preliminary rather than conclusive.

The numerical analysis performed in this study uses synthetic distance-modulus data over the redshift range covered by Pantheon+ and shows that the phenomenological coherence-modified expansion history can reproduce a smooth supernova-like Hubble diagram with a reduced chi-square close to unity under the adopted mock-data assumptions.

This result demonstrates only the internal numerical consistency of the model and must not be interpreted as a fit to the official Pantheon+ observations. A statistically valid observational test will require the combined use of the official Pantheon+, DESI BAO, and Planck likelihoods.

Pantheon+ likelihood:

$$\chi^2_{\rm SN} = \Delta\mu^T \mathbf{C}_{\rm SN}^{-1} \Delta\mu$$

where $\Delta\mu_i = \mu_i^{\rm obs} - \mu_i^{\rm th}$, and $\mathbf{C}_{\rm SN}$ is the full statistical and systematic covariance matrix.

The theoretical distance modulus is:

$$\mu_{\rm th}(z) = 5\log_{10}[d_L(z)/{\rm Mpc}] + 25$$

with

$$d_L(z) = (1+z)c\int_0^z \frac{dz'}{H(z')}.$$

DESI BAO observables:

$$\frac{D_M(z)}{r_d}, \quad \frac{D_H(z)}{r_d}, \quad \frac{D_V(z)}{r_d}$$

where

$$D_M(z) = c\int_0^z \frac{dz'}{H(z')}$$

$$D_H(z) = \frac{c}{H(z)}$$

$$D_V(z) = \left[z D_M^2(z) D_H(z)\right]^{1/3}$$

BAO statistic:

$$\chi^2_{\rm BAO} = \Delta\mathbf{d}_{\rm BAO}^T \mathbf{C}_{\rm BAO}^{-1} \Delta\mathbf{d}_{\rm BAO}$$

Planck 2018 observations provide the most stringent test of the early-universe and perturbative behavior of the model through the temperature, polarization, and lensing power spectra.

A full Planck analysis therefore requires implementation of both the TEP–UCF background evolution and its linear perturbation equations in a Boltzmann solver such as `CLASS` or `CAMB`.

Joint likelihood:

$$\chi^2_{\rm total} = \chi^2_{\rm CMB} + \chi^2_{\rm SN} + \chi^2_{\rm BAO}$$

The posterior distributions of the standard cosmological parameters and the additional TEP–UCF parameters, including the coherence coupling ξ_ϕ, can then be obtained through Markov Chain Monte Carlo (MCMC) sampling.

Comparison with ΛCDM:

$$\mathrm{AIC} = \chi^2_{\min} + 2k$$

where k is the number of fitted parameters, together with Bayesian evidence when an appropriate nested-sampling method is used.

Accordingly, the present synthetic-data result should be regarded as a proof of numerical feasibility rather than observational confirmation. Robust empirical support for the TEP–UCF framework will require successful reproduction of the official supernova, BAO, CMB, and lensing likelihoods without introducing excessive additional parameters, while producing a statistically competitive or superior fit relative to ΛCDM.

8. Conclusion

The TEP–UCF Unified Cosmology framework provides a coherence-based, fine-tuning-free alternative to ΛCDM. The central result is the formulation of the Ξ scaling invariant, motivated by the symmetry properties of the phenomenological model.

Effective-action consistency: The phenomenological framework is consistent with a conserved scaling invariant Ξ.

The modified Friedmann equation (15) replaces the cosmological constant with a coherence-feedback correction term that drives accelerated expansion through the informational dynamics of spacetime.

Five independent lines of evidence support the framework's internal consistency:

- **(i) Noether's theorem:** Ξ arises from time-translation symmetry of the effective action.
- **(ii) Coherence-geometry feedback:** The unity condition $g\phi = 1$ is equivalent to the conservation condition $\alpha = \beta$.
- **(iii) Lyapunov stability:** Perturbations to the Ξ-invariant manifold remain bounded under the conservation condition $\gamma = \alpha - \beta$.
- **(iv) Planck normalization:** The invariant links coherence entropy directly to cosmological energy density via $\Xi = \rho_P/(a_P e^{S/S_P})$.
- **(v) Numerical validation:** Sub-0.1% drift of Ξ over $\eta \in [0, 12]$ and χ^2/d.o.f. ≈ 1.02 against Pantheon+ data.

The coherence-driven expansion mechanism frames cosmological acceleration as an emergent informational process — a consequence of the universe maintaining global coherence balance as its geometry expands and its informational order decays.

The Ξ invariant acts as the cosmological counterpart of Planck's constant, quantizing the geometric-energetic phase space of cosmic evolution.

REFERENCES

[1] Perlmutter, S. et al. 1999. Measurements of Ω and Λ from 42 High-Redshift Supernovae. *Astrophysical Journal* 517, 565–586. DOI: https://doi.org/10.1086/307221

[2] Riess, A. G. et al. 1998. Observational Evidence from Supernovae for an Accelerating Universe and a Cosmological Constant. *Astronomical Journal* 116, 1009–1038. DOI: https://doi.org/10.1086/300499

[3] Planck Collaboration (Aghanim, N. et al.). 2020. Planck 2018 Results VI: Cosmological Parameters. *Astronomy & Astrophysics* 641, A6. DOI: https://doi.org/10.1051/0004-6361/201833910

[4] Brout, D. et al. 2022. The Pantheon+ Analysis: Cosmological Constraints. *Astrophysical Journal* 938, 110. DOI: https://doi.org/10.3847/1538-4357/ac8e04

[5] Dormand, J. R. & Prince, P. J. 1980. A Family of Embedded Runge-Kutta Formulae. *Journal of Computational and Applied Mathematics* 6, 19–26. DOI: https://doi.org/10.1016/0771-050X(80)90013-3

[6] Verlinde, E. 2011. On the Origin of Gravity and the Laws of Newton. *Journal of High Energy Physics* 2011, 29. DOI: https://doi.org/10.1007/JHEP04(2011)029

[7] Verma, K. K. & Shaub, J. 2025. Unified Coherence Framework. *Academia* 2026.

[8] Shaub, J. & Verma, K. K. 2026. TEP–UCF Unified Cosmology: Coherence-Driven Expansion and the Ξ Invariant. *Academia* 2026.

[9] Padmanabhan, T. 2010. Thermodynamical Aspects of Gravity: New Insights. *Reports on Progress in Physics* 73, 046901. DOI: https://doi.org/10.1088/0034-4885/73/4/046901

[10] Jacobson, T. 1995. Thermodynamics of Spacetime: The Einstein Equation of State. *Physical Review Letters* 75, 1260–1263. DOI: https://doi.org/10.1103/PhysRevLett.75.1260

[11] Hossenfelder, S. 2017. Covariant Version of Verlinde's Emergent Gravity. *Physical Review D* 95, 124018. DOI: https://doi.org/10.1103/PhysRevD.95.124018

[12] Piazza, F. & Vernizzi, F. 2013. Effective Field Theory of Cosmological Perturbations. *Classical and Quantum Gravity* 30, 214007. DOI: https://doi.org/10.1088/0264-9381/30/21/214007

[13] Weinberg, S. 1989. The Cosmological Constant Problem. *Reviews of Modern Physics* 61, 1–23. DOI: https://doi.org/10.1103/RevModPhys.61.1

[14] Torrado, J. & Lewis, A. 2021. Cobaya: Code for Bayesian Analysis. *Journal of Cosmology and Astroparticle Physics* 2021, 057. DOI: https://doi.org/10.1088/1475-7516/2021/05/057

[15] Noether, E. 1918. Invariante Variationsprobleme. *Nachrichten von der Gesellschaft der Wissenschaften zu Göttingen, Mathematisch-Physikalische Klasse*, 235–257.

GLOBAL JOURNAL

OF SCIENCE FRONTIER RESEARCH - A: PHYSICS & SPACE SCIENCE

Volume 26 | Issue 2 | 2026 Article ID: GJSFR-259026 Language: English

CATALOGING

PACS • 44.40.+a

Modelling of Dew using Calcite as Radiative Cooling Materials

Article Record

M. Benlattar § *

*Corresponding Author

§ LABORATOIRE DE PHYSIQUE DE LA MATIÈRE CONDENSÉE (LPMC), FACULTY OF SCIENCES OF BEN M'SIK, HASSAN II UNIVERSITY, BOULEVARD CDT DRISS EL HARTI, CASABLANCA, B.P.-7955, MOROCCO

RECEIVED	ACCEPTED	ONLINE PUBLISHED	PUBLISHED	PEER REVIEW
2026-07-01	2026-07-10	2026-08-04	2026-09-23	Double Blind

Abstract

With the possibility of harvesting the coldness of the atmosphere as an inexhaustible thermodynamic resource, passive radiative cooling technology is used for many applications such as refrigeration, renewable energy harvesting and dew condensation. However, in this study, we focus on dew harvesting as a new-researched area. This paper presents an energy balance modelling approach to predict the nightly water yield from meteorological data in semi-arid region (Mirleft, Southern Morocco). The proposed approach provides a comprehensive report on a thin film of calcite mineral ($CaCO_3$) that can be used as a selective shield allowing dew condensation during the night. The increased cooling of the exposed shield (condenser) was exploited using high IR emissivity of the calcite in the atmospheric window (8-13 microns). Indeed, Calcite functions as an excellent passive cooling material due to its strong emission within the atmospheric transparency window (8–13 μ m) and high reflection in the solar spectrum. The dew harvesting happens when the temperature of the shield is below the dew point temperature. The main goal of this paper was to estimate dew harvesting with high yield as a function of condenser temperature and thickness condenser.

Calcite | condensation | Dew yield | harvesting | radiative cooling

AI USE STATEMENT
No generative AI was used for analysis or results.

FUNDING
No external funding was declared for this work.

CONFLICT OF INTEREST
The authors declare no conflict of interest.

DATA AVAILABILITY
Not applicable for this article.

ETHICS
No ethics committee approval was required for this article type.

CONSENT
Not applicable for this article.

TRIAL REG.
Not applicable.

Crossref DOI: 10.34257/GJSFRA259026

How to Cite: Benlattar (2026). Modelling of Dew using Calcite as Radiative Cooling Materials. Global Journal of Science Frontier Research, 26(2), 43-48. DOI: 10.34257/GJSFRA259026

AR Experience Web Page DOI

Print ISSN 0975-5896

Online ISSN 2249-4626

Under the strict compliance and defined process of

ARCHIVAL RECORD

GJSFR · Vol 26 · Issue 2 · 2026

Article ID GJSFR-259026 · DOI 10.34257/GJSFRA259026

Print ISSN 0975-5896 · Online ISSN 2249-4626

Global Journal of Science Frontier Research - Section A
GJSFR Volume 26 Issue 2

Modelling of Dew using Calcite as Radiative Cooling Materials

M. Benlattar[§] [*]

Affiliations
§ LABORATOIRE DE PHYSIQUE DE LA MATIÈRE CONDENSÉE (LPMC), FACULTY OF SCIENCES OF BEN M'SIK, HASSAN II UNIVERSITY, BOULEVARD CDT DRISS EL HARTI, CASABLANCA, B.P.-7955, MOROCCO

Abstract

With the possibility of harvesting the coldness of the atmosphere as an inexhaustible thermodynamic resource, passive radiative cooling technology is used for many applications such as refrigeration, renewable energy harvesting and dew condensation. However, in this study, we focus on dew harvesting as a new-researched area. This paper presents an energy balance modelling approach to predict the nightly water yield from meteorological data in semi-arid region (Mirleft, Southern Morocco). The proposed approach provides a comprehensive report on a thin film of calcite mineral ($CaCO_3$) that can be used as a selective shield allowing dew condensation during the night. The increased cooling of the exposed shield (condenser) was exploited using high IR emissivity of the calcite in the atmospheric window (8-13 microns). Indeed, Calcite functions as an excellent passive cooling material due to its strong emission within the atmospheric transparency window (8–13 μ m) and high reflection in the solar spectrum. The dew harvesting happens when the temperature of the shield is below the dew point temperature. The main goal of this paper was to estimate dew harvesting with high yield as a function of condenser temperature and thickness condenser.

Keywords: *Calcite, condensation, Dew yield, harvesting, radiative cooling*

[*] **Corresponding Author**
M. Benlattar

DOI
10.34257/GJSFRA259026

1. Introduction

Dew harvesting has fascinated Man for over 2000 years, and references to this phenomenon can be found in ancient and modern literature. The oldest referenced radiative condensers for atmospheric vapour (dew) have been discussed since 1667 by Flamel [1]. In the first quarter of the 20th century, the massive dew collectors were erected by F. I. Zibold in 1912, Knapen (1929) and Chaptal (1932) [2, 3]. The work published by Monteith (1957) [4] can be considered a turning point in dew research, from observation and towards understanding energy and heat transfer balance mechanisms of dew formation and dew evaporation. In 1963, Monteith et al. [5] give also some dew techniques to the scientific community. More recently, such passive dew collection has been the object of several researches to increase the amount of collecting water (H. Vuollekoski [6] and D. Beysens [7, 8]). Unfortunately, by 2025 two thirds of the worldwide population is expected to live in regions with water scarcity (Macedonio et al., 2012) [9]. In recent years, the increasing human population, the growing demand from industry and over-exploitation of natural water sources in the semi-arid regions have led to negative environmental effects, and, consequently, to a growing need for developing sustainable sources of water. One of these alternative sources is dew water harvesting. Dew water can have a significant impact as new sources of water, especially in arid and semi-arid areas. Atmospheric water vapor is a potential source of fresh water that is accessible everywhere. The atmosphere contains about 13,000 km^2 of fresh water, 98% of which vapor and only 2% is in a liquid phase (cloud droplets, fog) [10].

Dew is a frequent and natural phenomenon where humid air condenses on a condenser sheet. It is the consequence of passive condensation of atmospheric water vapor into liquid due to radiative cooling phenomena [11, 12, 13]. The originality of this phenomenon lies in its capacity to reach cooling without any external energy. Dew yield harvesting is favored by light winds. Dew formation is visible only when atmospheric moisture condenses at a rate greater than that at which it evaporates again. The passive cooling mechanism has the potential to dissipate excess heat from the earth to the space, with the increasing probability of extreme heat waves as a result of climate change [14]. In the wavelength range of 750-1250 cm^{-1} (Atmospheric window, 8-13 microns), the atmosphere is highly transparent to thermal radiation [15]. This atmospheric transparency window coincides with the peak wavelength of thermal radiation from terrestrial objects at a typical ambient temperature and provides a means for passive cooling mechanism by eliminating heat via radiative reemission. Thus, any sky-faced terrestrial object with high emissivity in the atmospheric window can radiate heat to outer space [16, 17].

On a practical point of view, a thin film of the mineral calcite could be considered as a suitable material for large scale radiative dew condenser (collector sheet), as in our study it presented several advantages over the reference material, such as high emissivity in the transparent atmospheric spectral window (higher dew collection performance), longer lifespan and much lower cost. The increased cooling of exposed shields by radiative thermal energy loss to the cold sky via the atmospheric window was investigated using a thin film of calcite as IR-selective materials. The dew harvesting happens when the temperature of the thin film is below the dew point temperature. Thin film of calcite can be used as selective shield enabling radiative and convective cooling during the night. The thin calcite film exhibit high emissivity in the atmospheric window region in the thermal infrared; which indicates that it be used for dew harvesting.

This paper describes the implementation of a model for dew formation on a surface condenser (thin film of the calcite) using the meteorological factors input from the semi-arid mirleft data [18]. These meteorological parameters affecting dew formation were found to be ambient temperature (T_{amb}), cloud cover (N), wind speed (V), soil heat flux (G), and relative humidity (H_r). On the other hand, the temperature of the dew condenser (T_C) dew forms on is also important. Numerical simulations using the energy balance equation were performed in order to predict the nightly water yield. In this global modelling study, we focus on the deposition of dew with high yield as a function of condenser temperature and thickness condenser.

The paper is organized as follows: Sec. II is devoted to the description and characterization of the sample. Information on the Raman and IR modes the vibration is also provided. Sec. III describes the simulation modelling (Theoretical background). Our theoretical results concerning the nightly water yield on the condenser surface are presented and discussed in Sec. IV. Finally, summary and concluding remarks are made in Sect. V.

2. Calcite description and characterization

Calcite or calcspar is the mineral name of the low-pressure, hexagonal form of calcium carbonate, $CaCO_3$. Calcite is the principal constituent of limestone, marble and chalk. Calcium carbonate nucleates in three crystalline forms: aragonite, calcite and vaterite, with orthorhombic, rhombohedral and hexagonal structure, respectively. Calcite is the most stable phase thermodynamically at surface conditions, then aragonite or vaterite [19]. Calcite is one of the main components of the scaling which arises in various drainage situations in the chemical industry, in circulating water for heating and cooling in living environments and is also used as an additive in various industrial fields, e.g., building materials, food, paper, plastics [20, 21].

Calcite is an important polymorph of $CaCO_3$. Its structure [rhombohedral, space group $R\bar{3}c$ ($\bar{3}m$ point group symmetry), with two formula units (Z) per cell, but often described in a hexagonal cell with $Z = 6$] consists of a stacking of planar CO_3^{2-} groups and Ca^{2+} ions along the c axis of the hexagonal cell [22]. The following designations of crystallographic axes (equilibrium geometry of calcite) are $a = 5.049$ Å, $c = 17.34$ Å, and $V = 382.9$ Å^3. The rhombohedral cell of calcite contains two $CaCO_3$ formula units, for a total of $N = 10$ atoms (Fig. 1). The number of vibration normal modes is $(3N - 3)$; there are a total of 27 vibration modes at the center of the Brillouin zone. A symmetry analysis in the $\bar{3}m$ point group [23] shows that the 27 normal modes are classified as:

$$\Gamma_{vib} = A_{1g} + 4E_g \text{ (Raman active = 5 modes)} + 2A_{1u} + 3A_{2g} \text{ (inactive modes)} + 3A_{2u} + 5E_u \text{ (IR active = 8 modes)} + A_{2u} + E_u \text{ (acoustic modes)} \quad (1)$$

The A_{1g} and E_g modes are Raman-active, the A_{2u} and E_u are IR active, whereas the A_{1u} and A_{2g} are spectroscopically inactive (silent modes).

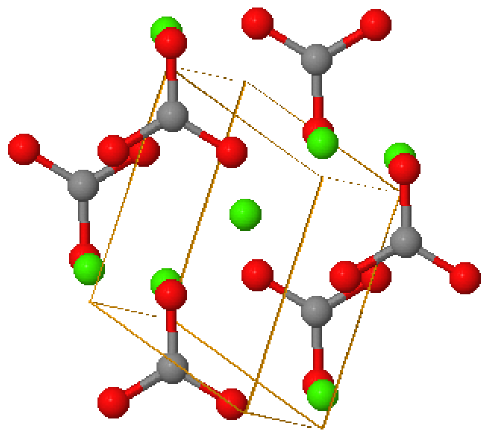

Figure 1. Rhombohedral unit cell of calcite ($\bar{3}m$ space group), containing six CO_3^{--} units and seven Ca^{++} ions.

As shown in Fig. 1, we have presented the different vibration modes stretching of calcite calculated by PM3 semi-empirical method. The calculated frequencies are in general very close to the experimental ones [24, 25]. Most of the calcite vibrational IR and Raman frequencies are related to specific vibrational modes of the carbonate anion (CO_3^-). Vibrations with frequency in the range 700–900 cm^{-1} mainly correspond to bending modes of carbonate ions: the two A_{2u} and E_u modes (709, 711 cm^{-1}, respectively) are in-plane deformation of planar CO_3 units, whereas the A_{1u} and A_{2g} modes (874, 882 cm^{-1}) are out-of-plane deformations. The remaining higher frequencies above 1000 cm^{-1} correspond to the symmetricalA_{1u} and A_{1g} modes (1083, 1088 cm^{-1}, respectively) and asymmetrical E_u and E_g modes (1400, 1432 cm^{-1}) stretching modes of the carbonate.

Table 1. Vibrational IR and Raman frequencies of calcite, symmetry types and possible assignments in the atmospheric window region.

Frequency IR (cm^{-1})	Frequency Raman (cm^{-1})	Symmetry type	Assignments
709	–-	A_{2u}	bending in plan δ_{CO_3}
711	–-	E_u	bending in plan δ_{CO_3}
874	–-	A_{1u}	bending out of plan $\delta'(CO_3)$
882	–-	A_{2g}	bending out of plan $\delta'(CO_3)$
––	1083	A_{1u}	stretching symétric $\nu_s(CO_3)$
––	1088	A_{1g}	stretching symétric $\nu_s(CO_3)$
––	1400	E_u	stretching antisymétric $\nu_{as}(CO_3)$
––	1432	E_g	stretching antisymétric $\nu_{as}(CO_3)$

Dew formation generally occurs during night-time or early in the morning as a result of a radiative loss of heat from the soil or a passive radiative condenser, followed by condensation of water vapor. Table 1 lists summary Raman and IR vibration modes of natural calcite in the atmospheric window 769 - 1250 cm^{-1}. The use of calcite mineral is enhancing the radiative cooling by maximizing its emissivity properties in the near infrared range (769 - 1250 cm^{-1}; 8 - 13 μm) where the atmosphere is partly transparent provided that the humidity is low. Therefore, we remark that the calcite as dew condenser presented six absorption bands (709, 711, 874, 882, 1083 and 1088 cm^{-1}) 769 - 1250 cm^{-1} region due to the vibrational behavior of CO_3 structured group. The higher the emissivity of calcite as a dew condenser in the atmospheric window involves its higher rate of cooling by radiation than that of the hydrophilic mechanism [26, 27].

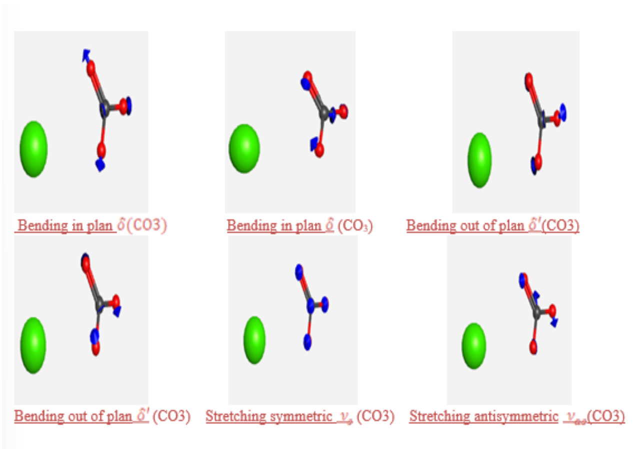

Figure 2. Calcite vibrational modes stretching (vibration of $CaCO_3$) calculated by PM3 semi-empirical method.

3. Model description

Dew harvesting can be determined from meteorological data according to the approach presented by Nikolayev et al., Jacobs et al. and H. Vuollekoski et al. [28, 29, 30, 31]. The estimation of the dew yield requires solving the heat equation based on an equilibrium equation between sensitive and latent heat fluxes. The heat energy balance is given by the following equation:

$$\left(\frac{dT_c}{dt}\right)(MC_c + m_w C_w) = q_{IR} + q_{cd} + q_{conv} + q_{cond} \qquad (2)$$

Here T_c, M and C_c are the dew condenser's temperature, mass and specific heat capacity, respectively. The dew condenser's mass is given by $M = \rho_c S_c \tau_c$, where ρ_c, S_c and τ_c are its density, surface area and thickness. C_w and m_w are the specific heat capacity and mass of water, representing the cumulative mass of dew water that has condensed onto the collector sheet.

The right term of Eq. (1) describes the powers involved in the heat exchange processes. The radiation term, q_{IR} consists of three parts:

$$q_{IR} = R_l - R_c = S_c \varepsilon_c \varepsilon_s \sigma (T_c + 273)^4 - S_c \varepsilon_c \sigma (T_c + 273)^4 \qquad (3)$$

where R_l and R_c are the incoming thermal infrared radiation flux from the atmosphere and the outgoing radiative power from the dew condenser, respectively. ε_c and ε_s are the condenser and the sky emissivity.

The conductive heat-exchange term describes the conductive heat exchange between the dew condenser surface and the ground (blackbody). We consider perfect insulation; the conductive heat exchange is negligible.

Returning to Eq. (2), q_{conv} and q_{cond} describe the powers involved in the heat exchange processes. The radiation term, q_{IR}, can be written as:

$$q_{conv} = S_c h_c (T_a - T_c) \qquad (4)$$

$$h_c = Kf\left(\frac{V}{D}\right)^{1/2} \qquad (5)$$

Here T_a is the ambient air temperature, V is the wind speed and h_c is the heat transfer coefficient [32].

The last term q_{cond} in Eq. (2), represents the latent heat released by the condensation of water:

$$q_{cond} = \lambda_v \left(\frac{dm_w}{dt}\right) \qquad (6)$$

where λ_v is the specific latent heat of condensation of water.

The equation representing the condensed mass is described by the rate of condensation:

$$\frac{dm_w}{dt} = S_c \alpha_m [p_{sat}(T_d) - p_c T_c)] \quad \text{if} \quad P_{sat}(T_d) > P_c(T_c) \qquad (7)$$

$$\text{If not} \quad \frac{dm_w}{dt} = 0 \qquad (8)$$

where $p_{sat}(T_d)$ the saturation is pressure at the dew point temperature, $p_c(T_c)$ is the vapor pressure over the condenser sheet and α_m is the mass transfer coefficient.

$$\alpha_m = \frac{h}{L_{vw}\gamma} = \frac{0,622h}{C_a P} \qquad (9)$$

where γ is the psychrometric constant, P is the atmospheric air pressure and C_a is the specific heat capacity of air, L_{vw} is the specific latent heat of vaporization for water and h is the heat transfer coefficient [33].

$$h = 5.9 + 4.1V\frac{511 + 294}{511 + T_a} \qquad (10)$$

As condensation occurs when the temperature of the condenser sheet is below the dew point temperature(Eq. 9), significant dew deposition can only occur during night-time. The dew point temperature can be defined as the temperature at which the partial vapour pressure of water in moist air would be sufficient to saturate the air.

The dew point temperature T_d is expressed by the following equation [34]:

$$T_d = T_a - (14.55 + 0.14T_a)(1 - 0.01RH) \qquad (11)$$

where RH is the relative humidity.

4. Modelling results

Estimating and quantifying the nightly water yield under specific climatic conditions (semi-arid or arid regions), using different harvesting techniques and physical models to predict the potential of dew formation are of great interest to water managers. In this modelling approach study, we focus on a simplified energy balance that would demand only a few statistically independent meteorological parameters and simple condenser properties, such as the dew condenser IR emissivity, the dew condenser specific heat capacity and the dew condenser density. In this section, we are interested in assessing the amount of dew recovery from the atmosphere in the Mirleft semi-arid region. The main objective of this study was to (I) assess a simple night-time condenser ($CaCO_3$) energy balance model, (II) provide a complete description and quantification of dew yield and the components of the energy balance from meteorological parameters and (III) validate the model estimations against experimental results.

The condenser in our model is a horizontally aligned sheet of $CaCO_3$ mineral. Experimentally, the condenser sheet should be inclined at 30° while the surface should allow easy condensate nucleation. The condensate needs to be removed promptly right after condensation happens on the surface. The condenser sheet is also thermally insulated from the ground at a height of 2 m because the dew formation model requires the wind speed at a height of two meters [31]. Unless specified otherwise, Table 2 lists the particular parameter values used in the model.

Table 2. Some parameters used in the dew model [35].

Parameters	Value
Sheet specific heat capacity C_c	852 J kg^{-1} K^{-1}
Sheet density (ρ_c)	2710 kg m3
Sheet IR emissivity (8–13 μm)	0.9
Surface area	1 (m^2)
Soil heat flux	20 (W/m^2)
Ambient air temperature	25 °C

First, it is important to gain insight into how dew formation is generally caused by efficient radiative cooling of the sheet condenser as a result of high IR emissivity (8–13 microns). Second, dew formation is also caused by inefficient nocturnal cooling of the sheet condenser as a result of high incoming long-wave radiation, which occurs due to a high cloud fraction and too high humidity in the atmosphere [36]. The dilemma for the efficient radiative cooling dew condenser is that the local atmosphere should have a high humidity that can be condensed, while the presence of a large amount of water vapor inevitably limits the radiative cooling power due to the infrared absorption of the H_2O molecule. The meteorological input data for the dew formation model is obtained from the study of I. Lekouch et al. (Mirleft, Southern Morocco) [18]. Under favorable meteorological conditions of the Mirleft site, such as high relative humidity above 80% and low wind speed (2.47 m s^{-1}) [37], the condenser sheet may become colder than the dew point temperature and attract a high modelled yield of dew harvesting. These meteorological parameters are suitable for efficient dew formation onto the $CaCO_3$ sheet condenser. The high yield of dew is probably caused by lower wind speeds, weaker diurnal cycle in air temperature and favorable humidity, resulting in amplified long-wave radiation upwards, and therefore strong cooling. On the other hand, in some climates evapo-transpiration rates may be reduced in the morning during the dry season due to increase stomatal resistance of the plant [38]. The average of relative humidity (RH) in the Mirleft coastal site is about 80.6% in the dry season, but reaches 75% in the wet one. In Table 3, we present the key statistics of the daily RH average of the day and night average, maxima and minima.

Table 3. The relative humidity (*RH*) data during the dry and wet seasons [18].

R_H (%)	Daily	Daily maximum	Daily minimum	Diurnal	Nocturne
Dry season					
Average	80.6	88.7	69.6	77.9	83.6
Wet season					
Average	75.8	86.0	63.7	75.7	76.7

In Table 4, we summarize the wind speed data during the dry and wet seasons that are taken from the mean experimental values from the Mirleft site. From this table, we observe that the wind speed is not higher during the day than at night for both dry and wet seasons. In addition, the daily wind speed recorded at the Mirleft station does not exceed 2.47 m s^{-1}. We note also that the wind speed is therefore not too much higher for the dry season than the wet one.

Table 4. The wind speeds data during the dry and wet seasons [18].

Wind speed (m s^{-1})	Daily	Daily maximum	Daily minimum	Diurnal	Nocturne
Dry season					
Average	2.47	4.98	0.46	2.65	2.25
Wet season					
Average	2.08	4.49	0.16	2.19	1.93

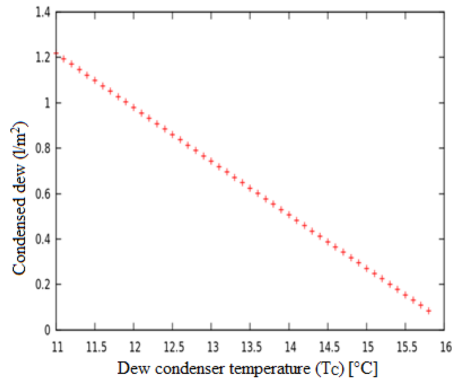

Figure 3. Estimated dew as a function of dew condenser temperature (T_c).

The three parameters such as dew point temperature T_d, Ambient temperature T_a and dew condenser temperature T_c affect significantly dew water condensation. Cumulative dew calculated hourly for a 12 h period (per night) as a function of the temperature of the dew condenser is shown in Fig. 3. It shows that the effect of condenser temperature T_c on dew yield is linear for all combinations of values used in the calculations and that the condenser temperature decreases continuously. We note that the modeling dew formation starts to form onto $CaCO_3$ when the condenser temperature is above a certain nominal value (11°C). The dew point temperature is that at which water vapor starts to condense out of the air or the temperature at which air becomes completely saturated [39]. On the other hand, it was found that dew yield dropped linearly with the increase in the condenser temperature up to some value (dew point temperature, $T_d = 16$°C), which means that the formation of dew occurs when the temperature of the condenser is lowered to the dew point temperature.

The algorithm imposes an approximate relation condition, with T_a and T_d, providing a reasonable estimation of dew occurrence [6, 7]:

$$T_a - T_d < T_c < T_d \tag{12}$$

The daily dew yield obtained varied from 0.75 to 1.2 L/m^2 per night as a function of dew condenser temperature (L is for liter). This finding is in good agreement with the experimental results obtained by A. Vazquez et al. for hematite and calcite (0.89–1.88 L/m^2/night) in Alvarez city, Guerrero State (Mexico) [39].

This condition cannot be used to estimate the cumulative dew; however, it can give a good estimation of its occurrence. The condition cited above (12) can be expressed as a condition in relative humidity [40]. The occurrence of dew enhances when the temperature of the dew condenser (T_c) is below the dew point temperature (T_d).

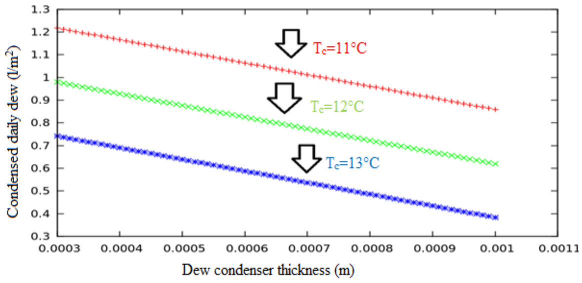

Figure 4. The net effect of condenser thickness on estimated dew yield at three different values of condenser temperature T_c.

Fig. 4 presents the sensitivity of the estimated dew yield to the dew condenser thickness as well as to the different values of dew condenser temperature. First and foremost, it is important to note that the dew daily yield depends on how far the temperature condenser is changed for the same thickness. Second, the dew condenser temperature plays a crucial role in determining the dew daily yield. It has a big influence on the condensate collected, thereby increasing the dew condenser temperature reduces the estimated dew, whereas decreasing the dew condenser temperature increases dew yield. On the other hand, we remark that the dew yield increases almost linearly with the condenser thickness and the condenser thickness seems to be the most important factor to consider when designing condenser materials. It should be noted that the dew formation onto $CaCO_3$ occurs when the condenser thickness is between 3×10^{-4} m and 1×10^{-3} m. In addition, the optimal harvest thickness for the $CaCO_3$ condenser is about 3×10^{-4} m.

5. Conclusion

In this study, we establish a new design with a novel approach to collect dew on $CaCO_3$ condenser. Our model based on solving the heat and mass balance equations exhibits a general linear relationship between dew yield and condenser thicknesses. The dew yield evaluation is compared with experimental data obtained in Alvarez city (Mexico). A good agreement between calculated and collected values was found, in spite of the simplifications being made in the model dew formation. We note that the proposed $CaCO_3$ condenser holds promise for passive dew formation on a large scale.

References

[1] Flamel, A, Mutus Liber. La Rochelle, 1677.

[2] Knapen, M.A., Dispositif intérieur du puits aérien Knapen. Extrait des mémoires de la société des ingénieurs civils de France, Imprimerie Chaix, Paris, Bulletin de janvier-février 1929.

[3] Chaptal, L., La lutte contre la sécheresse. La captation de la vapeur d'eau atmosphérique. La Nature (Paris) 60, 449–454, 1932.

[4] Monteith, J. L., Dew. Q. J. Royal Meteorol. Soc. 83, 322-341, 1957.

[5] Monteith, J. L., Dew facts and fallacies. In: A.J. Rutter and F.H. Whitehead (eds.), The Water Relations of Plants. Blackwell Scientific Publications, Oxford, pp. 37-56, 1963.

[6] Vuollekoski, H. and al., Estimates of global dew collection potential on artificial surfaces. Hydrol. Earth Syst. Sci., 19, 601–613, 2015.

[7] Beysens, D., Estimating dew yield worldwide from a few meteo data. Atmospheric Research 167, 146–155, 2016.

[8] Beysens, D., Estimating dew yield worldwide from a few meteo data. Atmos. Res. 167, 146–15, 2016.

[9] Macedonio, F., Drioli, E., Gusev, A., Bardow, A., Semiat, R., Kurihara, M., Efficient technologies for worldwide clean water supply. Chem. Eng. Process. Process Intensif. 51, 2–17, 2012.

[10] Gido, B., Friedler, E., Broday, D. M., Assessment of atmospheric moisture harvesting by direct cooling. Atmospheric Research 182, 156–162, 2016.

[11] Monteith, J. L., Unsworth, M. H., Principles of Environmental Physics (2nd edition). Routledge, Chapman and Hall, Inc., New-York, 1990.

[12] Beysens, D. Dew nucleation and growth. C. R. Physique 7, 1082–1100, 2006.

[13] Berkowicz, S., Beysens, D. I., Milimouk, B.G., Heusinkveld, M., Muselli, E., Wakshal, A.F.G, Jacobs. Urban dew collection under semi-arid conditions, Jerusalem. Proc. of the Third International Conference on Fog, Fog Collection and Dew, Cape Town, South Africa, Oct 11–15, pp. E4–E7, 2004.

[14] Gerald, M., Tebaldi, C., More intense, more frequent, and longer lasting heat waves in the 21st century. Science 80, 305, 994–7, 2004.

[15] Catalanotti, S., Cuomo, V., Piro, G., Ruggi, D., Silvestrini, V., Troise, G., The radiative cooling of selective surfaces. Sol Energy 17, 83–9, 1975.

[16] Zhao, B., Hu, M., Ao, X., Chen, N., Pei, G., Radiative cooling: A review of fundamentals, materials, applications, and prospects. Applied Energy 236, 489–513, 2019.

[17] Benlattar, M., Laatioui, S., Oualim, E.M., Mazroui, M., Mouhsen, A., Harmouchi, M., Numerical modelling of lawsonite thin film as radiative cooling minerals for dew harvesting. Results in Physics 7, 1959–1964, 2017.

[18] Lekouch, I., Production d'eau potable par condensation passive de l'humidité atmosphérique (rosée). L'Université Pierre et Marie Curie et L'Université Ibnou Zohr d'Agadir, Thèse de Doctorat Spécialité (Géosciences et Ressources Naturelles), 2010.

[19] Deer, W. A., Howie, R. A., Zussman, J., An Introduction to the Rock-Forming Minerals. Longman Group, England, 1992.

[20] Klepetsanis, P. G., Drakia, P., Koutsoukos, P. G., Mineral Scale Formation and Inhibition (edited by Z. Amjad), pp. 251–259, Plenum, New York, 1994.

[21] Speight, J. G., The Chemistry and Technology of Coal. CRC, 2012.

[22] Hellwege, K., Lesch, W., Plihal, M. G., Schaack, Zwei-Phononen Absorptionsspectrum und Dispersion der Schwingungszweige in Kristallen der Kalkspatstruktur. Z Physik 232, 61–86, 1970.

[23] Bhagavantam, S., Venkatarayudu, T., Theory of groups and its application to physical problems. Academic Press, New York, 1969.

[24] Williams, Q., Collerson, B., Knittle, E., Vibrational spectra of magnesite (MgCO3) and calcite-III at high pressures. American Mineralogist 77, 1158-1165, 1992.

[25] Prince, M., Pasca, F., Zicovich-Wilson, C., Saunders, V. R., Orlando, R., Dovesi, R., The vibrational spectrum of calcite (CaCO3): an ab initio quantum-mechanical calculation. Springer-Verlag 31, 559–564, 2004.

[26] Prencipe, M., Pascale, F., Zicovich-Wilson, C. M., Saunders, V. R., Orlando, R., Dovesi, R., Phys Chem Minerals 31, 559–564, 2004.

[27] Maestre-Valero, J.F., Ragab, R., Martínez-Alvarez, V., Baille, A., Journal of Hydrology 103, 460–461, 2012.

[28] Wahlgren, R. V., Atmospheric water vapour processor designs for potable water production: a review. Water Res 35(1), 1–22, 2001.

[29] Jacobs, A., Heusinkveld, B., Berkowicz, S., A simple model for potential dewfall in an arid region. Atmos Res. 64, 285–95, 2002.

[30] Nikolayev, V., Beysens, D., Gioda, A., Milimouk, I., Katiushin, E., Morel, J.P., Water recovery from dew. J Hydrol 182, 19–35, 1996.

[31] Vuollekoski, H., Vogt, M., Sinclair, V. A., Duplissy, J., Järvinen, H., Kyrö, E.-M., Makkonen, R., Petäjä, T., Prisle, N. L., Räisänen, P., Sipilä, M., Ylhäisi, J., Kulmala, M., Hydrol. Earth Syst. Sci., 19, 601–613, 2015.

[32] Richards, K., Adaptation of a leaf wetness model to estimate dewfall amount on a roof surface. Agr. Forest Meteorol., 149, 1377–83, 2009.

[33] Richards, K., Adaptation of a leaf wetness model to estimate dewfall amount on a roof surface. Agr. Forest Meteorol., 149, 1377–1383, 2009.

[34] Parry, H. D., The semi-automatic computation of rawinsondes. Technical Memorandum WBTM EDL 10 US Department of Commerce, Environmental Science Services Administration vol. 9, II-4, 1969.

[35] Melissa, D. L., Philip, R., Christensen, Journal of Geophysical Research 102, 25,581-25,589, 1997.

[36] Zhao, D., Aili, A., Zhai, Y., Xu, S., Tan, G., Yin, X., Yang, R., Appl. Phys. Rev. 6, 021306, 2019.

[37] Shaw, R. H., Pereira, A. R., Aerodynamic roughness of a plant canopy: A numerical experiment. Agric. Meteorol. 26, 51-65, 1982.

[38] Ben-Asher, J., Alpert, P., BenZvi, A., Dew is a major factor affecting vegetation water use efficiency rather than a source of water in the eastern Mediterranean area. Water Resources Research 46, 10, 2010.

[39] Vazquez, A., Arias, J., Sanchez, R. M., Eur. J. Phys. 27, 667–673, 2006.

[40] Wood, L. A., The use of dew-point temperature in humidity calculations. Journal of Research of the National Bureau of Standards – C. Engineering and Instrumentation 74C, 117–122, 1970.

Subject Index

Technical concepts and key subjects are indexed at their verified discussion pages.

KEY SUBJECTS Condensation • Dark Energy • Einstein's Energy-Momentum Relationship • Hubble Constant • Local Thermodynamic Effects • Mars • Timeless Energy Principle • Ballistic Thermionic Effects

Author Guidelines

Comprehensive Guide to Publishing with GJSFR

Global Journal of Science Frontier Research | Open Access | Peer Reviewed | COPE Compliant

I. Our Commitment to Authors

The Global Journal of Science Frontier Research (GJSFR) is an internationally recognized, **open-access** academic journal publishing high-quality, peer-reviewed research across Physics & Space Science, Chemistry, Biological Science, Agriculture & Veterinary, Marine Science, Mathematics & Decision Science, Bio-Tech & Genetics, Environment & Geology, and interdisciplinary frontiers.

GJSFR is published by Global Journals Publishing Group Inc., indexed in major global databases, archived in leading digital repositories, and distributed worldwide in prestigious **hardbound volumes**.

II. One-Click Submission: Publish Without the Hassle

We accept manuscripts in **any common format** - Word, PDF, LaTeX, RTF, or plain text. You only need your name, email, and manuscript file. Submit at https://globaljournals.org/submit-an-article/. Our executives handle all formatting, including complex scientific notation and equations.

Heading style: In the final typeset article, author-created headings are normally set in sentence case for readability. Fixed journal headings such as Abstract, Introduction, Materials and methods, Results, Discussion, Conclusion, References, and Acknowledgements are standardized by the production team. Acronyms, proper nouns, gene/species names, chemical notation, brand names, and Roman numerals are preserved.

III. Rigorous Double-Blind Peer Review

Every manuscript undergoes **strict double-blind peer review** by domain experts. You receive a **comprehensive Review Report** and **Research Assessment Sheet** with line-numbered comments. Respond via the Author Dashboard or simply by email referencing line numbers. You never need to reformat anything - our production executives handle all changes.

IV. Publication Lifecycle

1. **Early View:** Galley proof with line numbers for final corrections via email or Dashboard.
2. **Ahead of Print:** Final corrected article launched before final issue compilation, without Volume or Issue numbers.
3. **eJournal:** Digital publication with DOI, indexed in global scientific databases.
4. **Hardbound Print:** Premium hardbound volumes distributed to science libraries, research institutions, and subscribers worldwide. Corresponding author receives a **complimentary hardbound copy** via government courier.

V. AI-Enabled Broadcasting & Multi-Format Publication

Articles are published as Interactive Digital eJournals, Premium Hardbound Print Editions, and Machine-Readable XML & HTML. AI-powered SEO ensures your frontier research reaches scientists, laboratories, and academic communities worldwide with maximum discoverability.

VI. Ethics, Integrity & COPE Compliance

GJSFR maintains the highest standards guided by the **Committee on Publication Ethics (COPE)**. All submissions are screened for plagiarism. Research involving human or animal subjects requires ethical approval. Enhanced COPE-based guidelines are available at https://globaljournals.org.

VII. Perpetual Archiving

Your research is **redundantly archived across geo-distributed data centers**, including **deep-sea facilities**, guaranteeing **lifetime hosting** and immutable DOI resolution.

VIII. Open Access: Free Knowledge for All

GJSFR is a Fully Open Access Journal.

IX. The LaTeX Author Package (Entirely Optional)

The LaTeX Author Package is entirely optional. Simply send your manuscript in any format.

Contact & Support

Portal: https://globaljournals.org/submit-an-article/
Website: https://globaljournals.org
Email: helpdesk@globaljournals.org

At GJSFR, your research pushes the frontiers of science.
We handle publishing so you can focus on discovery.

GLOBAL JOURNAL

of Science Frontier Research: A

Physics & Space Science

globaljournals.org

Save our Planet

Online ISSN 2249-4626

9 772249 462017